COMBINED THERMAL AND STRUCTURAL MODELING AND DESIGN OF A SHAPE

MEMORY ALLOY DRIVEN MORPHING SPACE RADIATOR

A Thesis

by

SEAN NEVIN

Submitted to the Graduate and Professional School of
Texas A&M University
in partial fulfillment of the requirements for the degree of

MASTER OF SCIENCE

Chair of Committee,	Darren Hartl
Committee Members,	Jim Boyd
	Debjyoti Banerjee
Head of Department,	Ivett Leyva

December 2021

Major Subject: Aerospace Engineering

ABSTRACT

Thermal control systems for future manned space missions are requiring increased turndowns to address heat rejection and thermal environment variations. As a solution, space radiators that alter the heat rejection of the system are implemented to maintain crew cabin temperatures at a feasible level. Current radiator systems can achieve a turndown ratio of 3:1, however, future missions demand over a 6:1 ratio. The morphing radiator concept falls into the category of variable heat rejection radiators, and accomplishes this through a change in shape of the high emissivity surface exposed to the environment. The actuating method uses a shape memory alloy, which is a unique material that uses a thermally-driven solid-solid phase transformation to generate strain and then fully recover. With these materials having a high energy density, they are often used as actuators and are applied here to passively thermally actuate the radiator. This thesis covers the development and implementation of a modeling tool to simulate the morphing radiator behaviour with further application as a design tool. To confirm the accuracy of the model, a validation study was conducted against previous thermal vacuum chamber testing. As a design tool, geometric trade studies were conducted to optimize the composite layup and a design of experiments was carried out to optimize shape memory alloy sizing and properties.

DEDICATION

To my family, friends and mentors throughout my life.

The quicker you let go of old cheese, the sooner you find new cheese.

ACKNOWLEDGEMENTS

CONTRIBUTORS AND FUNDING SOURCES

TABLE OF CONTENTS

LIST OF FIGURES

x

LIST OF TABLES

1. INTRODUCTION

1.1 Motivation

Manned space missions require a thermal control system (TCS) to maintain crew cabin temperatures at a reasonable level in a variety of adverse temperature conditions. At any given time the TCS is exposed to a variety of heat sources, both internal an external. Internally, astronauts and electrical equipment generate heat while externally planets and suns radiate heat [48]. With the absence of a medium to facilitate convection, IR radiation is the only means of of rejecting heat from the TCS. To accomplish this, these systems reject heat to the surrounding space environment through the use of a working fluid and radiator [24]. To assess the performance of these radiators, a metric called turndown is often used, measuring the ratio between maximum and minimum heat rejection. This metric is useful when evaluating a variety of radiators adaptation to given thermal environments and will be outlined in more detail in Section 2.1.

Common space radiators have turndowns of 3:1, but with future manned missions aiming to travel past Low Earth Orbit (LEO), a higher turndown ratio is required to deal with increased variations in environmental temperatures and heat loads [1]. Thus, the goal of this design is to improve that standard and aim for turndowns of 6:1 and higher. A basis for these goals can be seen in the Altair lunar lander which had a projected required turndown ratio of 6:1 [10]. Figure 1 provides an example of the required heat rejection along with the sink temperature for the duration of the Altair mission. Three distinct phases arise providing variable thermal environments. First, during LEO the spacecraft is orbiting the earth following its launch. Next, Trans-Planetary Coast (TPC) represents the post trajectory burn travel period from orbit to the moon. And last the Planetary Surface Operations (PSO) signifies the time spent landed on the moon. For this mission, the sink temperature varies from 70 K to 228 K, necessitating variable heat rejection rates. Additionally, the TCS often requires increased heat rejection in warmer environments and less heat rejection in colder environments requiring high turndown

ratios.
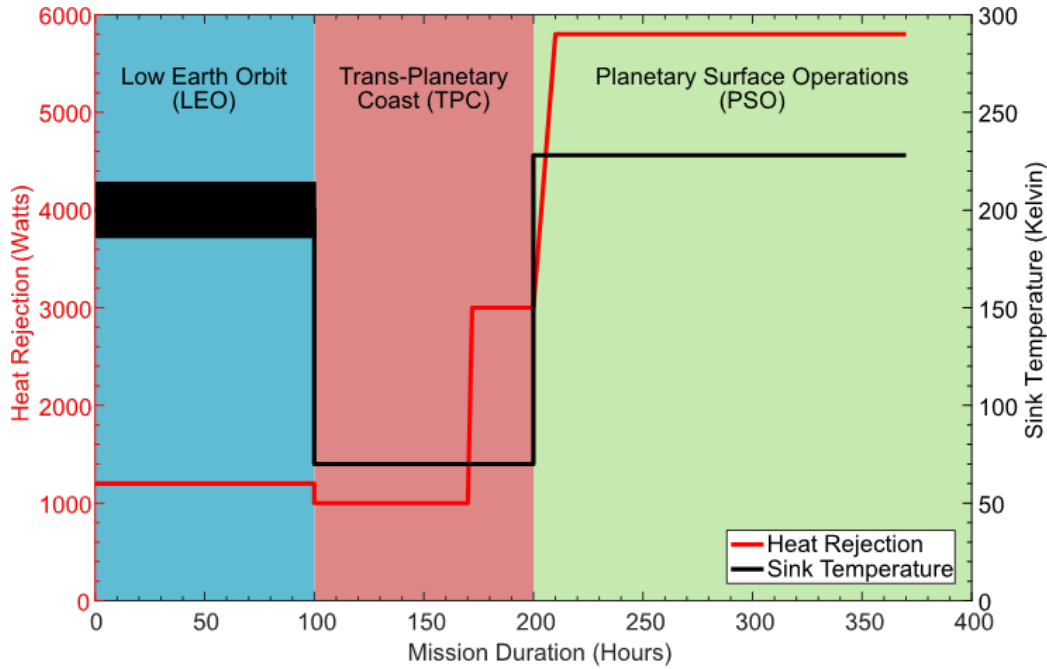
Figure 1: Altair mission profile heat load requirements [20][6]

One such application for achieving higher turndowns is a variable heat rejection radiator [11]. A NASA roadmap indicates this technology as a viable option for achieving their goal turndown of 6:1 with an upper goal of 12:1 [29]. There are also plans for demonstration of this technology on the International Space Station to advance the variable heat rejection radiator concept to TRL 7. Many versions of this have been investigated, such as the following: electrochromic radiator, digital radiator, deployable radiator, freezable radiator, stagnation radiator, origami radiator, variety in coefficients of thermal expansion, thermochromic materials, and morphing radiator. Electrochromic radiators achieve a turndown through variation in emissivity when applying a voltage [12]. Similarly, thermochromic coatings such as vanadium dioxide (VO_2) were used which change their emissivity with temperature [19]. Digital radiators have control of specific sections of a radiator with the capability to switch those regions on or off [13]. Freezing radiators focus on reducing the minimum heat rejection to near zero through a freezing of the working fluid [15]. Additionally, other work has been done to develop a stagnation radiator which avoids

freezing while still reducing the heat rejection rate through the use of viscosity changes due to temperature [16]. Origami radiators use surfaces with different emissivity to quickly change emissive properties of the structure [17]. Radiators with variations in coefficients of thermal expansion are used to thermally actuate a structure and expose higher emissivity surfaces as it reaches higher temperatures [18]. A deployable radiator has been designed which deploys and retracts a set of panels using shape memory alloys (SMAs) as the actuating mechanism [14]. Similarly a deployable two-phase radiator was implemented which utilizes a hollow curved panel with a working fluid sealed inside. Increasing the fluid temperature causes an increase in the vapor pressure which in turn results in the radiator opening and vise versa for the case of a decrease in temperature [47].

The present research focuses on a morphing radiator, which is capable of modifying its geometry to vary the amount of heat rejection [2][3][20]. The current morphing radiator design is a cylindrical composite that unfolds to a semicircular shape using SMAs to passively thermally actuate the structure. To visualize this passive thermal actuation of the radiator, Figure 2 below shows a temperature contour plot of the closed and open states of the radiator.
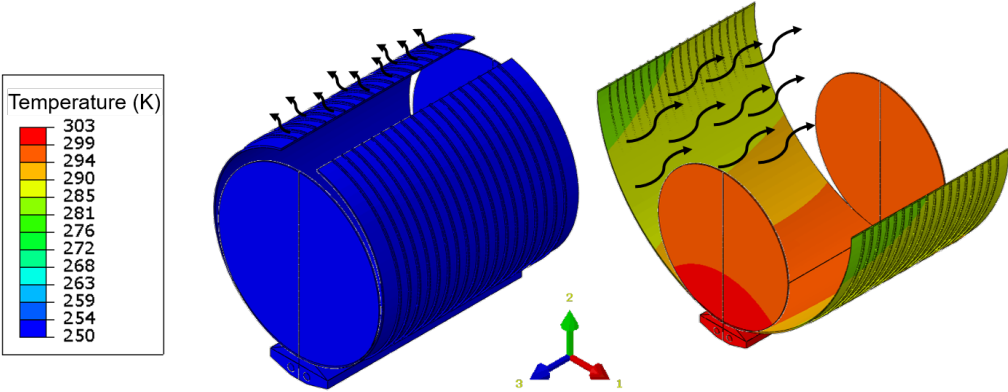
Figure 2: Temperature contour plots of open and closed states of the radiator.

As seen, for the cold case on the left, the radiator remains closed rejecting only a small amount of heat due to a low emissivity definition on the outer surface of the radiator which

3

is representative of an insulation. As the radiator reaches an elevated temperature, the SMA wires transform, shrinking them and opening the radiator to increase its view factor of the high emissivity coated inner surface that will reject a larger amount of heat to the environment.

SMAs are a unique metal that can be deformed and recover their original shape through a temperature change. This is referred to as the shape memory effect (SME) and is accomplished through the existence of two distinct solid phases, martensite and austenite. Austenite inherits a cubic crystal structure while martensite is monoclinic. The transition between these phases results in a strain generation. SMAs take on the austenitic phase in high temperature conditions, while the martensitic phase exists at a cooler temperature state. The phase diagram in Figure 3 below demonstrates a general thermal cycle of an SMA. Four thresholds exist to define at what temperatures transformation starts and finishes in either martensite or austenite. When cooling from austenite to martensite the transformation initiates at the martensitic start temperature, M_s, and transforms fully into martensite upon passing the martensitic finish temperature, M_f. Upon heating back into austenite, the transformation initiates at the austenitic start temperature, A_s, and transforms fully into austenite upon reaching the austenitic finish temperature, A_f. By utilizing this SME, SMAs can serve as actuators with a high energy density [4]. SMA actuators have a wide number of applications including, variable geometry chevrons, deployable solar arrays, and aircraft control surfaces [21][22][23]. In the present research, SMA wires are used to passively actuate the radiator based on the operational temperature ranges.
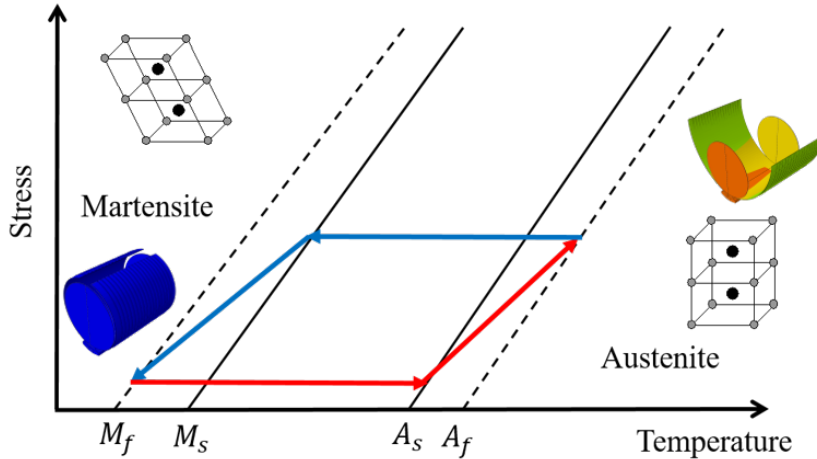
Figure 3: SMA phase diagram

1.2 Shape Memory Alloy Applications in Composites

The integration of SMAs into composite systems has a deep history. Incorporating SMAs into composite structures has led to developments in actuation, damping, vibration control, sensing and self healing. A wide variety of research exists in the field of SMA composite systems including polymer matrix and polymer composite matrix composites, metallic matrix composites, ceramic matrix composites, and SMA matrix composites. To narrow the scope to the applications relating to the present research, I will focus on the polymer-based composites which refer to either a polymer matrix reinforced with SMA or a polymer matrix composite reinforced by SMA, with a few noteworthy applications in other fields [28].

Starting with composites composed of a polymer matrix reinforced with SMA, structural healing applications of SMA include microencapsulated healing agents and catalysts to repair an epoxy matrix with the aid of embedded SMA wires SME to apply compressive force to aid in the curing process [32]. Two main contributing factors from the SMA are the reduced crack volume from compression, along with additional heating applied by the SMA to the healing agent to improve polymerization and overall mechanical properties once cured. Reinforcing of polymer matrix with SMA fibers and particles has shown significant improvements to damping

properties of the resulting composite. Both continual [33,34] and short fibers [35,36] were tested and proven to increase the storage modulus, with short fibers performing the best at a six times increase compared to the matrix alone with only small weight percentage contributions of the SMA [36]. For actuation control, SMA wires were inserted into a polymer matrix to create wrinkles which can be utilized for active texture control through joule heating of the SMA [37].

Moving to polymer matrix composites further reinforced by SMA, a few interesting applications arise. First in regards to actuation, a three-way bending actuation cycle was achieved through a shape memory composite belt [38]. The belt is composed of two SMA tapes with different phase transformation temperature ranges placed inside various layers of a shape memory polymer (SMP) material and heat treated. The actuation process is enabled by heating or cooling to the differing transformation temperatures of the SMA tapes, and using the softening of the SMP as it approaches and exceeds its glass transition temperature. Creating composites with improved impact damage tolerance through reinforcement of SMAs has been extensively investigated. Hybrid composites are one approach to utilize the superelastic deformation of SMAs to absorb energy from the impact [39]. Some common forms of SMA hybrid composites are embedded wires or strips inside of the matrix material as well as embedded SMA films and particulates. Pappadà et al. tested various specimens with hybrid SMA strips inside both glass reinforced and carbon fiber reinforced laminates [40][41]. They discovered a slight improvement in the impact energy required to break the specimen for both laminate types, while with repeated lower energy impacts they observed a small improvement in glass reinforced laminates and a worsening in carbon fiber reinforced laminates [40]. Other work regarding composites with embedded SMA wires has shown higher levels of absorbed impact energy before failure along with an increase in the composites overall toughness [42]. Furthermore, SMAs constitutive properties are highly temperature driven, and thus Kang and Kim conducted a series of impact tests on glass reinforced epoxy laminates versus laminates with embedded SMA wire under varying temperatures [43]. A key result showed the SMA laminates peak impact force to

6

be lower than the base laminate at higher temperatures, but this reversed at lower temperatures. This potentially demonstrates the degree of reinforcement the SMA provides is linked to the temperature through the corresponding mechanical properties at different phases of the SMA. Next, high velocity impact tests were conducted against a glass reinforced epoxy composite with a surface bonded SMA-epoxy hybrid layer as the impacting surface [44]. The SMA hybrid layer improved the composites perforation resistance by double, outperforming other hybrid layers such as aluminum-epoxy and kevlar-epoxy. Another unique application of SMAs in composites is a smart composite patch composed of either kevlar-epoxy or glass-epoxy and SMA wires [45]. In this case, upon patching either side of a notched plate specimen, the SMA reinforced patches performed the best under subsequent tension, bending and impact loading. Ciampa et al. demonstrated weaving of SMA filament material into a carbon-epoxy composite allows for an improvement in damage tolerance [30]. In particular the SMA aids in preventing the start of delamination by improving the interlaminar fracture toughness as well as serving to partially close cracks that have already propagated through electrical heating to initiate SME. Lastly, a noteworthy concept involves the use of magnetic shape memory alloys (MSMA) as a tool for damage sensing within a composite composed of SMA particles inside of an aluminum matrix [31]. Given enough damage from crack propagation, high local stresses near embedded SMA particles will induce martensitic stress transformation, giving off a change in magnetic permeability due to phase change from paramagnetic austenite to ferromagnetic martensite. This nondestructive evaluation method is used as a tool to sense damage within the composite.

1.3 Journey of the Morphing Radiator Concept

Previous experimental work was done with this design of the radiator which motivates the development of the finite element analysis (FEA) model used for this research. As an initial proof-of-concept, a prototype radiator was created that is comprised of a stainless steel foil with a graphite sheet layer adhered for improved thermal conductivity [20][2]. The sheet was then rolled to form a semicircular shape referred to as a winglet. To actuate the winglet, two SMA

wires crossing at the middle were attached by several terminating holes at the end of the panel. For sizing reference, the dimensions of this assembly when layed flat was 5 in long by 2 in wide, and when rolled the resulting open circle winglet diameter measured 1.6 in. To assemble the full system, two of these radiators were lined up in series and attached to an aluminum rod containing resistive heating tape on one end. To demonstrate the technology, the system was thermally cycled from 50°C to 140°C and then cooled by switching off the heater resulting in the morphing of the winglets. Figure 4 shows the experimental setup of the radiator system.
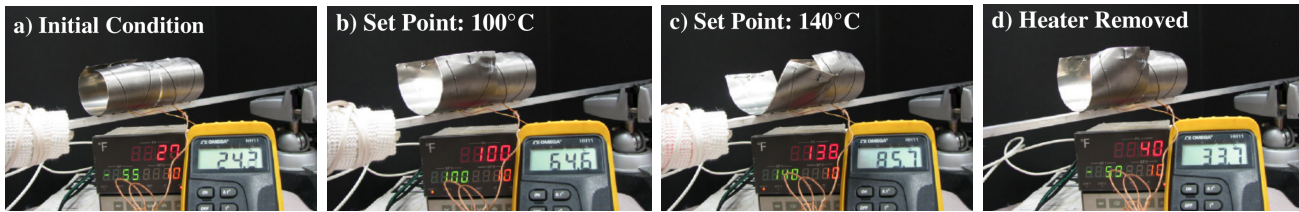
Figure 4: First morphing radiator prototype [20]

The second prototype explored the use of a five-ply composite laminate to take advantage of the high thermal conductivity and structural flexibility [20]. The layup consisted of a unidirectional prepreg tape system, CSW T40-800/5320-1. Similar to the first, it used SMA wires to actuate the panel through thermal cycling. The panel was first cooled to -20°C, exhibiting a cylindrical shape, and then allowed to settle to room temperature, where it achieved a nearly flat shape. This morphing behaviour can be seen below in Figure 5. These prototypes marked the first demonstration of a passive or "self-morphing" radiator system [20].
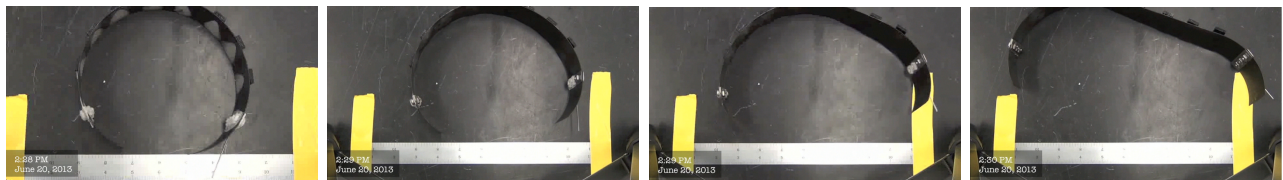
Figure 5: Composite morphing radiator prototype [20]

Next, another prototype was fabricated for eventual testing in a thermal vacuum chamber to simulate a relevant thermal environment [3]. This iteration consisted of a copper panel also

rolled to a semicircular shape with ten SMA wires wrapped around the exterior surface and now attached to the end of the panel through set screws passing through aluminum terminal blocks. Preliminary tests showed difficulty in fully closing the panel to a cylindrical shape, thus leading to the implementation of a steel spring to apply a biasing force during closing. A high emissivity polyurethane coating, Aeroglaze Z307, was applied to the inside surface of the panel. For heating, the copper panel was epoxied to a stainless steel flow tube passing over the base interior side of the panel. Figure 6 illustrates this prototype in the open configuration.
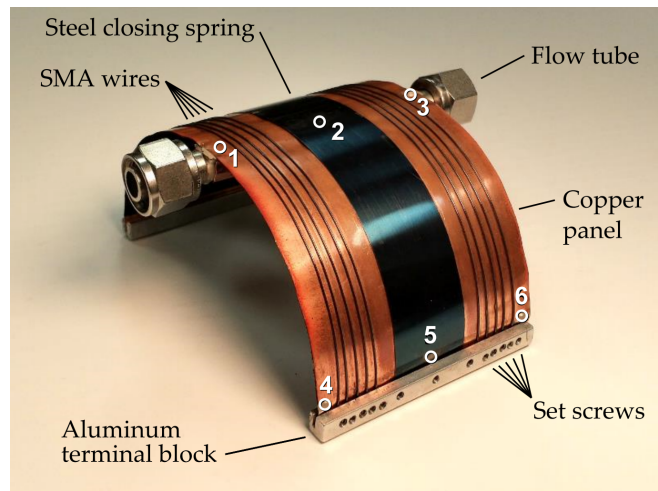
Figure 6: Copper morphing radiator prototype [3]

Thermal chamber testing held a constant shroud temperature of -178°C while the working fluid, Dynalene HC-50, was cooled to -45°C and heated to 60°C. As Figure 8 shows, the testing demonstrated successful morphing of the radiator from its initial semicircular configuration to a nearly full closed cylinder. Upon heating however, the initial semicircular shape was not recovered from SMA transformation temperatures misalignment with the operational environment.
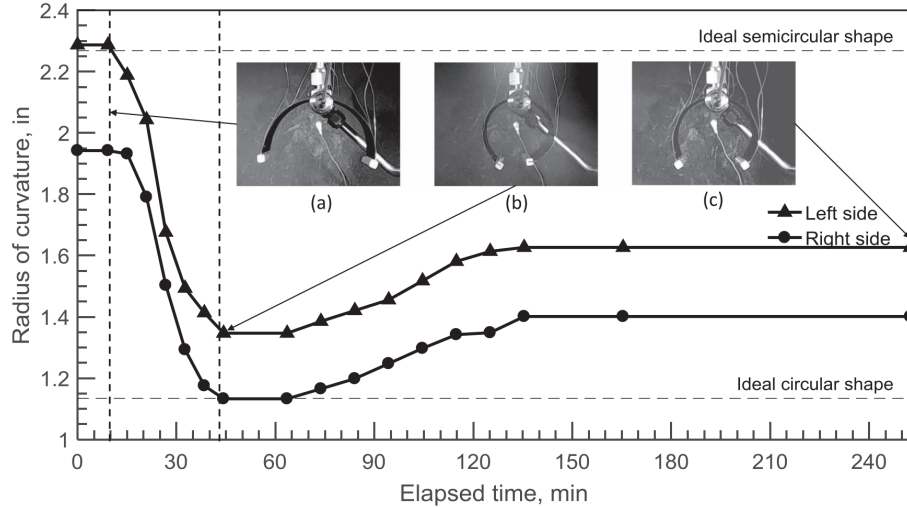
Figure 7: Copper morphing radiator open angle results [3]

This also introduced the challenges of this technology with respect to the required transformation of the SMA. In particular, the stress in the wires decreases towards zero as the panel closes, decreasing the martensite finish temperature in the process making it more difficult to completely transform into martensite and fully close the panel. Consequently this can be applied to the heating cycle in which the stress increases as the panel opens, shifting the austenite finish temperature and leading to possible challenges with full recovery of the open state.

Taking design considerations from the previous copper panel morphing radiator, a composite laminate panel was designed and tested in a thermal vacuum chamber [5]. The laminate consisted of K13D2U pitch-based carbon fibers with RS-3C resin. Furthermore, this testing investigated the use of both SMA wires and strips, as well as proposing the idea of end shields for the first time. The primary purpose of the end shields is to further reduce heat rejection in the cold closed configuration, improving overall turndown. Figure 8 shows the composite radiator prototype.
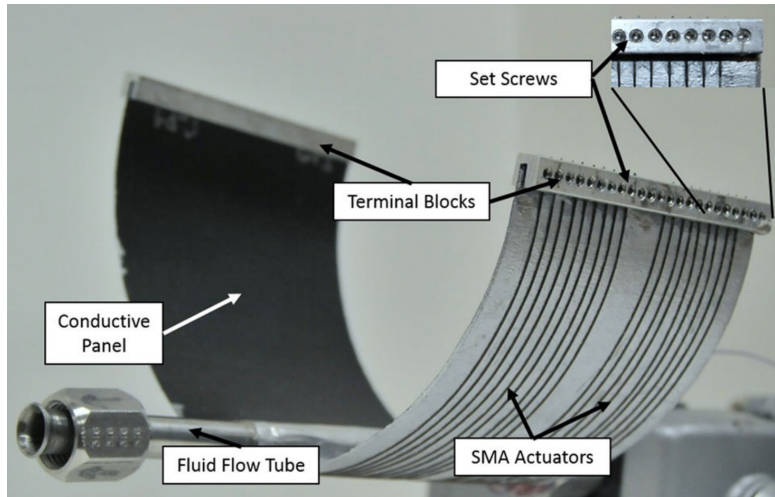
Figure 8: Revised composite morphing radiator prototype [5]

The most recent thermal vacuum chamber testing of a morphing radiator design implements many of the previous design considerations [6]. Figure 9 below depicts a single panel test conducted inside a thermal vacuum chamber. SMA strips were used as the actuating mechanism and are fixed with the same terminal block set screw method from previous designs. To improve turndown performance, the entire panel is wrapped in multi-layer insulation (MLI) and end shields are attached at either end of the panel. Also, a stainless steel flow tube is mounted underneath the base of the panel through an aluminum mating component to avoid blocking any of the composite panel's view of space. The fluid temperature is cycled to demonstrate full operational opening and closing of the radiator. Although this design performed the best in terms of the degree of openness at its hot and cold configurations, a large margin still remains in closure. Through every iteration of this morphing radiator concept it has become apparent that careful tuning of SMA properties is critical to achieving full closure and opening of the radiator.

Figure 9: Experimental single panel test [6]

1.4 Thesis Summary

The goal of this work is to assist in advancing the technology readiness level of the morphing radiator from a 3-4 to a 4-5. To accomplish this the present work outlines a FEA model used as a design tool for investigating different radiator panel geometries, and SMA sizing and properties. By simulating the behaviour of the morphing radiator system, informed design decisions were made about subsequent benchtop and thermal vacuum chamber testing.

1. Develop a morphing radiator finite element model to simulate the behaviour of the thermal control system, incorporating SMA constitutive modeling and ray tracing cavity radiation definitions.

2. Validate the morphing radiator model against previous thermal vacuum chamber testing.

3. Carry out a geometric trade study to determine the optimal panel geometry and composite layup which maximizes turndown.

4. Conduct a design of experiments to inform SMA sizing and properties, with a major focus on minimizing closed angle.

12

2. ENGINEERING FOUNDATIONS

Presented here are the fundamental assumptions and theory of various topics incorporated into the creation of the morphing radiator model. Topics include turndown background, composite mechanics, SMA constitutive modeling, and cavity radiation definitions.

2.1 Geometric and Thermal Definitions

For clarification, the degree of openness or open angle of the radiator is a term that will be frequently used as a metric to measure how much the view factor of the high emissivity inner surface of the radiator has increased. To clearly demonstrate what is meant by this, a graphic can be seen below in Figure 10 as to how this angle is defined exactly.
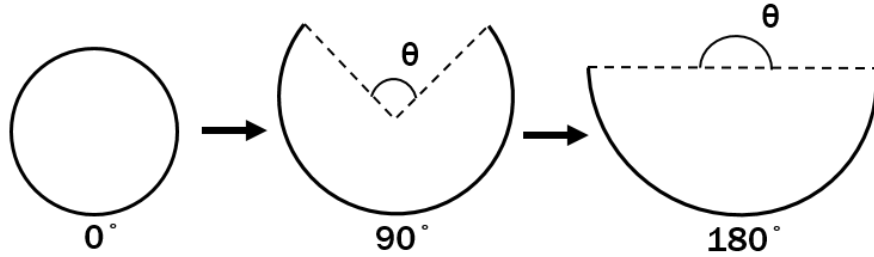
Figure 10: Degree of openness or open angle definition

At an angle of 0°, the radiator is considered to be fully closed, and at 180° the radiator is considered to be fully open. It will be shown in a later study that further open angles past 180° will give diminishing returns in turndown, which leads to the reasoning to design for 180°. Next, the turndown is defined as the ratio between the maximum and minimum heat rejection. The heat rejection, Q, is calculated from the emissivity, ε, area, A, view factor, F, temperature of the surface, T, and temperature of the environment, T_∞. This results in the following formulas:

$$Q = \epsilon \sigma AF(T^4 - T_{env}^4) \tag{2.1}$$

$$Turndown = \frac{Q_{max}}{Q_{min}} = \frac{\epsilon_{max}\sigma(AF)_{max}(T_{radiator,max}^4 - T_{space}^4)}{\epsilon_{min}\sigma(AF)_{min}(T_{radiator,min}^4 - T_{space}^4)} \tag{2.2}$$

It follows that the turndown for any given open angle of the radiator is the current heat rejection divided by the minimum heat rejection that occurs at the closed case of the radiator.

Various types of turndown can arise in a thermal control system, which is guided by (2.2). First any changes in emissivity is called a surface turndown sometimes also referred to as electrochromic effects. Geometric turndown refers to the change in view factor that indiciates a given surfaces view of space and is one of the primary turndowns for this morphing radiator technology. Another major contributing turndown method is system turndown which commonly refers to temperature changes in the thermal control system from system heat loads like crew cabin temperatures, electrical heat contributions, or heat exchangers. Lastly, environmental turndown accounts for variations in mission environments or vehicle orientation in correlation to the sun. To maximize turndown for the morphing radiator, a special high emissivity coating is painted on the inner surface of the radiator and MLI is wrapped around the exterior surface to minimize heat rejection in the closed case. Additionally the morphing radiator utilizes system and geometric turndown through the temperature cycling of the working fluid and associated morphing shape of the composite panel.

Typical thermal control systems for space missions require the heat rejection to be either turned down or turned up based on environmental conditions. Typically the turning up is the more difficult of the two to perform in a reasonable time frame.

2.2 Composite Mechanics

Classical Lamination Theory (CLT) assumes a plane stress state which is valid for thin plates and loading which resides in the same plane as the plate. For the morphing radiator, both of these hold true, as the bending mode exhibits tension and compression in the tangential plane of the panel. The assumptions of plane stress in the x-y plane can be written as:

$$\sigma_{zz} = \tau_{yz} = \tau_{zx} = 0 \tag{2.3}$$

where the axial and shear stresses are represented by σ and τ. CLT is vital for this work with the morphing radiator as it was used in a composite design study when transforming global stresses into their local coordinate systems for a maximum failure stress criterion as well as understanding the macromechanics of the cured composited. The coordinate system of the composite panel can be visualized in Figure 11, where the axis labels 1, 2 and 3 represent the x, y and z axes, respectively.
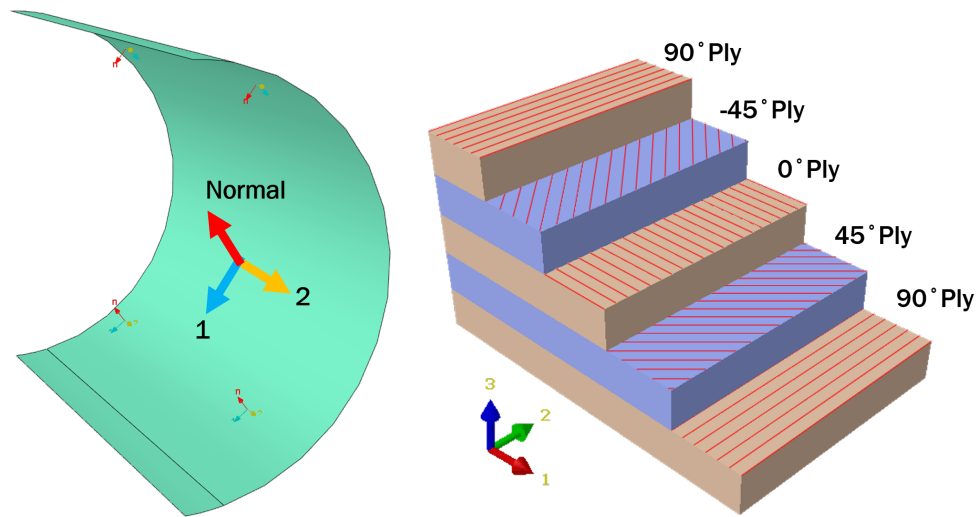
Figure 11: Radiator composite local coordinate system with example laminate

When discussing CLT, it is important to note the material symmetries existing in a composite. First, isotropy is defined as a material having the same properties in different directions such as metals or plastics. However, a composite is composed of stiff fibers aligning in one direction along with a softer matrix material, leading to anisotropy or varying of properties with direction. More specifically, from a plane stress assumption, the composite exhibits transverse isotropy, which refers to partial material symmetry. In this case, the y and z properties can be approximated to be equal while the x and y properties are drastically different. Due to this asymmetry, the angle of the ply will affect the material properties in the global coordinate system.

Under a plane stress assumption, the stress-strain relation for an orthotropic lamina in the principal material coordinate system is:

$$
\begin{bmatrix} \sigma_1 \\ \sigma_2 \\ \tau_{12} \end{bmatrix} = \begin{bmatrix} Q_{11} & Q_{12} & 0 \\ Q_{12} & Q_{22} & 0 \\ 0 & 0 & Q_{66} \end{bmatrix} \begin{bmatrix} \varepsilon_1 \\ \varepsilon_2 \\ \gamma_{12} \end{bmatrix}
\tag{2.4}
$$

Given an arbitrary angle in the plane of the lamina, the stress can be defined as:

$$
\begin{bmatrix} \sigma_x \\ \sigma_y \\ \tau_{xy} \end{bmatrix} = \begin{bmatrix} Q_{11} & Q_{12} & Q_{16} \\ Q_{12} & Q_{22} & Q_{26} \\ Q_{16} & Q_{26} & Q_{66} \end{bmatrix} \begin{bmatrix} \varepsilon_x \\ \varepsilon_y \\ \gamma_{xy} \end{bmatrix}
\tag{2.5}
$$

Using this nomenclature, the stress in the kth ply can be simply written as:

$$
\{\sigma\}_k = [Q_k]\{\varepsilon\}_k
\tag{2.6}
$$

Furthermore, the strains throughout the laminate can be represented by the midplane strains and curvatures,

$$
\{\varepsilon\}_k = \{\varepsilon\}_0 + z\{\kappa\}
\tag{2.7}
$$

where $\{\varepsilon\}_0$ denotes the midplane strain in the laminate, κ defines the midplane curvature of the laminate, and z is the distance from the midplane to the center of a given lamina illustrated later in Figure 12.

As an example let us look into the macromechanics of a composite laminate. Upon formation of a composite laminate, to better understand its constitutive response, the forces and moments, N and M, can be related to the midplane strains and curvatures, ε and κ, through the ABD matrix. This matrix includes three submatrices prescribing the extensional (A), extensional-

16

bending coupling (B), and bending (D) stiffnesses of the laminate.

$$
\begin{bmatrix} N \\ M \end{bmatrix} = \begin{bmatrix} A & B \\ B & D \end{bmatrix} \begin{bmatrix} \varepsilon \\ \kappa \end{bmatrix}
\tag{2.8}
$$

The force and moment resultants are calculated by summing the stresses in each ply layer of the laminate,

$$
N = \sum_{k=1}^{n} Q_k \varepsilon_k (z_k - z_{k-1}), \, M = \frac{1}{2} \sum_{k=1}^{n} Q_k \varepsilon_k (z_k^2 - z_{k-1}^2)
\tag{2.9}
$$

Next, each of the laminate stiffness matrices can be calculated through the following equations:

$$
A = \sum_{k=1}^{n} Q_k (z_k - z_{k-1}), \, B = \frac{1}{2} \sum_{k=1}^{n} Q_k (z_k^2 - z_{k-1}^2), \, D = \frac{1}{3} \sum_{k=1}^{n} Q_k (z_k^3 - z_{k-1}^3)
\tag{2.10}
$$

where Q is the global stiffness matrix of which Q_k represents the local stiffness matrix of the kth ply rotated back to the global coordinate system based on the ply angle. Furthermore, z_k represents the vertical position in the ply measured from the midplane of the laminate. This distance from the midplane along with the ply angle rotation can be further visualized in Figures 12 and 13.
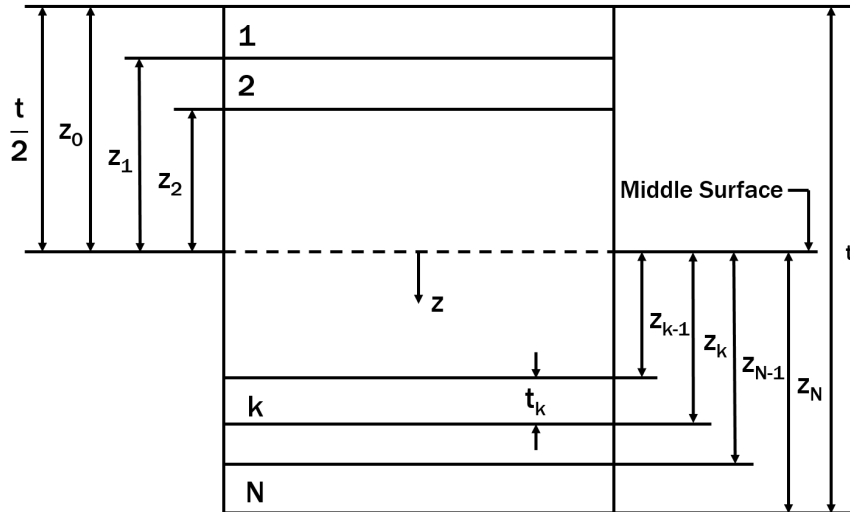
Figure 12: Laminate geometry given N plies (adjusted from [27])
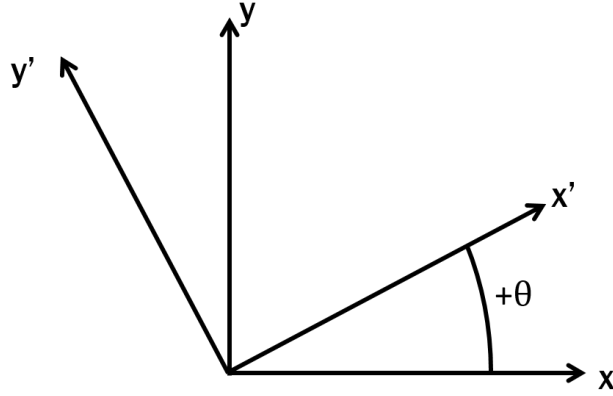
Figure 13: Local ply orientation angle in global frame of reference

The transformation of Q is performed through the following rotation matrix and transformation equation, assuming rotation about the z-axis for a x-y plane stress assumption:

$$Q_k = T^{-1}QT^{-T} \tag{2.11}$$

$$T_z = \begin{bmatrix} \cos^2(\theta) & \sin^2(\theta) & 2\sin(\theta)\cos(\theta) \\ \sin^2(\theta) & \cos^2(\theta) & -2\sin(\theta)\cos(\theta) \\ -\sin(\theta)\cos(\theta) & \sin(\theta)\cos(\theta) & \sin^2(\theta) - \cos^2(\theta) \end{bmatrix} \tag{2.12}$$

In reference to the composite morphing radiator, understanding the D matrix is key as the primary loading is bending. Common practice for ply stacking sequence of a carbon fiber composite laminate is to maintain symmetry and balance with respect to the plies angled between $0°$ and $90°$. Symmetry in a laminate refers to the symmetry of ply orientations about the midplane of the composite. Balanced laminates always have positive and negative angle ply pairs of equal-thickness which can either be adjacent or not. However, if a layup is symmetric or unbalanced, this can lead to bend-twist coupling terms appearing in the D matrix (D_{16}, D_{26}). To eliminate these terms an anti-symmetric layup can be used, which follows symmetry of the ply orientations about the midplane of the laminate with opposite signs. Although, anti-symmetry causes extension-twist and bend-shear coupling to arise in the B matrix (B_{16}, B_{26}). With the morphing

18

radiator loading existing primarily in bending, an anti-symmetric layup was found to perform best with the least twist effects. An example of bend-twist coupling can be seen in Figure 14 when going from an anti-symmetric balanced [90/45/0/-45/90] layup to a symmetric unbalanced [90/45/0/45/90] layup. Additionally, the D_{22} term is clearly dominant demonstrating the bending stiffness in the desired bending case about the global laminate 2 axis depicted previously, which aligns with the 0° ply. Furthermore, in practice this twist phenomena was found during a composite trade study to determine the optimal layup. Figure 15 shows an end-on-view of both the layups mentioned previously to illustrate the severity of this twist for each case. In turn, the twist caused a stress concentration at the fixed mounting region of the radiator leading to earlier failure.

$$D = \begin{bmatrix} 7.16 & 5.74 & 0 \\ 5.74 & 88.4 & 0 \\ 0 & 0 & 5.73 \end{bmatrix}, \begin{bmatrix} 7.16 & 5.74 & 5.44 \\ 5.74 & 88.4 & 5.44 \\ 5.44 & 5.44 & 5.73 \end{bmatrix}$$

Figure 14: Bending stiffness D matrix comparison of anti-symmetric balanced (left) versus symmetric unbalanced (right) laminates
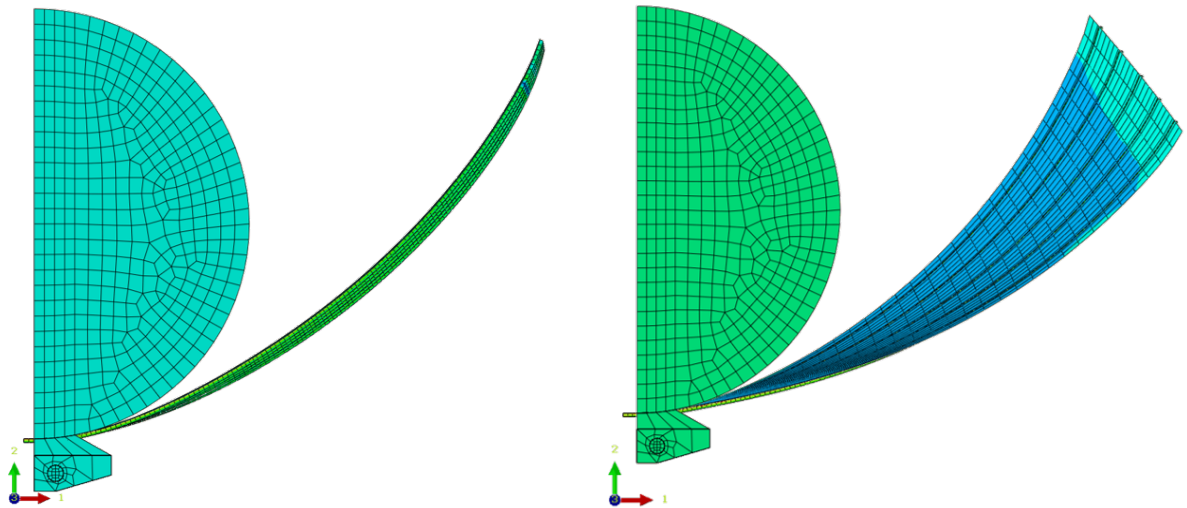
Figure 15: Displacement contours exhibiting bend-twist phenomena, anti-symmetric balanced layup on left, symmetric unbalanced layup on right

2.3 Composite Selection

Carbon fiber reinforced composites are chosen for the radiator application for their ability to reach high combined conductivity and stiffness properties. The chosen materials for this are a K13C2U carbon fiber and an RS-3C resin manufactured by Toray Composite Materials America with properties listed in Tables 1 and 2, respectively [8][9]. The fiber was chosen for its high thermal conductivity properties combined with its high stiffness. The resin was chosen for having a good balance between toughness and performance at high temperatures. This project has a background with experimental work and these materials follow from that as well [5]. Due to availability a slightly different material is used here as the former fiber was K13D2U which has a slightly higher stiffness with a lower thermal conductivity. The main challenge when switching to the K13C2U fiber is that the provided materials ply thickness doubled. However, a computational trade study is conducted for a variety of composite laminates to determine the optimal layup that maximizes turndown for this increased ply thickness. The composite properties for use in finite element methods were experimentally verified using 4-point bend tests of composite specimen strips.

Table 1: K13C2U carbon fiber properties [8]

Property	Value
$0^{\underline{o}}$ Tensile Modulus	81 Msi
$0^{\underline{o}}$ Tensile Strength	296 ksi
$90^{\underline{o}}$ Tensile Modulus	0.676 ksi
$90^{\underline{o}}$ Tensile Strength	2.79 ksi
$0^{\underline{o}}$ Compressive Modulus	75.65 Msi
$0^{\underline{o}}$ Compressive Strength	49.75 ksi
$90^{\underline{o}}$ Compressive Modulus	0.746 ksi
$90^{\underline{o}}$ Compressive Strength	11.35 ksi
Fiber Modulus (Fiber Direction)	132 Msi
Fiber Strength (Fiber Direction)	560 ksi
Fiber Thermal Conductivity (Fiber Direction)	387 W/m-K
In-Plane Poisson's Ratio (ν_{12})	0.33
In-Plane Shear Modulus (G_{12})	0.2175 Msi

Table 2: RS-3C resin properties [9]

Property	Value
Tensile Modulus	11.6 ksi
Tensile Strength	0.43 Msi
Tensile Strain	4.9%
Flexural Stength	18.4 ksi
Flexural Modulus	0.48 Msi
Fracture Toughness	2.1 in-lb/in^2

2.4 Formulation of SMA Constitutive Model

The constitutive model used to characterize SMA behaviour is partly summarized here and starts with the framework developed by Boyd and Lagoudas [53][54]. This involves a thermodynamic free energy potential, of which the Gibbs free energy potential, G, is defined here.

This energy potential incorporates a variety of independent state variables ($G = G(\boldsymbol{\sigma}, T, \boldsymbol{\zeta}^t)$), namely two external variables, the applied stress tensor and absolute temperature T, and a set of internal variables packaged inside $\boldsymbol{\zeta}^t$. These internal state variables can be unpacked as $\boldsymbol{\zeta}^t = \{\boldsymbol{\varepsilon}^t, \xi, g^t\}$. First, $\boldsymbol{\varepsilon}^t$ is the transformation strain tensor which represents the inelastic strain generated and recovered from forward and reverse transformation beteween austenite and martensite, respectively. The term ξ ($0 \leq \xi \leq 1$) is the total martensitic volume fraction, specifying the state of transformation within the material which is driven by the amount of martensitic crystal variants present. Next the transformation hardening energy g^t captures the change in mixing energy between austenite and martensite during transformation at a given constant stress [55]. Expansion of the Gibbs free energy can be found in the framework of Boyd and Lagoudas [53][54].

Diving deeper into the internal state variables, the evolution equations for the transformation strain and hardening energy are necessary to understand. The associated flow rule for transformation strain is follows as,

$$\dot{\boldsymbol{\varepsilon}}^t = \boldsymbol{\Lambda}^t \dot{\xi}, \qquad \boldsymbol{\Lambda}^t = \begin{cases} \boldsymbol{\Lambda}^t_{fwd}, & \dot{\xi} > 0, \\ \boldsymbol{\Lambda}^t_{rev}, & \dot{\xi} < 0. \end{cases} \tag{2.13}$$

Note that there are two cases for the transformation direction tensor $\boldsymbol{\Lambda}^t$. These correspond to forward transformation leading to generation of inelastic transformation strain, and reverse transformation which corresponds to the recovery of that inelastic strain. These forms are defined as,

$$\boldsymbol{\Lambda}^t_{fwd} = \frac{3}{2} H^{cur} \frac{\boldsymbol{\sigma}'}{\overline{\sigma}}, \qquad\qquad \boldsymbol{\Lambda}^t_{rev} = \frac{\boldsymbol{\varepsilon}^{t-r}}{\xi^r}, \tag{2.14}$$

where H^{cur} is the maximum transformation strain for full transformation into martensite. Next,

$\overline{\sigma}$ refers to the Mises stress following the correlation,

$$\overline{\sigma} = \sqrt{\tfrac{3}{2}\boldsymbol{\sigma}' : \boldsymbol{\sigma}'} \tag{2.15}$$

where $\boldsymbol{\sigma}'$ is the deviatoric stress tensor. Given the form of the forward transformation direction tensor and that the Mises definition is scalar-valued, the direction of the applied stress is what drives the orientation of the transformation strain. On the other hand, to capture the transformation history of the given SMA material, the orientation and magnitude of strain recovery during reverse transformation is assumed to follow the average orientation of martensite upon transformation reversal. Through this method a memory term arises, ξ^r, which provides the last martensitic volume fraction achieved during forward transformation. Additionally, ε^{t-r} describes the amount of transformation strain generated at the end of forward transformation. Both of these terms are obtained at the moment of transformation reversal.

The parameter of maximum transformation strain, H_{cur}, used in this model refers to the saturated value or maximum possible transformation strain at higher levels of applied stress. Additionally, the Two Way Shape Memory Effect (TWSME) tends to develop in trained SMA materials, exhibiting small amounts of strain at low stress levels. To account for this effect, a parameter called H_{min} is implemented. Then to obtain the correct amount of transformation strain for varied levels of applied stress, the maximum transformation strain H_{cur} is experimentally fit with a decaying exponential function using data collected from uniaxial isobaric thermal cycling tests.

$$H^{cur}(\overline{\sigma}) = \begin{cases} H_{min} & ; \quad \overline{\sigma} \leq \overline{\sigma}_{crit}, \\ H_{min} + (H_{sat} - H_{min})(1 - e^{-k(\overline{\sigma} - \overline{\sigma}_{crit})}) & ; \quad \overline{\sigma} > \overline{\sigma}_{crit}. \end{cases} \tag{2.16}$$

where σ_{crit} establishes the critical Mises equivalent stress where transformation strain beyond H_{min} begins and k is an experimentally obtained constant from aforementioned isobaric testing.

The term H_{sat} also refers to the maximum recoverable transformation strain achieved at which higher applied stresses do not result in further strain generation.

Moving on to the evolution equation for hardening energy during transformation,

$$\dot{g}^t = f^t \dot{\xi}, \qquad f^t = \begin{cases} f^t_{fwd}, & \dot{\xi} > 0, \\ f^t_{rev}, & \dot{\xi} < 0. \end{cases} \qquad (2.17)$$

where the term f^t symbolizes the hardening function that provides the transformation hardening behaviour. Given a full transformation cycle, both the internal and external variables fully recover their initial values. In an energy sense, this means there must be an energy recovery in all of the decomponsed Gibbs free energy terms. The only term from that formulation that varies with a full transformation cycle is the transformation hardening energy g^t, which necessitates the following relationship between the hardening energy functions during forward and reverse transformation:

$$\int_0^1 f^t_{fwd} d\xi + \int_1^0 f^t_{rev} d\xi = 0. \qquad (2.18)$$

Now the chosen hardening functions take on the form of power laws using ξ to facilitate a smooth curve in the transition regions where transformation starts or ends:

$$f^t_{fwd}(\xi) = \frac{1}{2} a_1 \left(1 + \xi^{n_1} - (1 - \xi)^{n_2} \right) + a_3, \qquad (2.19)$$

$$f^t_{rev}(\xi) = \frac{1}{2} a_2 \left(1 + \xi^{n_3} - (1 - \xi)^{n_4} \right) - a_3. \qquad (2.20)$$

The model parameters $n_1 - n_4$ are are experimentally obtained and lie within the interval of $0 < n \leq 1$ as real numbers. Terms n_1 and n_3 correspond to the regions of transformation initiation, while n_2 and n_4 refer to regions transformation completion. Values of 1 provide a sharp transition in these regions while values less than 1 incrementally smooth the response.

For a more in depth derivation of the final thermodynamically consistent constitutive relations for a SMA through the Coleman-Noll procedure the reader is referred the following works

24

[58][59][60][61][63].

2.4.1 Transformation Criteria

Herein, the proposed model has covered the relevant thermodynamic requirements and evolution equations for an SMA, but the conditions for initiating transformation still remain. The basis for this definition relies on the principle of maximum transformation dissipation. This principle is similar to the maximum dissipation principle used in plasticty by Simo and Hughes [52], but now considers the energy dissipation inherent in the hysteretic behaviour of a given SMA transformation cycle [51]. Assuming this dissipative relationship during the evolution of transformation internal variables, the following arises,

$$\left[\boldsymbol{\sigma} : \boldsymbol{\Lambda}^t + p - f^t \right] \dot{\xi} = \pi^t \dot{\xi} > 0 \quad \forall \quad \dot{\xi} \neq 0. \tag{2.21}$$

Notice that the above inequality requires the effective thermodynamic driving force, π^t, to be positive during forward transformation and negative during reverse transformation (when ξ is either increasing or decreasing). From the work of Qidwai and Lagoudas, the next step is to define a critical thermodynamic driving force, Y^t, which determines the threshold for transformation [51]. Given the two directions of transformation, two transformation functions, $\Phi^t_{fwd}(\boldsymbol{\sigma}, T, \xi)$ and $\Phi^t_{rev}(\boldsymbol{\sigma}, T, \xi)$, are defined through these thermodynamic forces, Y^t_{fwd} and Y^t_{rev}. These functions prescribe a transformation surface in stress-temperature hyperspace to determine the thermoelastic region that transformation occurs. To start, the forward transformation surface Φ^t_{fwd} is represented through the following:

$$\Phi^t_{fwd} = \pi^t_{fwd} - Y^t_{fwd}. \tag{2.22}$$

The Kuhn-Tucker conditions are then applied to give an explicit requirement for forward transformation:

$$\dot{\xi} \geq 0, \qquad \Phi^t_{fwd} \leq 0, \qquad \Phi^t_{fwd}\dot{\xi} = 0. \tag{2.23}$$

25

Furthermore, the thermodynamic driving force is subject to changes with stress of which the sensitivity of that dependency is captured through the model parameter, D, which will be formulated and discussed further in Section 2.4.2. In terms of Y_{fwd}^t this is represented as,

$$Y_{fwd}^t(\boldsymbol{\sigma}) = Y_0^t + D\boldsymbol{\sigma} : \boldsymbol{\Lambda}_{fwd}^t, \tag{2.24}$$

where Y_0^t is the thermodynamic driving force at zero stress.

The same developments apply to reverse transformation as well where the transformation surface Φ_{rev}^t is represented through the following:

$$\Phi_{rev}^t = -\pi_{rev}^t - Y_{rev}^t, \tag{2.25}$$

Similarly, for Φ_{rev}^t the Kuhn-Tucker conditions are,

$$\dot{\xi} \leq 0, \qquad \Phi_{rev}^t \leq 0, \qquad \Phi_{rev}^t \dot{\xi} = 0. \tag{2.26}$$

and the same stress dependency applies for the reverse transformation critical thermodynamic force:

$$Y_{rev}^t(\boldsymbol{\sigma}) = Y_0^t + D\boldsymbol{\sigma} : \boldsymbol{\Lambda}_{rev}^t \tag{2.27}$$

2.4.2 Model Parameter Calibration

Calibrating the material properties for the SMA constitutive model is the next task imperative to characterizing a given SMA material. Through these following relationships, the scalar unknowns, ($\boldsymbol{\sigma}$, $\boldsymbol{\varepsilon}^t$, ξ, and g^t), can be solved for increments in strain and temperature. The model parameters are calibrated to match an experimental material response, of which a 1-D stress state with uniaxial loading is sufficient.

Firstly, the total strain in an SMA can be decomposed into three main contributing types,

namely, the elastic, thermal and transformation components. Using this, the following equation describes the stress-strain relation at any given instance throughout a load cycle,

$$\sigma = E(\xi) \left[\varepsilon - \alpha(T - T_0) - \varepsilon^t \right], \tag{2.28}$$

where $E(\xi)$ denotes the Young's modulus of the SMA which is a function of the martensitic volume fraction, ξ. Using a simple rule of mixtures between the austenitic and martensitic elastic moduli, E^A and E^M, the following equation arises,

$$E(\xi) = \left[1/E^A + \xi(1/E^M - 1/E^A) \right]^{-1}. \tag{2.29}$$

Next, the transformation strain, ε^t, can be prescribed using its evolution equation which varies depending on the direction of transformation, denoted by Λ^t (forward or reverse),

$$\dot{\varepsilon}^t = \dot{\xi}\Lambda^t; \quad \Lambda^t = \begin{cases} H^{cur}(\sigma)\mathrm{sgn}\,(\sigma); & \dot{\xi} > 0, \\ \varepsilon^{t-r}/\xi^r; & \dot{\xi} < 0. \end{cases} \tag{2.30}$$

The transformation function during forward (2.31) and reverse (2.32) transformation are,

$$\begin{aligned} \Phi^t_{fwd}(\sigma, T, \xi) &= (1 - D)\,|\sigma|\,H^{cur}(\sigma) + \frac{1}{2}\left(\frac{1}{E^M} - \frac{1}{E^A}\right)\sigma^2 + \rho\Delta s_0 T - \rho\Delta u_0 \\ &- f^t_{fwd}(\xi) - Y^t_0 = 0, \end{aligned} \tag{2.31}$$

$$\begin{aligned} \Phi^t_{rev}(\sigma, T, \xi) &= -(1 + D)\sigma\frac{\varepsilon^{t-r}}{\xi^r} - \frac{1}{2}\left(\frac{1}{E^M} - \frac{1}{E^A}\right)\sigma^2 - \rho\Delta s_0 T + \rho\Delta u_0 \\ &+ f^t_{rev}(\xi) - Y^t_0 = 0. \end{aligned} \tag{2.32}$$

The constitutive model parameters to be calibrated are the thermoelastic parameters for both the austenite and martensite phases $(E^M, E^A, \nu^A, \nu^M, \alpha)$, the parameters pertaining to the

27

maximum transformation strain, $H^{cur}(\sigma)$, and seven more parameters ($\rho\Delta s_0, \rho\Delta u_0, a_1, a_2, a_3, Y_0^t$ and D) detailing further characterization of the martensitic transformation. The thermoelastic constants are experimentally obtained from stress-strain curves in both distinct solid phases of martensite and austenite. Hardening coefficients, $n_1 - n_4$, are also implemented as a fitting tool to smooth the inflection points of the hysteresis plots where transformation starts and ends as detailed earlier in Section 2.4. Transformation temperature parameters are for a zero stress state and can then be used to calibrate the following five parameters $\rho\Delta u_0, a_1, a_2, a_3,$ and Y_0^t

$$a_1 = \rho\Delta s_0(M_f - M_s), \quad a_2 = \rho\Delta s_0(A_s - A_f),$$

$$a_3 = -\frac{a_1}{4}\left(1 + \frac{1}{n_1 + 1} - \frac{1}{n_2 + 1}\right) + \frac{a_2}{4}\left(1 + \frac{1}{n_3 + 1} - \frac{1}{n_4 + 1}\right),$$ (2.33)

$$\rho\Delta u_0 = \frac{\rho\Delta s_0}{2}(M_s + A_f), \quad Y_0^t = \frac{\rho\Delta s_0}{2}(M_s - A_f) - a_3.$$

The last two parameters to be calibrated, $\rho\Delta s_0$ and D, account for the slope of the transformation surface in stress-temperature space of the SMA phase diagram. Referring back to the Kuhn-Tucker conditions, the differential of the transformation function can be rewritten in a 1-D form.

$$\mathrm{d}\Phi^t = \partial_\sigma\Phi^t\,\mathrm{d}\sigma + \partial_T\Phi^t\,\mathrm{d}T + \partial_\xi\Phi^t\,\mathrm{d}\xi = 0.$$ (2.34)

A constant ξ and calibration stress σ^* are used for the subsequent solution of the stress-temperature derivatives in forward (2.35) and reverse (2.36) transformation,

$$\left.\frac{\mathrm{d}\sigma}{\mathrm{d}T}\right|_{\sigma=\sigma^*,\dot{\xi}>0} = \left.\frac{-\rho\Delta s_0}{\Lambda^t + \sigma\partial_\sigma\Lambda^t_{fwd} + \sigma\left(\frac{1}{E^M} - \frac{1}{E^A}\right) - \partial_\sigma Y^t_{fwd}}\right|_{\sigma=\sigma^*},$$ (2.35)

$$\left.\frac{\mathrm{d}\sigma}{\mathrm{d}T}\right|_{\sigma=\sigma^*,\dot{\xi}<0} = \left.\frac{-\rho\Delta s_0}{\Lambda^t + \sigma\partial_\sigma\Lambda^t_{rev} + \sigma\left(\frac{1}{E^M} - \frac{1}{E^A}\right) + \partial_\sigma Y^t_{rev}}\right|_{\sigma=\sigma^*}.$$ (2.36)

Given that the slope of the transformation surface is experimentally found to differ between forward and reverse transformation, the following form of Y^t can account for this when written

in 1-D,

$$Y_{fwd}^t = Y_{rev}^t = Y_0^t + D\sigma^* H^{cur}(\sigma^*) \tag{2.37}$$

where Y_0^t refers to the critical thermodynamic driving force at zero stress. These forward and reverse transformation slopes are specified as, C^M and C^A,

$$C^M = \left. \frac{-\rho\Delta s_0}{(1-D)\left(\Lambda^t + \sigma\partial_\sigma\Lambda^t\right) + \sigma\left(\frac{1}{E^M} - \frac{1}{E^A}\right)} \right|_{\sigma=\sigma^*}, \tag{2.38}$$

$$C^A = \left. \frac{-\rho\Delta s_0}{(1+D)\left(\Lambda^t + \sigma\partial_\sigma\Lambda^t\right) + \sigma\left(\frac{1}{E^M} - \frac{1}{E^A}\right)} \right|_{\sigma=\sigma^*}. \tag{2.39}$$

Through solving the above equations (2.38) and (2.39) for the remaining parameters $\rho\Delta s_0$ and D we obtain,

$$\rho\Delta s_0 = \left. \frac{-2\left(C^M C^A\right)\left[H^{cur}(\sigma) + \sigma\partial_\sigma H^{cur}(\sigma) + \sigma\left(\frac{1}{E^M} - \frac{1}{E^A}\right)\right]}{C^M + C^A} \right|_{\sigma=\sigma^*}, \tag{2.40}$$

$$D = \left. \frac{\left(C^M - C^A\right)\left[H^{cur}(\sigma) + \sigma\partial_\sigma H^{cur}(\sigma) + \sigma\left(\frac{1}{E^M} - \frac{1}{E^A}\right)\right]}{\left(C^M + C^A\right)\left[H^{cur}(\sigma) + \sigma\partial_\sigma H^{cur}(\sigma)\right]} \right|_{\sigma=\sigma^*}.$$

2.4.3 Constitutive Model Implementation in a Finite Element Framework

Given this thesis covers 3-D FEA modeling incorporating this SMA constitutive model scheme, a review of the numerical implementation is presented here. The implementation follows an incremental procedure of the evolution of ε^t using a backwards Euler integration method. For application to 3-D FEA, a convex cutting plane algorithm form of the return mapping algorithm (RMA) is used [49][50]. To review, a RMA, also denoted as a predictor-corrector scheme, is a numerical method which returns a trial stress state based on a predicted elastic state. In solid mechanics, a common name for this scheme is an elastic predictor-plastic corrector, as the prediction checks for crossing of the yield surface to ensure the proper governing equations are

implemented. In the case of the SMA constitutive model, that yield surface is implemented as the transformation surface, to determine when transformation is occurring. Given this framework, a thermoelsatic state of the material is predicted, meaning a given increment of strain and temperature are prescribed and the constitutive model outputs an increment of stress. Fundamentally, the method aims to satisfy the transformation consistency conditions, and thus transformation corrections are implemented when such conditions are violated. For efficient numerical implementation, modified versions of the RMA can be used based on two common integration algorithms which are a closest point project and convex cutting plane. Both methods are strain-driven and compute all relevant state variables using deformation history. They differ in the relaxation portion of their formulation. The closest point projection method develops a set of non-linear algebraic equations which are subsequently solved by the Newton-Raphson iteration method. The closest point projection is stable for convex yield surfaces and first-order accurate [49]. The convex cutting plane explicitly integrates the governing differential equations, providing more simplicity and computational efficiency [49]. To begin, the evolution equation can be discretized using the closest point projection algorithm

$$\boldsymbol{\varepsilon}^{t\,(k+1)}_{n+1} = \boldsymbol{\varepsilon}^{t}_{n} + (\xi^{(k+1)}_{n+1} - \xi_n)\boldsymbol{\Lambda}^{t}(\boldsymbol{\sigma}^{(k+1)}_{n+1}). \tag{2.41}$$

Then an iterative update follows,

$$\boldsymbol{\varepsilon}^{t\,(k+1)}_{n+1} = \boldsymbol{\varepsilon}^{t\,(k)}_{n+1} + \Delta\boldsymbol{\varepsilon}^{t\,(k)}_{n+1}. \tag{2.42}$$

By substition of (2.42) into (2.41) for iterations (k) and $(k+1)$ this provides

$$\Delta\boldsymbol{\varepsilon}^{t\,(k)}_{n+1} = (\xi^{(k+1)}_{n+1} - \xi_n)\boldsymbol{\Lambda}^{t}(\boldsymbol{\sigma}^{(k+1)}_{n+1}) - (\xi^{(k)}_{n+1} - \xi_n)\boldsymbol{\Lambda}^{t}(\boldsymbol{\sigma}^{(k)}_{n+1}). \tag{2.43}$$

The convex cutting plane method relaxes the dependence on transformation direction, $\boldsymbol{\Lambda}^{t}(\boldsymbol{\sigma}^{(k+1)}_{n+1})$,

instead focusing on the magnitude of transformation much unlike the closest point projection. The following simplification then follows,

$$\Delta\boldsymbol{\varepsilon}^{t(k)}_{\,n+1} = (\xi^{(k+1)}_{n+1} - \xi^{(k)}_{n+1})\boldsymbol{\Lambda}^t(\boldsymbol{\sigma}^{(k)}_{n+1}) = \Delta\xi^{(k)}_{n+1}\boldsymbol{\Lambda}^t(\boldsymbol{\sigma}^{(k)}_{n+1}). \tag{2.44}$$

The numerical solving for the constitutive model follows a local iteration for correction, while there still remains a global increment for the loading case. Thus previous equations can be rewritten in an incremental form, taking the notation of $n+1$ as the current loading increment and (k) as the current iteration,

$$\boldsymbol{\sigma}^{(k)}_{n+1} = \boldsymbol{\mathcal{C}}^{(k)}_{n+1}[\boldsymbol{\varepsilon}_{n+1} - \boldsymbol{\varepsilon}^{th}_{\,n+1} - \boldsymbol{\varepsilon}^{t(k)}_{\,n+1}]. \tag{2.45}$$

The two main inputs obtained from the global solver are increments in strain and temperature. Using the previously described modified return mapping algorithm, the constitutive relations for a SMA element are solved. This is done through an initialization where the iteration starts at (0) and a predicted thermoelastic state from (2.45) that assumes no evolution for the transformation internal variables,

$$\boldsymbol{\varepsilon}^{t(0)}_{\,n+1} = \boldsymbol{\varepsilon}^t_{\,n}, \quad \xi^{(0)}_{n+1} = \xi_n. \tag{2.46}$$

Next, violation of the transformation constraint, $\Phi^{t(0)}_{\,n+1} \leq 0$, is checked after the calculation of the transformation function using the prediction. Two cases arise from this: one being no violation followed by a subsequent acceptance of the prediction and continuation of the global solver; the other being a violation which results in a transformation correction procedure through the RMA to obtain $\Phi^t = 0$ to within a tolerance. During the process of iterative correction, the current strain and temperate are stagnated meaning,

$$\Delta\boldsymbol{\varepsilon}^{(k)}_{n+1} = \mathbf{0}, \qquad \Delta T^{(k)}_{n+1} = 0. \tag{2.47}$$

31

The following equation relates the differential of the constitutive stress-strain relation in (2.45) with both the discretized evolution equation (2.44) and the stagnation simplification (2.47),

$$\Delta\boldsymbol{\sigma}_{n+1}^{(k)} = -\boldsymbol{\mathcal{C}}_{n+1}^{(k)}\left(\Delta\boldsymbol{\mathcal{S}}\boldsymbol{\sigma}_{n+1}^{(k)} + \boldsymbol{\Lambda}_{n+1}^{t(k)}\right)\Delta\xi_{n+1}^{(k)}. \tag{2.48}$$

The transformation equations rely on key variables from the solution process, being stress, temperature and martensitic volume fraction as seen where the "+" sign refers to forward transformation and the "−" sign refers to reverse,

$$\Phi^t(\boldsymbol{\sigma}, T, \xi) = \pm\left[\boldsymbol{\sigma} : \boldsymbol{\Lambda}^t(\boldsymbol{\sigma}) + p(\boldsymbol{\sigma}, T) - f^t(\xi)\right] - \left[Y_0^t + D\boldsymbol{\sigma} : \boldsymbol{\Lambda}^t(\boldsymbol{\sigma})\right] = 0. \tag{2.49}$$

The next procedure aims to enforce the transformation function consistency condition such that the next iteration follows,

$$\Phi_{n+1}^{t(k)} + \Delta\Phi_{n+1}^{t(k)} = \Phi_{n+1}^{t(k+1)} \simeq 0. \tag{2.50}$$

Through the chain rule on the above requirement,

$$\Phi_{n+1}^{t(k)} + \partial_{\boldsymbol{\sigma}}\Phi_{n+1}^{t(k)} : \Delta\boldsymbol{\sigma}_{n+1}^{(k)} + \partial_{\xi}\Phi_{n+1}^{t(k)}\Delta\xi_{n+1}^{(k)} + \simeq 0 \tag{2.51}$$

Combining the relevant correction equations, the increment in stress (2.48) and the transformation requirement after the chain rule (2.51), we obtain,

$$\Phi_{n+1}^{t(k)} - \partial_{\boldsymbol{\sigma}}\Phi_{n+1}^{t(k)} : \boldsymbol{\mathcal{C}}_{n+1}^{(k)}\left(\Delta\boldsymbol{\mathcal{S}}\boldsymbol{\sigma}_{n+1}^{(k)} + \boldsymbol{\Lambda}_{n+1}^{t(k)}\right)\Delta\xi_{n+1}^{(k)} + \partial_{\xi}\Phi_{n+1}^{t(k)}\Delta\xi_{n+1}^{(k)} \simeq 0. \tag{2.52}$$

The correction in ξ can then be solved for the present iteration through (2.52),

$$\Delta\xi_{n+1}^{(k)} = \frac{-\Phi_{n+1}^{t(k)}}{A_2^t}, \tag{2.53}$$

where

$$A_2^t = \partial_\xi \Phi^{t\,(k)}_{n+1} - \partial_{\boldsymbol\sigma} \Phi^{t\,(k)}_{n+1} : \boldsymbol{\mathcal{C}}^{(k)}_{n+1} \left(\Delta \boldsymbol{\mathcal{S}} \boldsymbol{\sigma}^{(k)}_{n+1} + \boldsymbol{\Lambda}^{t\,(k)}_{n+1} \right).$$

Using this correction, the inelastic strain, $\boldsymbol{\varepsilon}^t$, can be updated using the previous incremental definition (2.13),

$$\boldsymbol{\varepsilon}^{t\,(k+1)}_{n+1} = \boldsymbol{\varepsilon}^{t\,(k)}_{n+1} + \Delta\xi^{(k)}_{n+1}\boldsymbol{\Lambda}^{t\,(k)}_{n+1}. \tag{2.54}$$

Through further iteration, the transformation function can be recalculated given updated transformation strains, elastic stiffness and stress until $\Phi^{t\,(k+1)}_{n+1}$ is smaller than a given tolerance or $\xi^{(k+1)}_{n+1}$ hits a bound of 0 or 1.

To summarize the presented convex cutting plane RMA for a 3-D FEA framework, Table 3 illustrates three distinct steps of initialization, elastic prediction and transformation correction [62].

Table 3: Numerical modeling of phase transformation in SMAs (convex cutting plane and return mapping algorithm) [62]

1. Initialize
a. Rotate all tensors from last increment n by $\boldsymbol{\mathcal{Q}}_{n+1}$.
b. Let $k = 0$, $\xi^{(0)}_{n+1} = \xi_n$, $\boldsymbol{\varepsilon}^{t\,(0)}_{n+1} = \boldsymbol{\varepsilon}^t_{n}$, $\mathbf{S}^{(0)}_{n+1} = \mathbf{S}_n$.

2. Elastic Prediction
a. $\boldsymbol{\sigma}^{(0)}_{n+1} = \boldsymbol{\mathcal{C}}^{(0)}_{n+1} \left[\boldsymbol{\varepsilon}_{n+1} - \boldsymbol{\alpha}(T_{n+1} - T_0) - \boldsymbol{\varepsilon}^{t\,(0)}_{n+1} \right].$
b. Find $\Phi^{t\,(0)}_{n+1}$.
c. IF $\Phi^{t\,(0)}_{n+1} \leq 0$ THEN EXIT (response elastic).

3. Transformation Correction
a. ELSE IF $\Phi^{t\,(0)}_{n+1} > 0$ CONTINUE.
b. Find $\Delta\xi^{(k)}_{n+1}$ via (2.53).
c. $\xi^{(k+1)}_{n+1} = \xi^{(k)}_{n+1} + \Delta\xi^{(k)}_{n+1}$, and $\boldsymbol{\varepsilon}^{t\,(k+1)}_{n+1} = \boldsymbol{\varepsilon}^{t\,(k)}_{n+1} + \Delta\xi^{(k)}_{n+1}\boldsymbol{\Lambda}^{t\,(k)}_{n+1}$.
d. IF $0 \leq \xi^{(k+1)}_{n+1} \leq 1$ THEN CONTINUE, ELSE set
   $\xi^{(k+1)}_{n+1}$ to violated bound and recalculate $\Delta\xi^{(k)}_{n+1}, \xi^{(k+1)}_{n+1}$, and $\boldsymbol{\varepsilon}^{t\,(k+1)}_{n+1}$.
e. $\boldsymbol{\sigma}^{(k+1)}_{n+1} = \boldsymbol{\mathcal{C}}^{(k+1)}_{n+1} \left[\boldsymbol{\varepsilon}_{n+1} - \boldsymbol{\alpha}(T_{n+1} - T_0) - \boldsymbol{\varepsilon}^{t\,(k+1)}_{n+1} \right].$
f. IF $\Phi^{t\,(k+1)}_{n+1} > TOL^t$ (conditions 2.23, 2.26) THEN CONTINUE ELSE EXIT.
g. Increment k and GOTO 3b.

2.5 Cavity Radiation Formulation

The following section covers the foundations of the heat transfer and cavity radiation methods used in ABAQUS/Standard. To address terminology, a cavity is defined as a surface composed of facets which are themselves sides of an element in the 2-D and axisymmetric case or in 3-D they consist of the face of a solid element or surface of a shell element [68]. Cavity radiation occurs when two facets within a geometry are in view of each other and thus exchange heat through radiation. The relevant theory and background for the upcoming governing equations can be found from the well-known works of Holman as well as Siegel and Howell [66][67].

To start, gray body radiation assumes that the monochromatic emissivity of a body is independent of wavelength [66]. The term monochromatic means of a single wavelength or frequency meaning the monochromatic emissivity refers to the ratio of emissive power of the gray body to the emissive power of that of a black body given the same wavelength and temperature. This emissivity ranges from $0 < \epsilon < 1$ for a gray body, while being defined as $\epsilon = 1$ for a black body.

$$\epsilon_\lambda = \frac{E_\lambda}{E_{b\lambda}} \tag{2.55}$$

Other assumptions are that only diffuse reflection, or the scattering of an incident ray on a surface at many angles as opposed to only one, is considered and attenuation of radiation within the medium of the cavity is neglected. For a single cavity facet, the radiation flux per unit area can be prescribed as,

$$q_c^i = \frac{\sigma \epsilon_i}{A_i} \sum_j \epsilon_i \sum_k F_{ik} C_{kj}^{-1} [(\theta_j - \theta^Z)^4 - (\theta_i - \theta^Z)^4] \tag{2.56}$$

where the term Cij is defined as:

$$C_{ij} = \delta_{ij} - \frac{(1 - \epsilon_i)}{A_i} F_{ij} \tag{2.57}$$

Here i and j refer to the facets with A_i being the area of facet i, ϵ_i and ϵ_j being the emissivities of facets, σ being the Stefan-Boltzman constant, F_{ij} being the view factor matrix, θ_i and θ_j being the temperatures of the facets, θ^Z being the absolute zero temperature, and δ_{ij} symbolizes the Kronecker delta.

As an additional note, although not explicitly mentioned in the ABAQUS/Standard Theory Manual, a method of ray tracing must be used to graphically track the ray projections occurring during these cavity radiation calculations. Common types of ray tracing are path tracing, ray casting, recursive ray tracing and scanline rendering. To compare two of these, path tracing is a higher fidelity and thus more computationally expensive scheme that uses a Monte Carlo method to integrate all of the illuminance or rays arriving at a single point pixel by pixel [70]. On the other hand scanline rendering offers a row-by-row basis using scan lines which is less accurate but more computationally efficient [71].

Next, view factor is a term used to relate the amount of energy exchanged between two surfaces. View factor calculation is quite complex beyond simple geometries, however, ABAQUS/Standard offers a formulation that accounts for radiation blocking and symmetry. For closed formed analytical relations of view factors for different geometries the reader is referred to the works of Siegel and Howell [67][69]. Generally, the view factor between two facet areas is defined as,

$$F_{ij} = \int_{A_i} \int_{A_j} \frac{cos(\phi_i)cos(\phi_j)}{\pi R^2} dA_i dA_j \tag{2.58}$$

where Figure 16 illustrates some of the relevant terms [68].
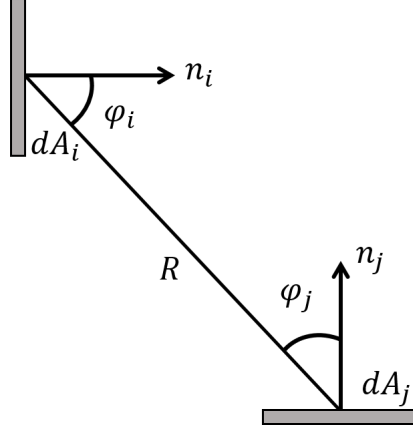
Figure 16: View factor calculation diagram (modified from [68])

R is the distance between areas A_i and A_j, and the two angles formed by R and the vectors normal to the area surfaces are ϕ_i and ϕ_j. Since area is incorporated in this calculation of view factor, the previous radiation equation (2.1) would simply be adjusted to avoid double counting. As a note, this equation is accurate in the case that areas are small in relation to the distance between them. The equation can then be simplified to:

$$F_{ij} = \frac{A_i cos(\phi_i) A_j cos(\phi_j)}{\pi R^2} \qquad (2.59)$$

When it comes to the mesh of an FEA model, as mentioned previously cavities are comprised of a group of element faces or facets which each individually follow this area view factor calculation. Additionally, linear and quadratic elements perform similarly for view factor calculations as the midside nodes are ignored.

Two types of cavities exist in the FEA definition of cavity radiation, open and closed. Closed cavity radiation refers to a completely enclosed geometry with associated surfaces not radiating heat to the environment. Open cavity radiation allows the definition of an ambient temperature to the medium for the surfaces to radiate heat to if they are in view of space. The method used to check accuracy of these view factor calculations is a geometric check on a fully enclosed

36

cavity:

$$\frac{1}{A_i} \sum_j F_{ij} = 1 \tag{2.60}$$

During closed radiation a tolerance is specified on the deviation from one in this equation, while for an open cavity radiation case the deviation from one over this tolerance represents the fraction radiating from the facet to the environment.

Moving back to the radiation flux formulation, the method of discretizing and approximating the heat transfer problem involving cavity radiation must now be addressed. For this, the nodal temperatures of the cavity surface are required, of which the individual facets are considered isothermal. The temperature radiation power is defined as,

$$\eta_i = (\theta_i - \theta^Z)^4, \eta^N = (\theta_N - \theta^Z)^4 \tag{2.61}$$

where facet numbers are denoted by the subscript i and nodal numbers are represented with N. Then the average facet temperature radiation power follows as,

$$\eta_i = \sum_N P_i^N \eta^N \tag{2.62}$$

where the limit of N is the number of nodes comprising the facet and P_i^N is a term referring to the contribution factor for a given facet based on its area integration,

$$P_i^N = \frac{1}{A_i} \int_{A_i} N_i^N dA_i \tag{2.63}$$

where N_i^N are the interpolation fuctions for facet i. Finally the radiation flux into a facet takes the form of,

$$Q_i = q_c^i A_i = \sum_j R_{ij}(\eta_j - \eta_i) \tag{2.64}$$

where the term R_{ij} is expanded to,

$$R_{ij} = \sigma \epsilon_i \epsilon_j D_{ij} \tag{2.65}$$

and the term D_{ij} is:

$$D_{ij} = \sum_k F_{ik} C_{kj}^{-1} \tag{2.66}$$

Combining these equations the radiation flux into a facet i is simplified to,

$$Q_i = \sum_j \overline{R}_{ij} \eta_j \tag{2.67}$$

with the term $\overline{R}_{ij}$ defined as:

$$\overline{R}_{ij} = R_{ij} - (\sum R_{ik}) \delta_{ij} \tag{2.68}$$

Each of the nodal contributions from this radiation flux formulation on each facet is now written as,

$$Q_i^N = \int_{A_i} q_c^i N_i^N dA_i = P_i^N Q_i \tag{2.69}$$

where this can be summed to obtain the total radiation flux at a given node:

$$Q^N = \sum_i Q^N = \sum_i P_i^N Q_i \tag{2.70}$$

By substituting 2.62 and 2.67 into 2.70, we arrive at the final nodal radiation flux,

$$Q^N = \sum_M \overline{R}^{NM} \eta^M \tag{2.71}$$

where $\overline{R}^{NM}$ is:

$$\overline{R}^{NM} = \sum_i \sum_j P_i^N \overline{R}_{ij} P_j^M \tag{2.72}$$

Similarly, this is fully written out in terms of the unit area of a facet as shown earlier in 2.56.

2.6 Coupled Thermal Radiation & Shape Morphing Modeling

An inherent coupling exists between the geometry of the radiator and its temperature, due to the radiation equations dependence on view factor. For example, as the radiator bends open it rejects more heat, which in turn will further cool the panel. Due to the cavity radiation definition requiring a view factor calculation for each new geometry of the radiator, this provides a challenge to traditional methods of modeling coupled temperature-displacement methods. To approximately model this coupling a combined thermal-displacement solution procedure was developed by Chris Bertagne which separately runs the thermal and displacement solutions [3][7]. The basis of this framework is to decompose the coupled problem into these two analyses, transferring data between them for a given time increment to approximate the coupled behaviour.

A schematic summarizing this model scheme can be found below in Figure 17, where red arrows correspond to temperature data transfer and blue arrows represent structural data transfer. The ordering of analyses can be followed through the numbering in the top-left corner of each box and the solution time increment is denoted in parentheses. First, an initial step is run to initialize the temperature and geometry fields in which no changes in temperature or geometry are observed. Next a thermal analysis is executed to determine the variation in temperature across the radiator for a given time increment.

The resulting temperature field is then transferred to a structural analysis. The SMA response is then captured based on the provided temperature field, providing an updated deformed shape of the radiator. This newly deformed geometry is sent back to the thermal analysis, advancing the global simulation time, for subsequent recalculation of view factor matrices and updated temperature field upon which this trading pattern continues until the total time increment meets the desired run time.
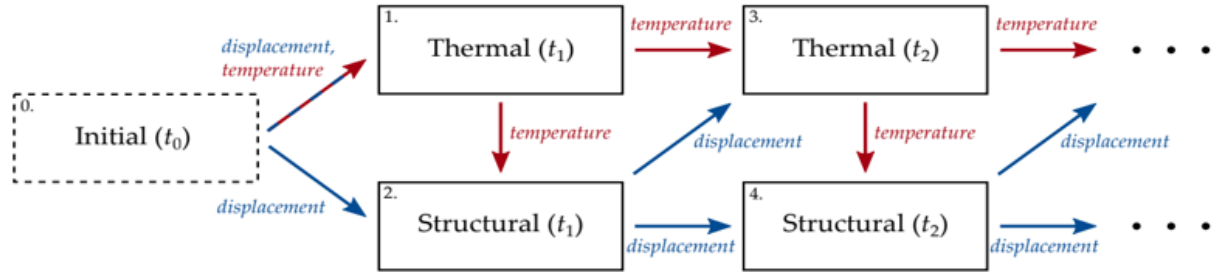
Figure 17: Coupled thermal-displacement framework [7]

This model scheme is implemented in this work with a couple of variations for the updated morphing radiator model. In previous work, a simple heat flux was applied to the root of the radiator [7], when in reality the radiator will be part of a thermal control system that incorporates a working fluid to transfer heat from a space crew cabin to the radiator. The current model accounts for this through an approximate bulk fluid flow detailed further in Section 3.1. Particularly, the driving factor for temperature change throughout the thermal analyses is an incremental linear change in the fluid inlet temperature. Given this change, the temperature is linearly varied to cycle the morphing radiator through the operational temperature bounds. Additionally, each thermal step is run to steady state. Although not presented in this work, transient steps were investigated for more accuracy but were found to provide considerably lower panel temperatures when compared to experimental tests in a model validation study detailed in Section 4.2.

The time increment size selection is also an important factor in this coupled model scheme. Decreasing the time step increases the number of increments required to reach the total run time, adding significant computational time due to the cost of creating new analysis steps. However, a large enough time step can lead to poor modeling of the coupled behaviour and subsequent inaccuracies in the model. This can be directly seen in the current framework of the morphing radiator model which uses linear varying of the fluid inlet temperature. For this example, a high enough time step leads to large changes in fluid temperature between increments which in turn

can lead to large changes in geometry of the morphing radiator. Ideally the temperature change remains at a reasonable range so as to allow small geometry changes of the radiator to ensure the capturing of the coupled behaviour of this application. Thus, a balance must be struck to obtain accurate modeling of the coupled behaviour of the problem along with a feasible run time. Bertagne conducted a variety of verification studies to ensure the model accuracy for a variety of differing time steps, which were used as a foundation for the time step selection in the present model (Δt =45 seconds) [65]. To give perspective of the chosen incremental step time, the global step time is 4,050 seconds or 67.5 minutes.

3. THE MORPHING RADIATOR MODEL

This section covers the development of a FEA model for the morphing radiator detailing components, assumptions, boundary conditions and mesh selection. The ultimate goal of this model is the implementation as a design tool for optimizing the performance of the morphing radiator. Many contributions went into selecting key features of the model and will also be discussed here.

3.1 FEA Model Setup

First, the full assembly for the morphing radiator will be addressed along with outlines of each component and the relevant justifications for modeling methods. Using the combined thermal-displacement scheme mentioned in Section 2.6, a FEA model of the radiator was developed which originates as a closed radiator and cycles the fluid inlet temperature to open and close. Figure 18 below illustrates the key components of the model. SMA wires are wrapped around the outside of the composite panel, two aluminum endcaps close off the ends of the cylindrical panel and the radiator panel is mounted to a thermal joint. Inside the thermal joint is a fluid channel which will drive the temperature change of the radiator throughout the analysis. Propylene glycol is the chosen working fluid for this model and the maximum and minimum temperature ranges are determined by the operational temperatures of the fluid such as freezing point. To save computational time, only half of the radiator is modeled using symmetry about the YZ-plane. Unless otherwise specified, all shells were modeled with 3-node or 4-node reduced integration general-purpose shell elements (S3R, S4R), while 3-D components used 8-node linear brick continuum elements (C3D8).
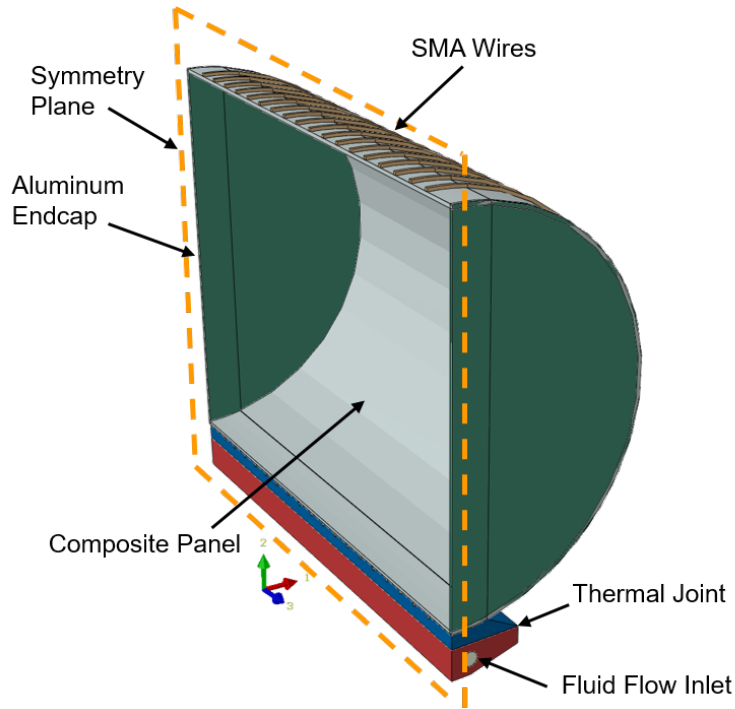
Figure 18: Diagram of radiator model

In normal operation the thermal joint is comprised of two components which are designed to break contact with the fluid channel in adverse heating conditions through an SMA plug so the thermal control system does not absorb unwanted heat at extreme temperatures. Examples of possible adverse heating conditions are solar absorption from prolonged exposure to the sun combined with dust collection increasing the absorptivity of the radiator. For this study, the thermal joint is simply modeled as a mounting interface and conduction path for the fluid channel into the panel, capturing the thermal resistance stack-up of the system. Figure 19 below displays the thermal joint assembly, comprised of a fluid flange on the bottom which contains two eighth inch diameter fluid channels, and a radiator flange on top which interfaces with the composite panel. Note that the mesh refinement is not critical as these components are non-load bearing and simply act as conduction paths for the fluid into the radiator.
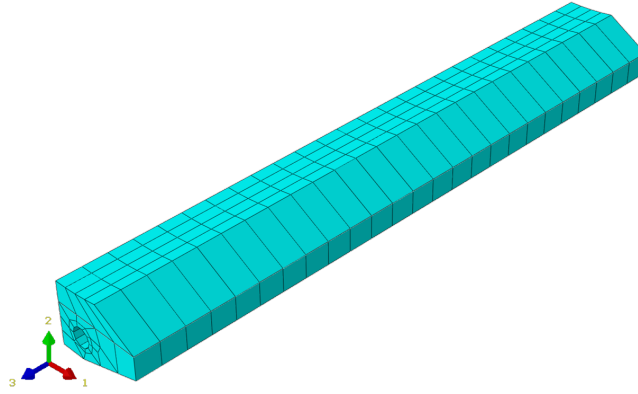
Figure 19: Thermal joint assembly mesh

The model currently approximates fluid flow using forced convection heat transfer elements with a constant mass flow rate. Thus, by setting the inlet temperature a simulated forced convection fluid flow is achieved, giving bulk fluid motion. Using this tool, the fluid inlet temperature is linearly varied throughout the analysis to cycle between the maximum and minimum temperatures. This fluid model was verified by performing a simple heat balance through the second law of thermodynamics. A surface heat flux was applied to the exterior of the flow channel to provide a corresponding temperature increase down the length of the channel. It was found that energy was conserved as the difference between the inlet and outlet heats equated to the applied heat. Figure 20 gives a representation of the mesh for the fluid channel.
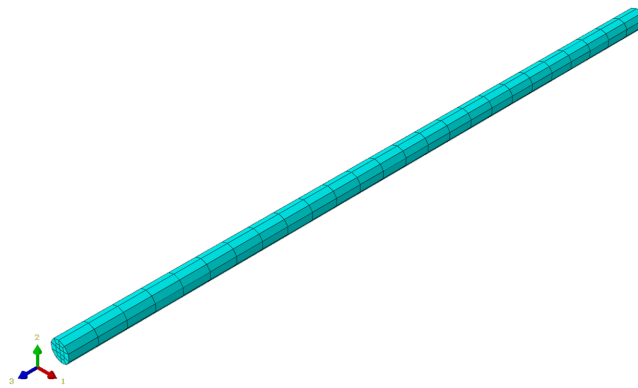

Figure 20: Flow tube mesh

44

The SMA drawing form is another key design selection for this model which will be detailed further in Section 3.2. SMA wires were selected as the drawing form and the starting point for total number of SMA wires and their diameter is calculated to match the same effective area of previous experimental tests using 0.2032 mm thick strips [6]. Furthermore, the wires are simplified to a square geometry to provide a definitive contact surface between the radiator panel and wires. A small length of the wires is tied to the top region of the composite panel that represents the terminal block that clamps the wires, so they are taught against the panel. This terminal block provides a needed boundary condition so the wires can react against the panel as they shrink, bending it open. Lastly, a small sliding contact definition is modeled between the wires and the composite panel with an approximate coefficient of friction of 0.3 based on literature covering contact between graphite-epoxy composites and different metals [64]. Figure 21 shows a single wire to illustrate the geometry and mesh, where 8-node linear brick elements for incompatible modes (3CD8I) elements were used. It was found that for this bending dominated application this incompatible mode element provided the most consistent convergence over other linear and quadratic choices. Also, a local material orientation was assigned to align the primary axis in the circumferential direction of the wire for numerical implementation of the SMA constitutive model.
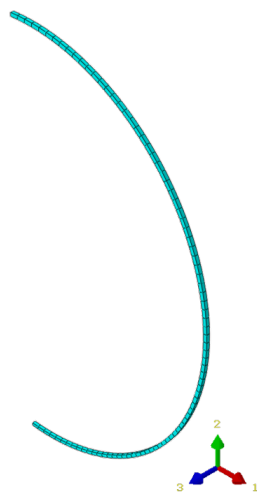

Figure 21: SMA wire mesh

The composite panel is modeled as a shell with a corresponding composite layup definition in Abaqus. Dimensions are a 3.32 in outer diameter, 3.25 in inner diameter and a 3 in length. Within this definition the ply orientations, ply thickness and material properties are specified. Section 3.2 covers the calibration for the composite orthotropic stiffness properties based on experimental 4-point bend test data. The ply thickness is driven by the as manufactured thickness of the composite layup and is thus prone to slight variations. As a basis for future design work, this tolerance is carefully considered with both a nominal value and upper limit tolerances being used for geometric trade studies. Figure 22 illustrates the mesh for the panel.
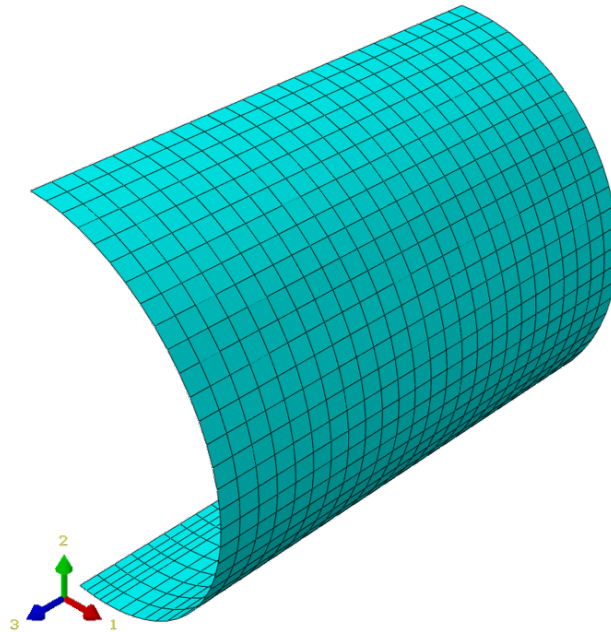
Figure 22: Composite panel mesh

Two aluminum end caps are modeled as shells on either end of the radiator. Their primary role is to minimize heat rejection in the closed configuration of the radiator with a secondary effect of acting as fins, rejecting heat in the open configuration. With this work focusing on a single panel system, two end caps are required to fully enclose the radiator; whereas in an array of radiators with multiple panels in series a single end cap can be used between panels to minimize mass. The mesh is critical for these components due to the ray tracing calculations

46

mentioned earlier in Section 2.5, meaning a poor mesh can allow heat leaking through small inaccuracies in the end cap outline mesh. Thus, it is a key modeling practice to refine the mesh on the boundary of the end cap until the heat rejection converges in the closed configuration. Figure 23 below shows the chosen mesh which is sufficient to meet these requirements.
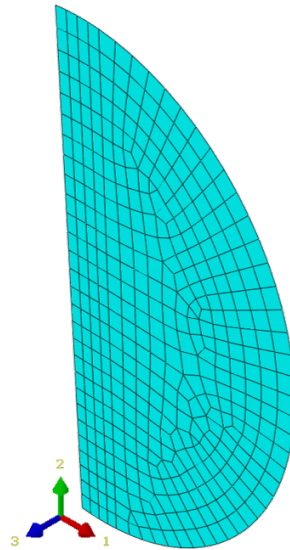
Figure 23: End cap mesh

Two geometries were investigated with the same composite layups to compare the feasibility of each. The geometries differ only in the bottom region where they would interface with a mounting feature. The first is an omega shape where the main attraction of this design is to fit the thermal joint within the region carved out by the omega feature, as well as increase the contact area for conductance. The other geometry is a simple circular shape, with no changes in radii. The benefit of this shape is a nice homogeneous cylinder without changes in radii that could cause regions of stress concentration. Both can be visualized below in Figure 24. The reasoning for investigating both geometries is that they each have been posed as possible designs for this morphing radiator, and this design process aims to verify which is the most optimal one to use.

47

Figure 24: Two chosen radiator geometries: omega on left, circular on right
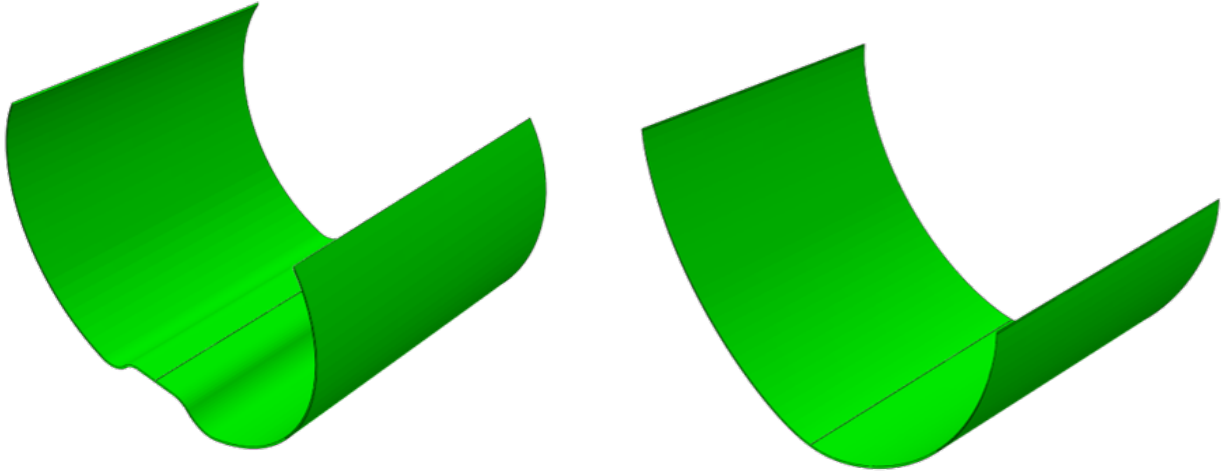
3.2 Wire vs. Strip Trade Study

As the SMA is responsible for the actuation of the radiator, it is imperative to determine the best drawing form. Thus, a trade study was conducted to determine the optimal SMA drawing configuration, wire or strip. The importance of this analysis is to ensure that the average temperature in the SMA is maintained even in a worst case of imperfect conduction between the SMA and the composite panel. This is critical since the temperature of the SMA drives phase transformation and corresponding deflection of the radiator. To simulate this, a 2D thermal analysis was conducted with an SMA wire or strip sandwiched between MLI and the composite panel. A temperature boundary condition of 300 K was set at one end of the composite panel, while the environmental temperature was fixed at 100 K. Figure 25 below shows a 3D diagram of the physical representation of this analysis.
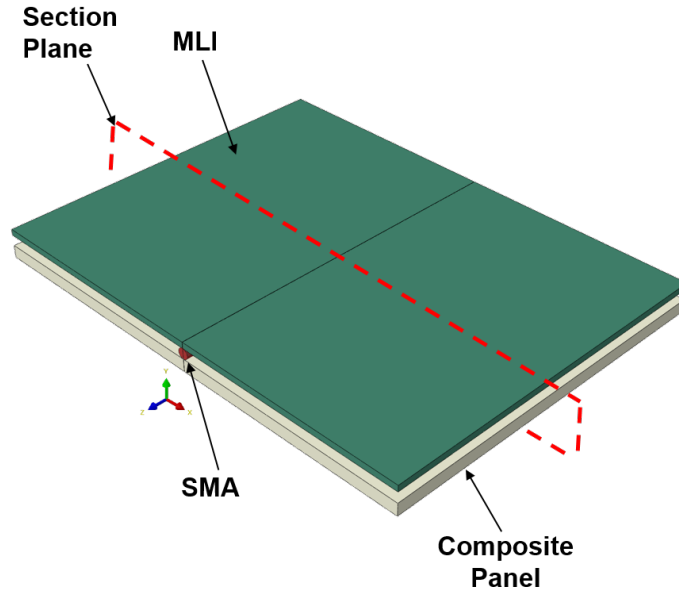
Figure 25: Wire vs. strip analysis

Four cases were investigated, alternating the presence of conduction and insulation. Figure 26 shows a summary of the average temperature in the SMA for each case while Figure 27 displays the corresponding temperature fields. In both case 1 and 3 with and without insulation, the conduction dominates the temperature in the SMA. In case 2 when there is no conduction or insulation, the average temperature in both SMA drawing forms drops drastically from the initial applied temperature boundary condition. However, when the MLI is added in case 4, the average temperatures in both the SMA wire and strip is maintained to the same degree. This demonstrates that the insulation allows the radiation from the composite panel to effectively heat the SMA in a scenario of imperfect conduction. Additionally, these results illustrate that both wires and strips perform similarly and are viable selections for this application.

Cases	Strip	Wire
Tie Conduction (1)	299 K	299 K
No Conduction (2)	247 K	246 K
MLI Tie Conduction (3)	299 K	299 K
MLI No Conduction (4)	295 K	295 K

Figure 26: Average temperature results for all case studies
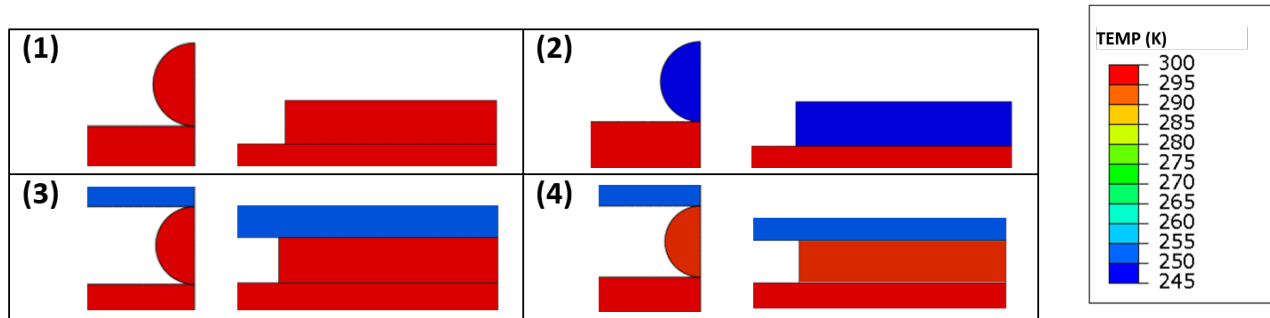
Figure 27: Temperature contour plots of each case with and without conduction or insulation

3.3 Composite Property Validation

Following experimental results for composite strips under 4-point bend testing done by Priscilla Nizio, a simulation was done to match the same setup. Figure 28 below shows the experimental and computational setups where the top crossheads displace while the bottom crossheads are fixed. The simulation was carried out for a variety of different composite layups, and composite moduli were adjusted to match experimental force-displacement curves. This matching can be seen in Figure 29. Below is a list of the composite layups that were validated against experiment:

- Layup 1: $[0/0/0/0]$
- Layup 2: $[90/90/90/90]$
- Layup 3: $[90/0/0/90]$
- Layup 4: $[90/45/0/0/45/90]$

Figure 28: Experimental and computational 4-point bend test diagram

Figure 29: 4-point bend test experiment (red) vs. simulation (blue) results

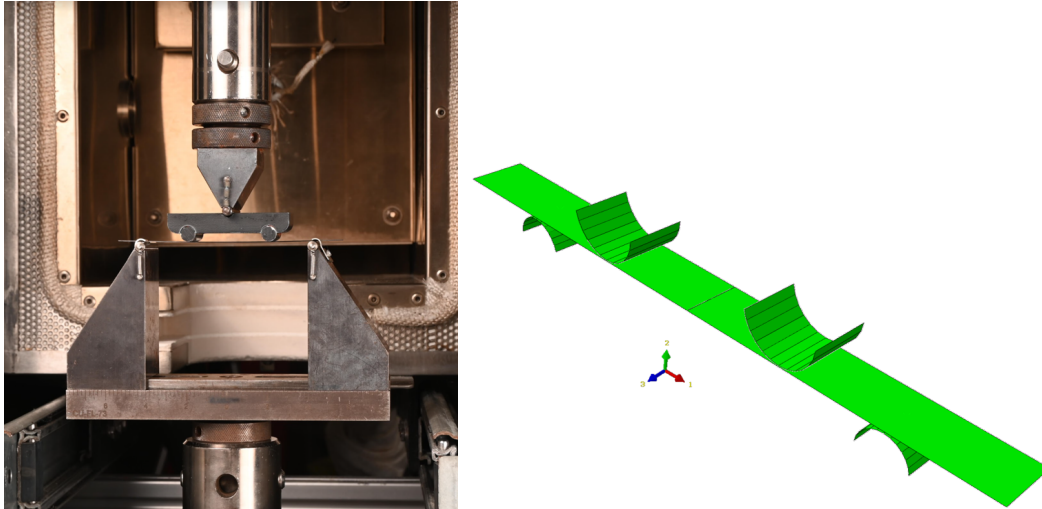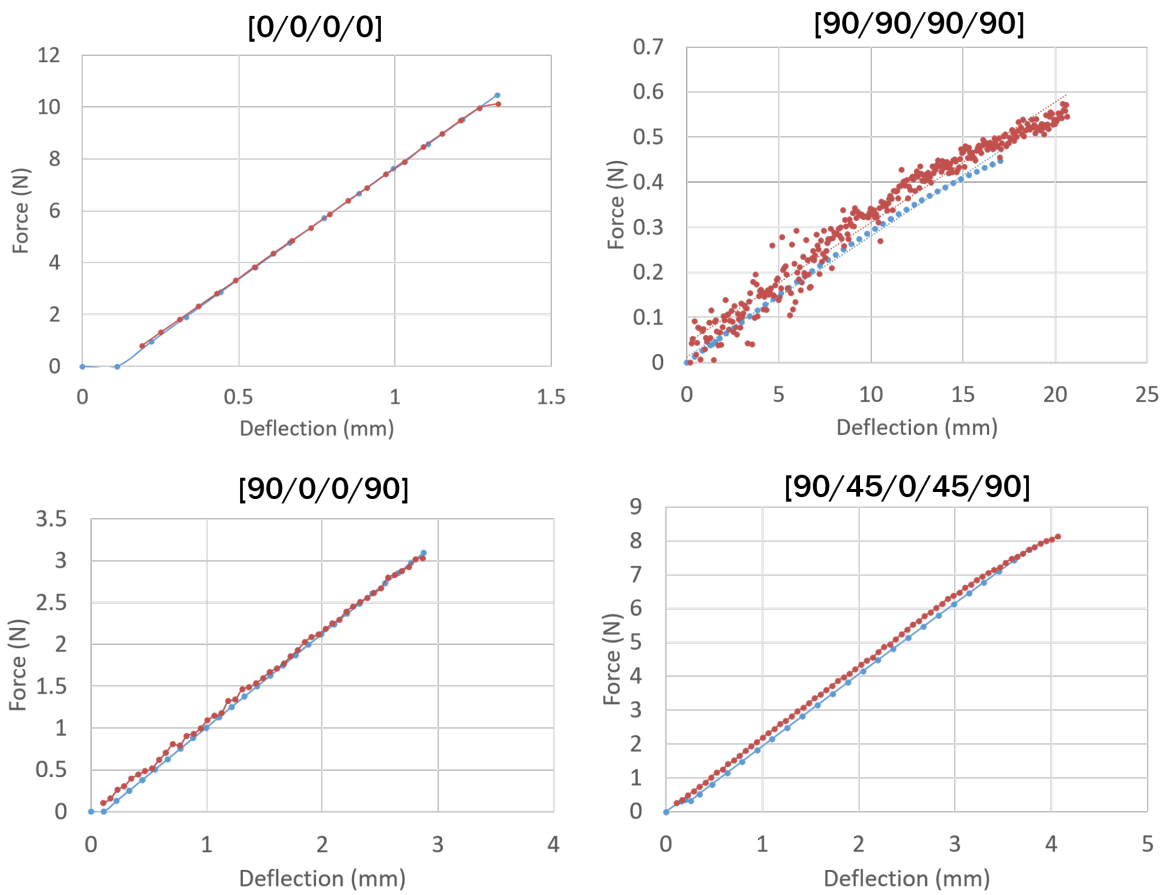The first two layups, 1 and 2, served as a calibration for both the 0° and 90° properties of the composite lamina, where the modulus was adjusted until the model matched experimental force displacement responses. Using this calibration, the following layups, 3 and 4, validated these properties by the subsequent agreement with experimental results. As a small note, the shear modulus was also calibrated with layup 4 given the added 45° layers and backed up by literature on graphite-epoxy shear modulus properties [27]. Final modulus properties were $E_{11} = 335$ GPa (manufacturer: 558 GPa), $E_{22} = 2.45$ GPa (manufacturer: 4.66 GPa), and $G_{12} = 1.5$ GPa.

3.4 Mesh Convergence Study

A mesh convergence study was conducted to identify the accuracy of the mesh size of the model. Particularly, there are two key features to verify, the composite panel and the SMA wires. The composite panel is responsible for the majority of the heat rejection of the thermal control system, along with providing a temperature to the SMA wires. Furthermore, the maximum stress in the composite is isolated at a region of stress concentration where the panel mounts onto the thermal joint. The SMA wires actuate the radiator panel and are dependent on stress and temperature to determine the degree of transformation that occurs. For these reasons, it is critical to ensure that both meshes are accurate and this has been done herein by tracking outputs of maximum and minimum heat rejection, maximum closed angle, and maximum failure stress factor. The key takeaway is that there are marginal changes in all tracked outputs with increased mesh refinements as shown in Table 4. All outputs achieve 2% or less change between refinements at the finest mesh, demonstrating an accurate modeling of the proposed operation of the radiator.

Table 4: Mesh refinement results

Output	# of Elements (Panel,Wires)	% Change
Maximum Failure Stress	560, 1260	-
	850, 1584	1.49%
	1485, 2088	0.172%
Maximum Q	560, 1260	-
	850, 1584	2.49%
	1485, 2088	1.42%
Minimum Q	560, 1260	-
	850, 1584	2.32%
	1485, 2088	1.40%
Maximum Closed Angle	560, 1260	-
	850, 1584	3.22%
	1485, 2088	2.00%

Runtime is another metric that helps facilitate the mesh size selection process and is of importance in this model due to the costly nature of the constitutive modeling for the SMA wire elements and the ray tracing for radiation of the composite panel elements that both add considerable computational time. To outline the most noticeable mesh refinement result, Figure 30 shows the maximum failure stress factor plotted against total runtime. This demonstrates a large relative improvement in accuracy with only a small added runtime of 1 hour, whereas when continuing to refine only small variations occur for 2 more hours of runtime. This justifies the usage of the middle seed size for all future results. As a final note on the mesh convergence study, this model is particularly sensitive to mesh refinement. At times, the model would diverge under mesh sizes inbetween two meshes that are known to converge. Likely factors of this are the complexity of contacting wires against the composite panel, along with the SMA constitutive modeling of the SMA wires under the combined contact and compressive loadings.
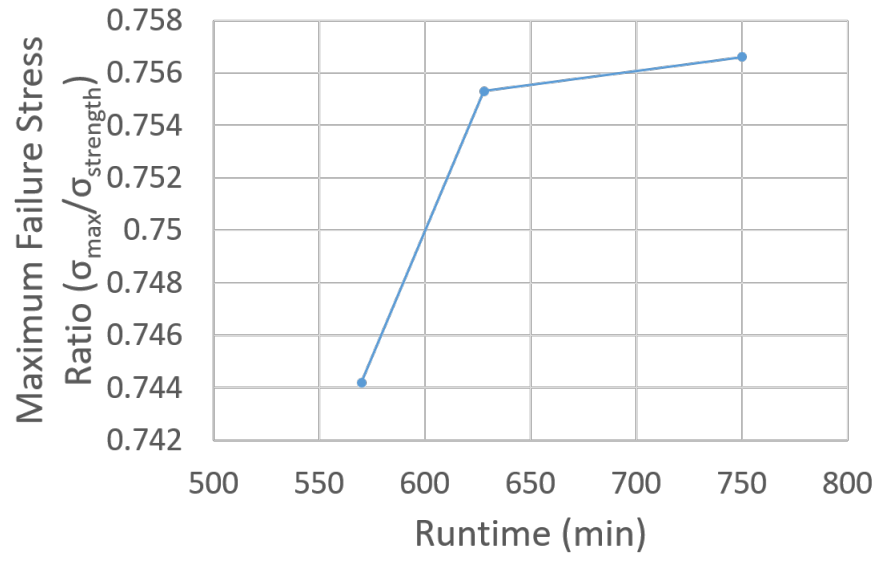
Figure 30: Panel seed size effects on maximum failure stress factor vs. runtime

4. RESULTS & INSIGHTS

This next section presents the results from a variety of computational studies including a validation of the proposed coupled thermomechanical model, a geometric trade study to optimize the radiator panel shape and composite layup, as well as a design of experiments to improve the morphing radiator performance through SMA wire number and properties.

4.1 Composite Trade Study of Panel Mechanical Performance

A composite trade study was conducted, trading between turndown and maximum failure stress, with the primary goal of answering two major questions: which radiator geometry is better and what is the optimal composite layup? Thus, two main outputs were extracted which are the turndown of the radiator as well as the maximum failure stress factor throughout all the plies in the composite. To calculate the total turndown, the radiation over the entire surface of the radiator was summed for various open angles and divided by the minimum heat rejection occurring at the closed state of the radiator. To calculate the maximum failure stress factor, the maximum stress for each direction was compared to its corresponding directional failure strength, and the maximum value out of all those ratios was taken as the maximum failure stress factor. The method used to actuate the panel in this trade study was the pulling on a set of wires in contact with the composite panel, displayed in Figure 31.
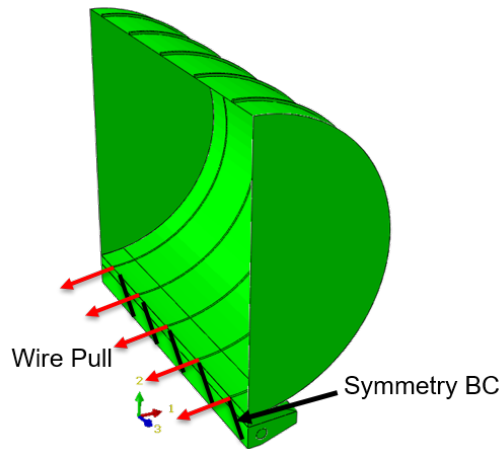

Figure 31: Geometric trade study model formulation

The following results will demonstrate the shortcomings of the omega shaped radiator geometry as the circular geometry is able to open much more (as indicated by an increased turndown) before failing (aka exceeding a stress factor of 1). This can very clearly be seen in Figure 32 which plots the first instance of failure for both the circular and omega geometries of the radiator given a [90/45/0/-45/90] layup. The omega geometry is failing at lower open angles largely due to the high stress concentration at the omega feature that changes radii and can be visualized by the red region failing in the 90° tensile direction. The following contour plot is a maximum envelope meaning it provides the maximum stress in the chosen direction of the local composite coordinate system throughout all the plies.
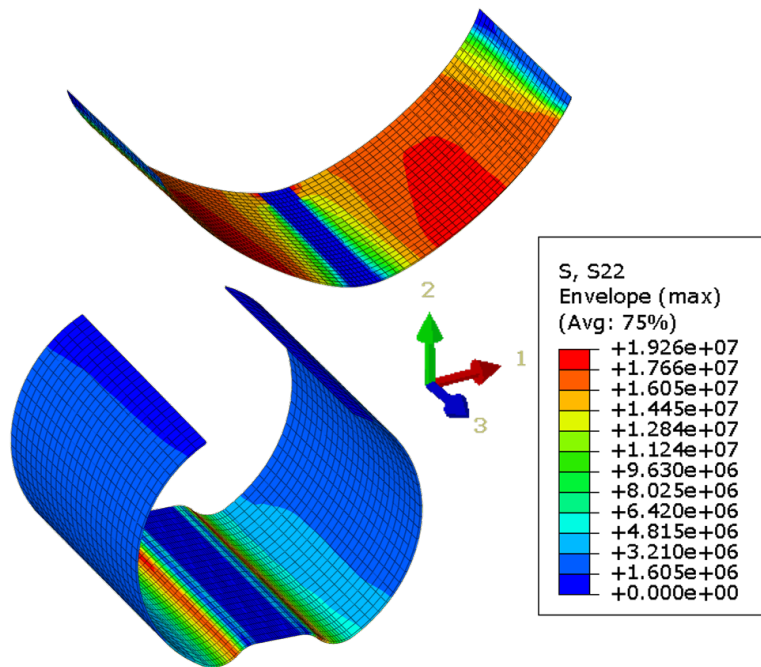
Figure 32: First instance of failure for omega and circular geometries given a [90/45/0/-45/90] composite layup (contour plot of local composite 90° direction maximum tensile stress throughout all plies)

To visualize and compare the performance of each composite layup, the turndown was plotted against the failure stress factor determined by the aforementioned failure criteria. This was done for increasing view factor as the radiator starts from a state of being fully closed to fully open.

56

A dashed line is drawn to indicate a safety factor of 1 and a safety factor of 1.5. Each black line corresponds to the results for a given composite layup, defined by the layup number in the list below.

- Layup 1: [90/45/0/45/90]

- Layup 2: [90/45/0/-45/90]

- Layup 3: [90/45/0/0/-45/90]

- Layup 4: [90/45/-45/-45/45/90]

- Layup 5: [90/45/-45/0/0/45/-45/90]

Figure 33 shows the results for the circular geometry while Figure 34 shows the results for the omega geometry.
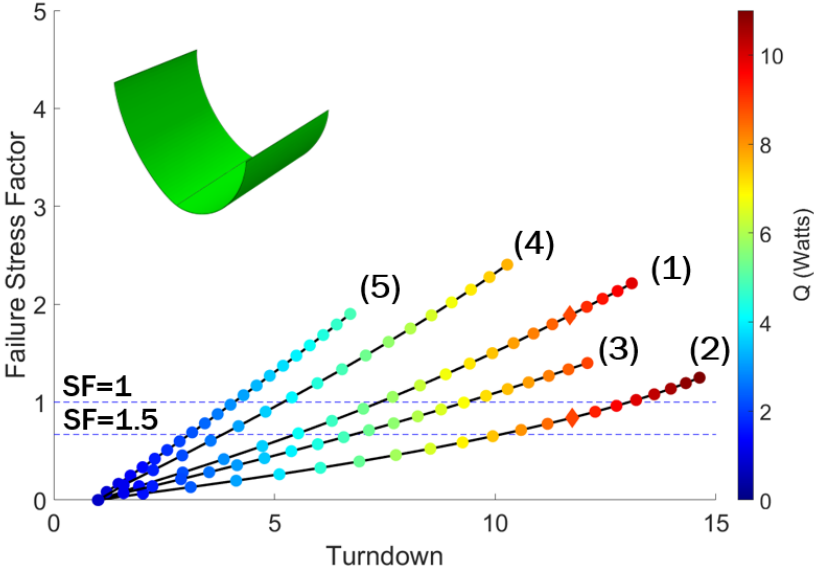

Figure 33: Plot of circular geometry failure stress factor vs. turndown for various composite layups (diamond represents 180° open angle)
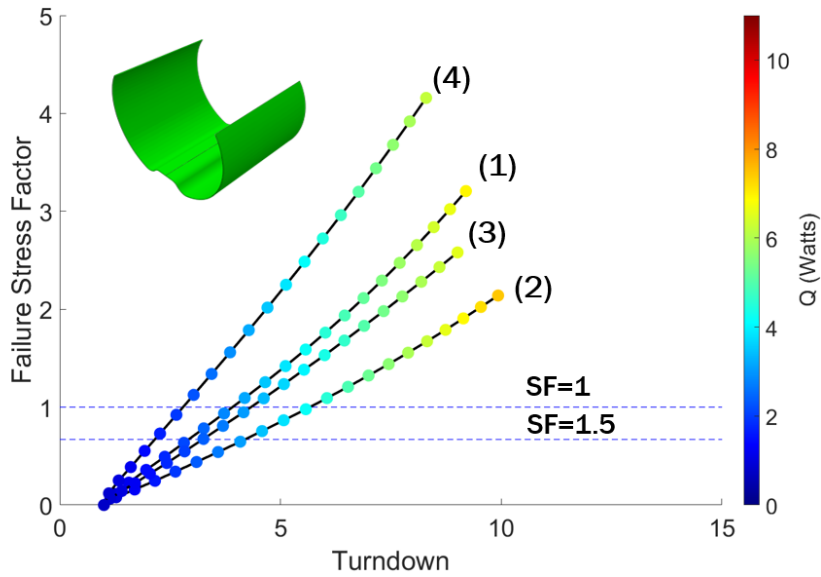
Figure 34: Plot of omega geometry failure stress factor vs. turndown for various composite layups

As a small note, layup 5 had difficulty converging for the omega feature, meaning there are only four layups plotted in Figure 34. The best performing layup that maximizes turndown while minimizing failure stress factor appears to be layup 2 for both geometries, which is the [90/45/0/-45/90]. The maximum turndown for this layup reaches 9.94 with a heat rejection of 7.51 W for a safety factor of 1.5 and a turndown of 12.7 with a heat rejection of 9.63 W for a safety factor of 1.

Next, a separate plot was made to demonstrate the diminishing returns in turndown after exceeding an open angle of 180°. Figure 35 below shows an asymptotic behavior of the turndown versus open angle where the data sets begin this trend at around 180°. This justifies the reasoning behind designing the composite layup to meet the strength requirements for that given level of openness. Additional actuation beyond 180° will improve overall turndown but composite failure stress considerations and fatigue life must be accounted for.
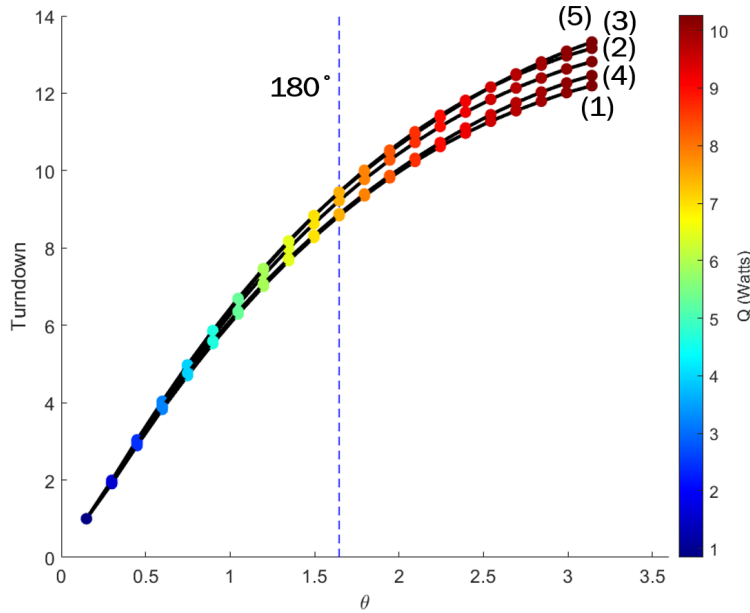
Figure 35: Plot of turndown vs. open angle for circular geometry

This study has informed many different insights outside of the panel geometry and composite selection. Particularly due to the loading application primarily being bending, the stress in the composite is sensitive to layup thickness. Presented here was the results for a nominal composite thickness while Appendix B dives deeper into the worst case composite thickness tolerance based on manufactured panels. This sensitivity is also demonstrated when comparing between different layups within this nominal thickness study. The addition of extra plies showed increased stress factors, hindering turndown performance of the radiator by not allowing it to reach higher open angles before failure. The main contributing factor to this is the ply thickness of each lamina. Given thinner ply layers, the possible resulting composites could allow for symmetric layups typically used in aerospace applications. More specifically, axial-extensional coupling (coming from the B matrix as discussed in Section 2.2) from aymmetric layups can lead to significant warping due to residual stresses arising from mismatches in coefficients of thermal expansion. This effect is eliminated with a symmetric layup which is especially important to mitigate any initial stress state of the composite, negatively effecting its failure strength. Additionally, with

this thermal control systems plans for multiple radiator panels in series, any warping could cause interference between panels in an array. Another important composite behaviour found during this study was the bend-twist coupling behaviour resulting from unbalanced layups. The twisting behaviour caused significant stress concentrations that can be easily seen in the difference in failure stress factor between the [90/45/0/-45/90] and [90/45/0/45/90] layups. A more detailed discussion behind this phenomenon lies in Section 2.2.

Upon manufacturing of the best performing layup ([90/45/0/-45/90]) visible warping was observed. This comes as a results of using an anti-symmetric balanced layup which eliminates the bend-twist coupling yet has potential for initial warping upon retrieval from the autoclave oven. An example of this warping can be seen below in Figure 36. In this same figure, a twinned layup is shown which aims to mitigate this warping by placing two opposite sign 45° ply layers in the same ply plane. Figure 37 below shows how this layup is manufactured from the outside to inside diameters of the morphing radiator from left to right. This solution hinges on a common practice to address this warping in layups by placing opposite sign angle plies one after the other. This mitigates warping effects by negating the coefficient of thermal expansion contributions from each angle ply.

Figure 36: Original balanced layup [90/45/0/-45/90] on left, twinned layup on right
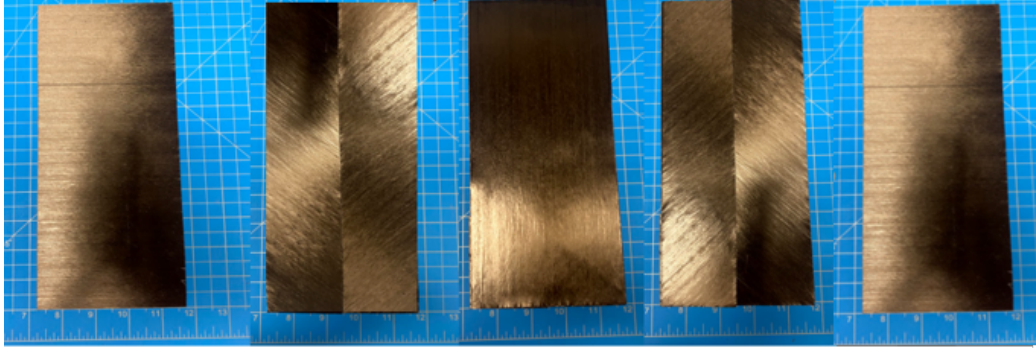
Figure 37: Ply stack orientations for manufacutring, left to right corresponds to bottom to top

Failure stress factor versus turndown results were obtained for this new twinned layup and showed slightly worse performance than the best layup, although this was due to highly localized stress concentrations where the 45° ply layers meet in the middle of the panel. This proved to be no problem in testing as the composite panel was cycled to 180° open hundreds of times without failure. However, this fact must not be neglected as local non-catastrophic damage could be occurring within the laminate affecting overall strength. Further results demonstrating the twinned laminate stress concentrations can be found in Appendix B.

The main restriction with this composite trade study was the chosen carbon fiber prepreg ply thickness. Previous experimental work used a carbon fiber material with similar proprerties and half the ply thickness. Specifically, the current fiber in use for this work is a K13C2U carbon fiber with a 0.005 in ply thickness, while the old carbon fiber was K13D2U with a 0.0025 in ply thickness. Thus, another trade study was conducted to determine the best possible layup given this more desirable ply thickness. A list of the simulated layups can be found below for the K13D2U carbon fiber:

- Layup 1: [90/45/-45/0/45/-45/90]
- Layup 2: [90/45/-45/0/0/45/-45/90]
- Layup 3: [90/0/90/0/90/0/90]
- Layup 4: [90/60/-60/30/-30/0/30/-30/60/-60/90]

61

- Layup 5: [90/60/-60/30/-30/0/0/30/-30/60/-60/90]

- Layup 6: [90/45/-45/45/-45/0/45/-45/45/-45/90]

Figure 38 shows the failure stress factor versus turndown results for these composite laminates.
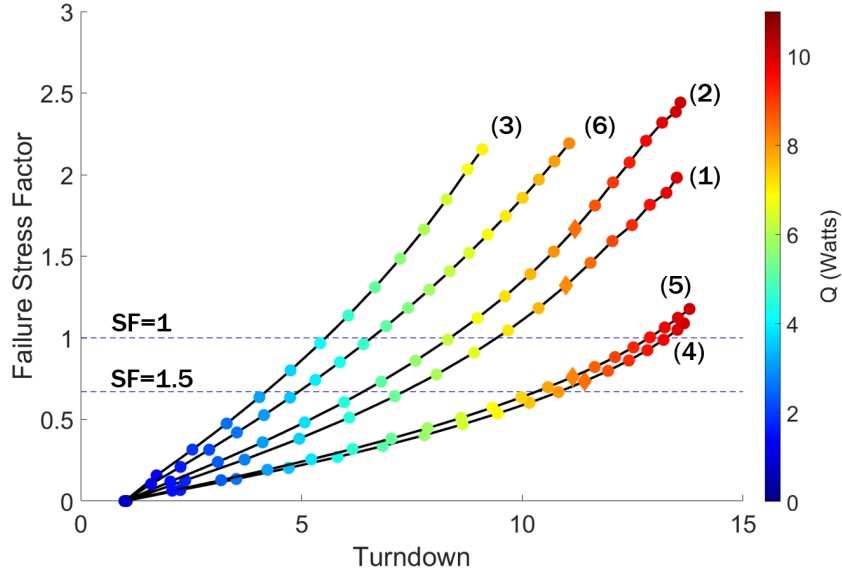
Figure 38: Failure stress factor vs. turndown for laminates using thinner
ply K13D2U carbon fiber (diamond represents 180° open angle)

Taking the best performing laminates for both the K13C2U and K13D2U carbon fibers, Fiugure 39 shows a comparison of their performance with respect to failure stress factor and turndown. The K13D2U based laminate performs the best, although the K13C2U based laminate has slightly higher turndown at the same level of open angle. Interestingly, where the K13D2U based laminate wins out is in the greatly improved failure stress factor with open angle which can be clearly seen in Figure 40. Furthermore, this laminate uses an arbitrary selection of 30° and 60° angle plys and thus further optimzation could be achieved by exploring combinations of angles between 0° and 90°.

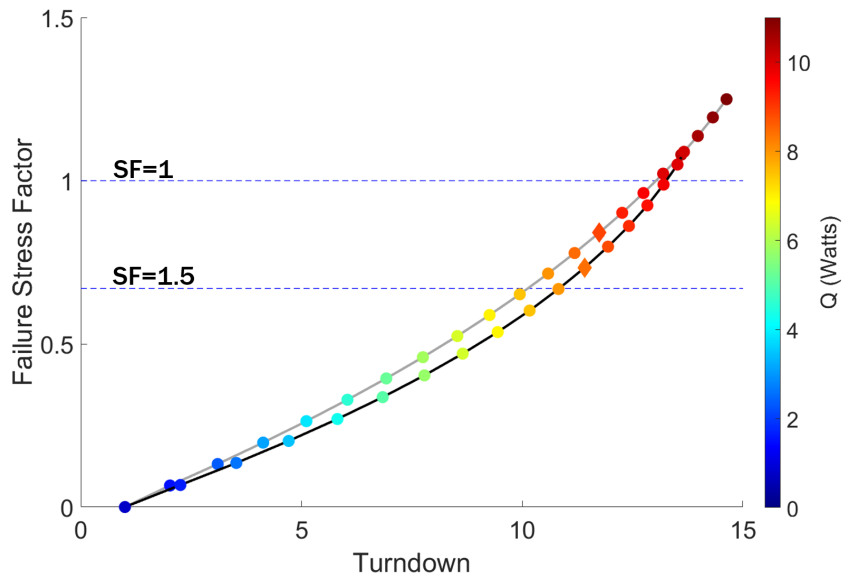Figure 39: Failure stress factor vs. turndown for best performing layups using both carbon fibers (K13C2U in grey [90/45/0/-45/90], and K13D2U in black [90/60/-60/30/-30/0/30/-30/60/-60/90], diamond represents 180° open angle)
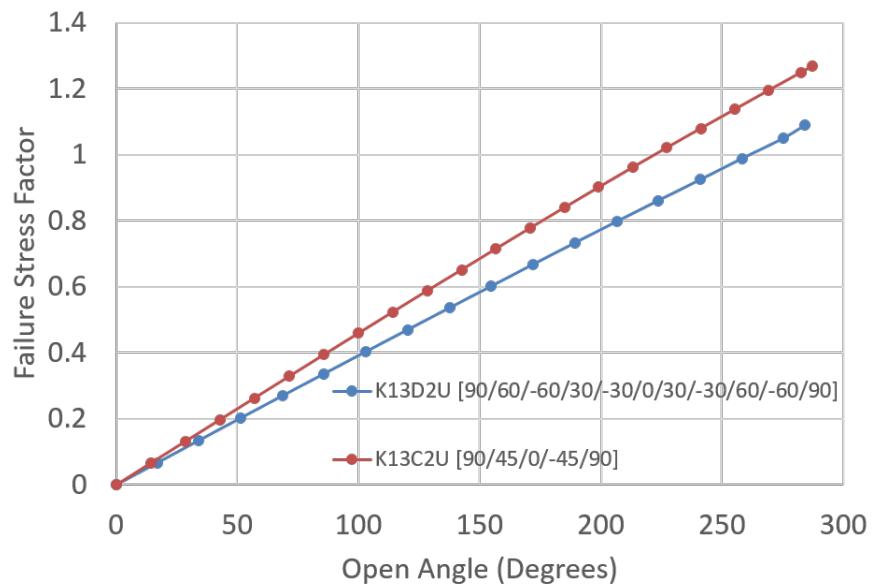

Figure 40: Failure stress factor vs. open angle for best performing layups of both carbon fibers

4.2 Validation of the Fully Thermomechanically Coupled Model

With this morphing radiator model being utilized as a design tool, it is imperative to validate its accuracy to ensure the behaviour of the system is captured. To validate the simulation results of the radiator, a model was developed to match the single panel experimental thermal vacuum chamber test done by Patrick Walgren and NASA JSC [6]. A diagram of this model can be visualized in Figure 41. Careful consideration was made to accurately match every aspect of the experimental conditions. First, the composite properties were a [90/45/-45/0/0/45/-45/90] layup with K13D2U unidirectional carbon fiber and RS-3C resin and a ply thickness of 0.0025 in. The SMA coverage area was 60% of the exterior surface area of the radiator with 0.005 in thick NiTiCo strips. The working fluid, a 50/50 propylene glycol and water mixture, was modeled with a constant flow rate of 550 lbm/hr. The aluminum endcaps were thermally tied to the tube mount with tabs and are slightly oversized as they were during the experiment. Additionally a bondline of Arctic Silver epoxy was modelled based on the average manufacturer specified bondline thickness [46].
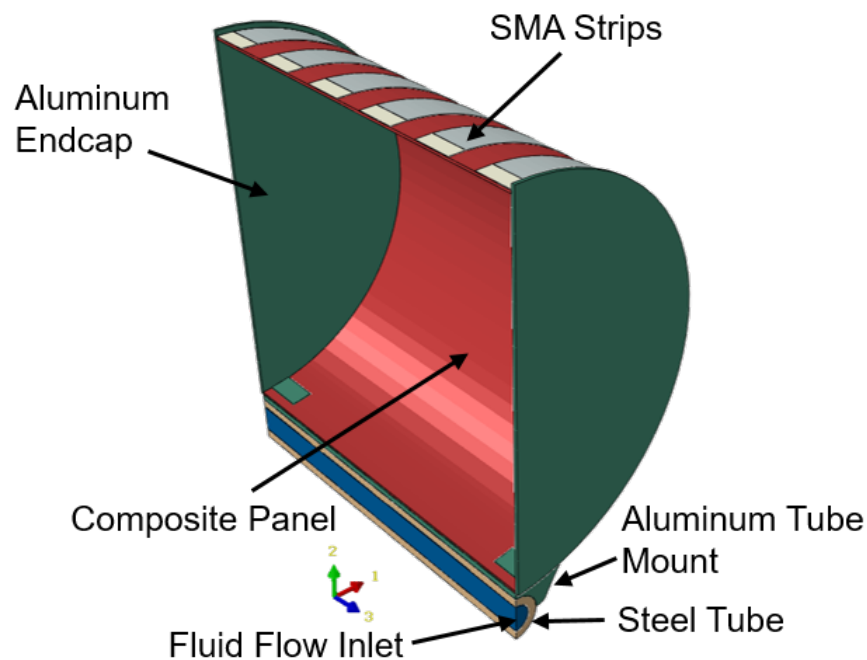

Figure 41: Validation model diagram

The low stress response of the SMA is pertinent to this application since the SMA approaches zero stress as the radiator becomes fully closed. Through an iterative process of calibrating the SMA properties for use in the model, this phenomenon was discovered. Initial calibration methods used an averaging scheme of the properties at different stress levels to fit isobaric test curves. When implementing these averaged properties into the validation model, overclosure of the radiator was observed resulting mainly from poor representation of the SMA response at low stresses. In particular there was a large difference in the martensitic start transformation temperature, M_s, at the 7 MPa curve compared to higher stress curves. Thus, a second method was utilized which incorporates a biasing of the low stress properties, leading to a much more accurate closure angle of the radiator as seen later in Figure 46. The SMA calibration curves in strain-temperature space conducted by Patrick Walgren can be found below in Figure 42 while more detailed parameter and phase diagram details lie in Appendix A.
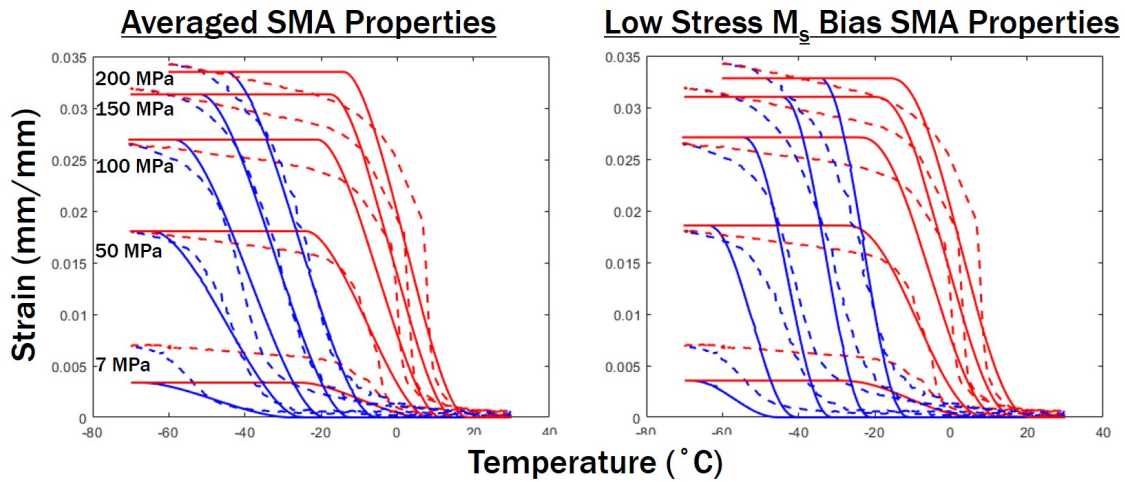
Figure 42: NiTiCo SMA strip experimental (dashed) and calibration (solid) strain-temperature curves

The two key metrics used to measure accuracy between the actuation cycles are the temperature at various locations of the radiator, along with the open angle. The fluid inlet temperature over time from the experiment is used as the input for this analysis with the corresponding outputs being open angle and temperature at the base, middle and top sections of the radiator

down the midline of the length of the radiator, also color coded by red, green and blue in Figure 43, respectively. Additionally, Figure 43 displays all the thermocouple locations in the experiment, of which thermocouples 2, 4 and 7 as well as the fluid inlet PRT measurements were used as the temperature basis for simulation comparison.

Figure 43: Experimental validation thermocouple locations

The fluid inlet temperature is cycled from 50 °C to -45 °C to 50 °C again, with a constant shroud temperature of -177 °C. Tem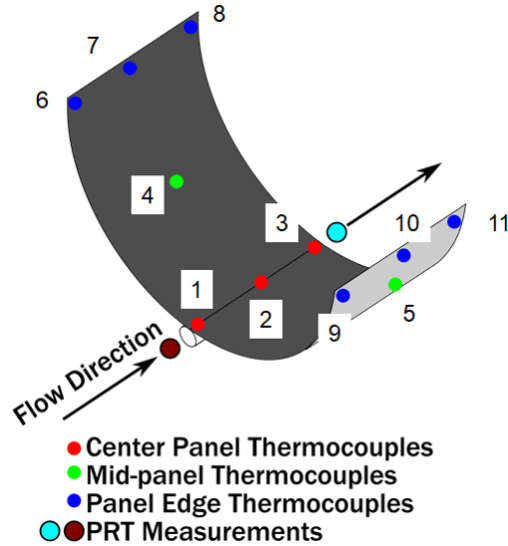perature and open angle results can be visualized in Figure 44 and Figure 46. Trends to note are that the coldest case panel temperatures of the simulation roughly match the minimum bound of the experiment at about -45 °C while the simulation panel temperatures during heating are consistently 4 °C higher than the experiment, besides the base panel temperature which is more closely tied to the fluid temperature. These discrepancies can be attributed to a few major areas. First, the composite thermal conductivity through the thickness is critical for this analysis and was approximated based on manufacturer feedback since it is difficult to measure through testing. From previous analysis work in attempting to address this issue, the temperature of the composite was shown to be sensitive to this property change. Furthermore, the model simplifies the MLI as a constant emissivity surface which could lead to temperature inaccuracies from not capturing this more complicated insulation interaction.

66

Also on the experimental side the surface thermocouples could have had a temperature gradient from radiating heat, dropping their temperature readings further. The largest difference in temperatures between experiment and simulation comes from the base temperature which compounds the middle and tip temperatures. Thus, any additional thermal resistances that were not captured in the model could explain the variance between experiment and simulation thermocouple readings.
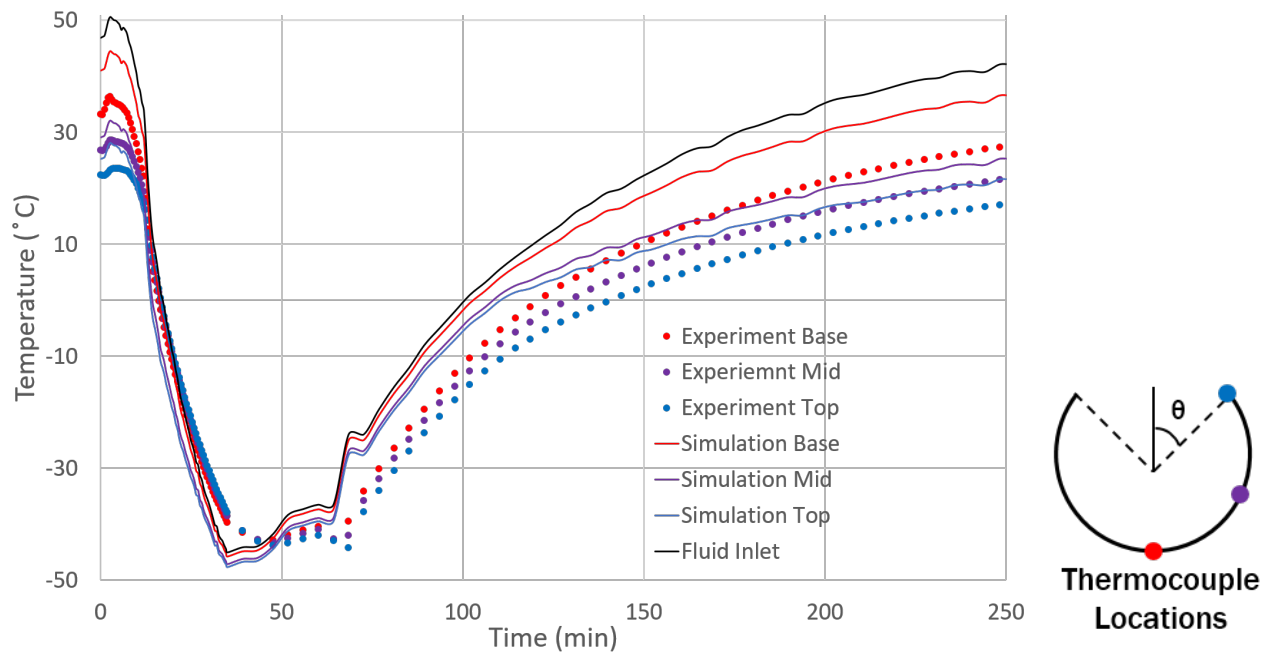
Figure 44: Radiator temperatures vs. time for experiment and simulation

Next, two methods were used to track the open angle of the radiator during the experiment. The first was an optical tracking of the left and right terminal block angles depicted in red in Figure 45. However, this method was prone to slight variations in tracking with data during heating sometimes dipping below others even when the images clearly show the radiator opening to a further degree. Thus, a second method was implemented which tracks the gap distance between the terminal blocks and backs out the angle through arc length equations as seen in purple along with the associated arc length diagram in Figure 45. Given that the arc length of the radiator throughout the experiment is fixed and equal to its circumference and the chord

length is equal to the terminal block gap distance, arc length and chord length equations can then be solved for θ,

$$S = R\theta \tag{4.73}$$

$$d = 2Rsin(\frac{\theta}{2}) \tag{4.74}$$

$$d = 2\frac{S}{\theta}sin(\frac{\theta}{2}) \tag{4.75}$$
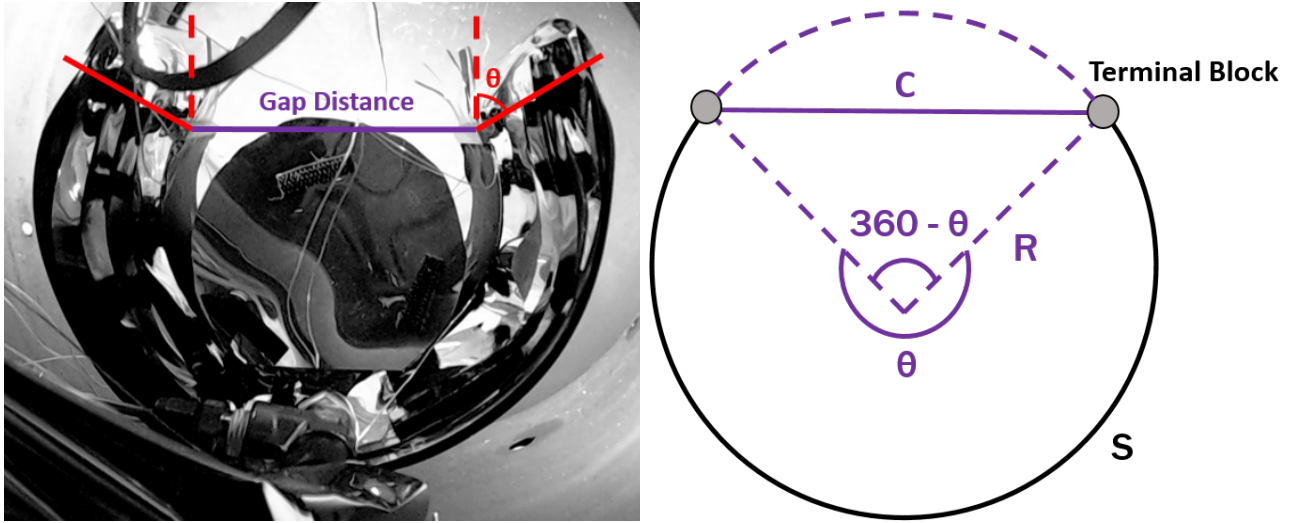
Figure 45: Measurement methods for open angle

Note that this θ corresponds to the exterior angle based on radial lines drawn to the terminal blocks and thus to obtain the open angle of the radiator, this θ is subtracted from 360°.

The resulting open angle comparison between experiment and simulation are illustrated below in Figure 46. The right and left winglet average open angle refers to the optical measurement of the terminal block angles with vertical, while the arc length average refers to the angle backed out from terminal block distance. For both experimental open angle results, error bars are place to signify the measurement uncertainty. The low stress biased SMA properties indicated a close modeling to experimental behaviour of the morphing radiator. In particular, nominally the simulation closed configuration had an error of 19% while the open configuration nearly matched

the experiment at an error of 1.2%.

Figure 46: Radiator open angle vs. time for experiment and simulation
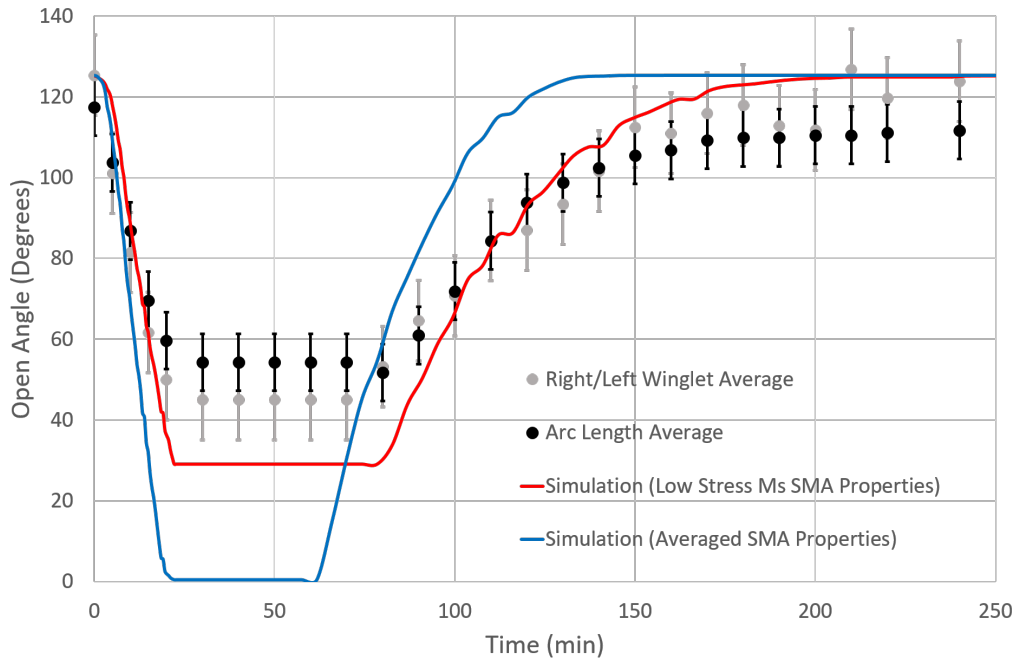with measurement uncertainty considerations

Uncertainty considerations arise in these experimental open angle results because they were manually and optically measured using pictures of the radiator at different time steps throughout the test. The distance accuracy of the optical measurement tool used to track angles was accurate to a hundredth of an inch. Thus, this leads to an inherent error for both measurement methods of 1.72°. The first method of measuring open angle through the terminal block angle with the vertical was sensitive to human error. This is more noticeable at stages of the test where the morphing radiator is near fully open. Particularly, images show increased open angles advancing forward in time but some measurements read drops in open angle due to human error. This shakes down at a worst case to an overshoot error of 8.27°. The arc length measurement method mitigates this source of error by allowing for a much easier measurement of the distance between terminal blocks, resulting in the open angle measurement never reversing direction during heating or cooling phases. However, this arc length measurement method is not perfect

as it uses a calibration factor based on the real dimension of the terminal block and the length of the lines used to measure distance in the optical tool. This leads to a potential error in open angle of 5.37° based on this calibration and the measurement accuracy of the optical tool. In total, the errors for both methods amount to 9.98° and 7.08° for the right/left winglet average and arc length average data in Figure 46, respectively.

To visualize the state of radiator at the two thermal bounds, Figure 47 below shows temperature contour plots of the heated and cooled configurations for the radiator validation model.
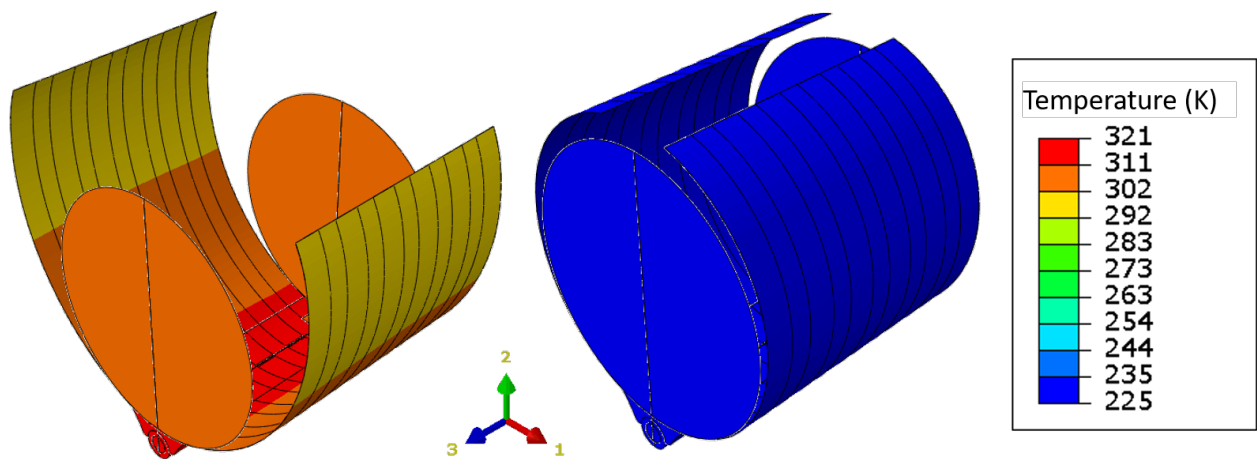
Figure 47: Validation temperature contour plots, heated geometry on left, cooled geometry on right

Validation of a finite element model requires careful consideration for all aspects involved. Often times assumptions are made that may simplify key behaviours of the physical reality. This validation process was highly iterative, to ensure model accuracy and avoid oversimplifications that existed. For this reason, many lessons were learned in developing the final morphing radiator model. To start, careful calibration of SMA model parameters are critical to achieve accurate behaviour of the morphing radiator, especially during low stress. Thermal resistance factors like the thermal conductivity of the composite through the thickness, and bond layer thickness both contributed greatly to improving panel temperature accuracy. Furthermore, composite nodal temperatures are tracked by section points throughout each ply, which defaults at three. In

ensuring the correct surface temperatures of the panel were recorded, it was found that large temperature variation ($\sim 4°C$) exist between top and bottom layers of the composite. Steady state heat transfer analyses proved more accurate to experimental temperatures while transient lagged behind considerably. Overall error between simulation and experiment still remains with the final model in both temperature and open angle results. This error was deemed sufficient to use this model as a design tool but also demonstrates the sensitivity of this technology to SMA model parameters.

4.3 Design of Experiments

Next, a design of experiments was conducted to determine effects of some key inputs, particularly with respect to the SMA wires. These inputs include the number of wires, the martensitic start transformation temperature, and the delta between the martensitic start and finish temperatures. The wire diameter was held constant at a diameter of 0.030 in. The reasoning behind these inputs is that both experimental and modeling experiences has shown difficulty in fully closing the radiator for the cold case, while it consistently reachs nearly fully open in the hot case. The SMA properties that were utilized for this study came from isobaric tests done on a variety of SMA samples with varying heat treats and composition levels of cobalt. A list of the averaged properties from this data can be found in Appendix A.

First, a diagram of the radiator model used for this analysis is shown below in Figure 66.
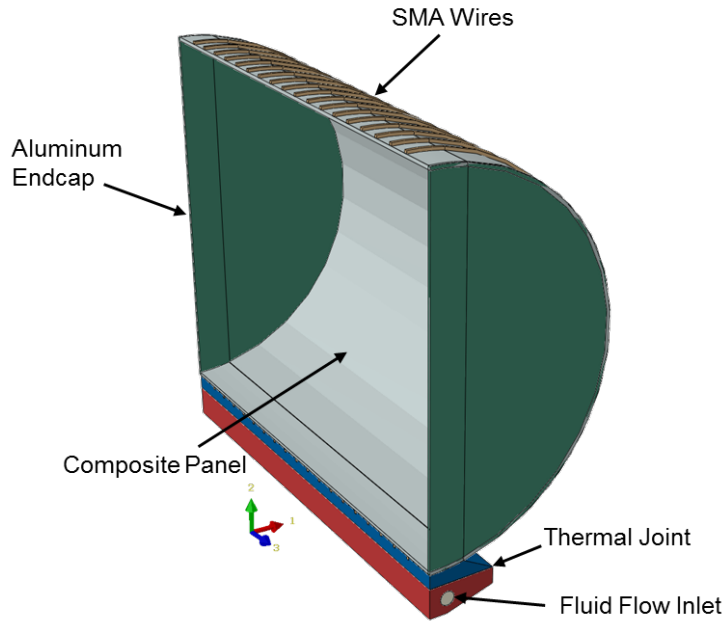
Figure 48: DOE radiator diagram

Next, the list below shows the design variables for the DOE and their various levels. A Taguchi L9 was used for this which lowers the amount of required runs versus a full factorial method while still giving sufficient results to extract relevant effects of each design variable on the outputs.

- Design Variable [Level]

  - Number of wires [15, 18, 21]

  - M_s [-12°C, -9°C, -6°C]

  - $\Delta M = M_s - M_f$ [25°C, 30°C, 35°C]

As mentioned previously, closure is the main focus of this DOE thus the design variables were centered on the martensitic transformation temperatures to achieve as much closure as possible. Additionally, the number of wires was selected to drop the maximum stress in the wire at fully open as much as possible to improve fatigue life. The corresponding outputs for this DOE are listed below:

- Outputs

  - SMA wire average σ_{mises} @ θ=180°

  - θ_{max} @ T_{inlet} = 30°C

  - θ_{min} @ T_{inlet} = -20°C

By tracking these outputs, some trends were ascertained for each of the design variables through creating main effects plots displayed below in Figure 49. First, the stress in each wire drops with increased number of wires which is important to note from a design perspective, as this change in stress affects the transformation temperatures of the SMA. Next, the fully closed angle greatly decreases with the increase in M_s and decrease in hysterisis ΔM. The fully closed angle is critical to this application through achieving a low heat rejection in the cold case, thus these martensitic transformation temperature properties should be adjusted based on these trends to a feasible range.
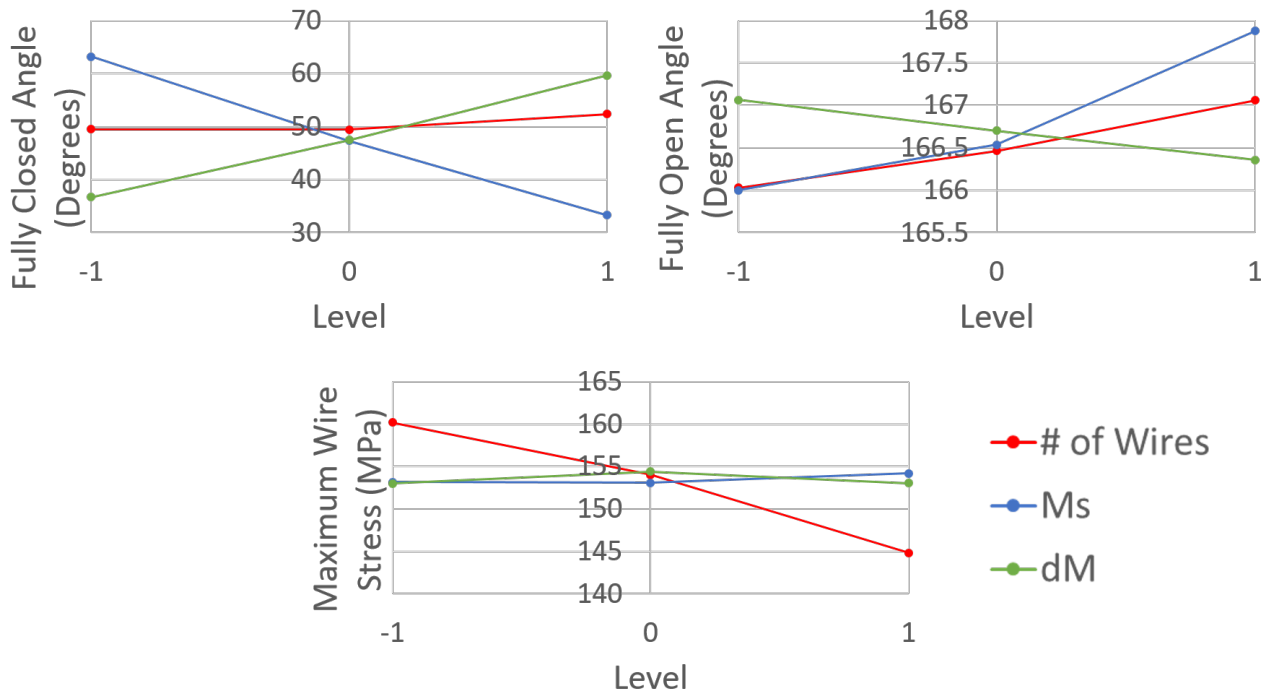
Figure 49: Main effects plots for all design variables

Additionally by plotting the fully closed angle versus the fully open angle, properties resulting in the best performance were found as shown below in Figure 50. The best case and worst case of fully closed angle is also displayed in Figure 51.

Figure 50: Fully closed angle vs. fully open angle for all DOE runs

Figure 51: DOE fully closed angles, worst case on left, best case on right

Lastly, to view feasibility of the SMA properties used in this study we compared the simulation ΔM and M_s to the experimental isobaric tests done by NASA GRC and Othmane Benefan. To ensure comparability to the zero stress properties of the DOE, Figure 52 displays this for

only the low stress experimental data (around 3 MPa). The DOE data is in the middle of all the experimental results, but the experimental SMA sam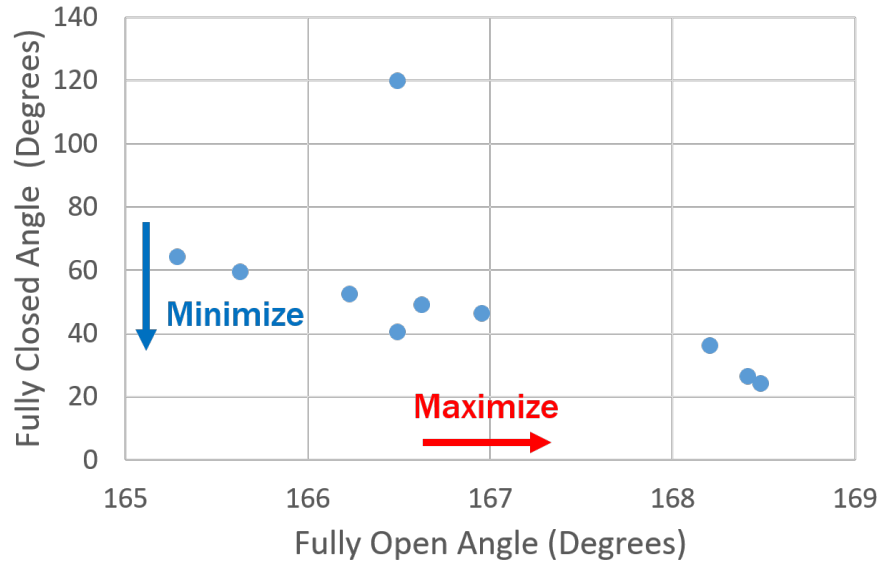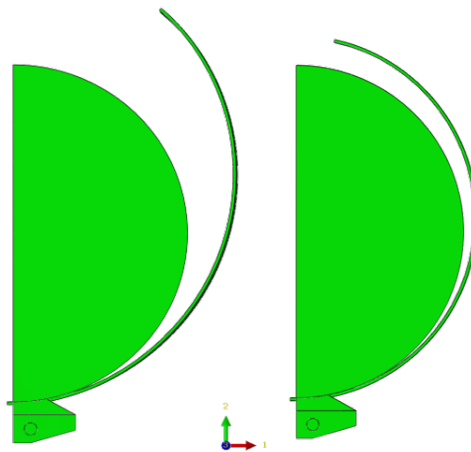ples were untrained and thus could possibly easily shift to a desired temperature range. So although no current material matches the desired properties, we have a better conceptual idea of where we want to end up. The best performing properties are an M_s of 6°C and a ΔM of 25°C with 18 wires, but full closure was still not seen, so a higher M_s and lower ΔM would be desirable. All of this data is pending on some sample SMA wire sent from NASA GRC, that is to be trained and tested at Texas A&M to compare to this study in the future.
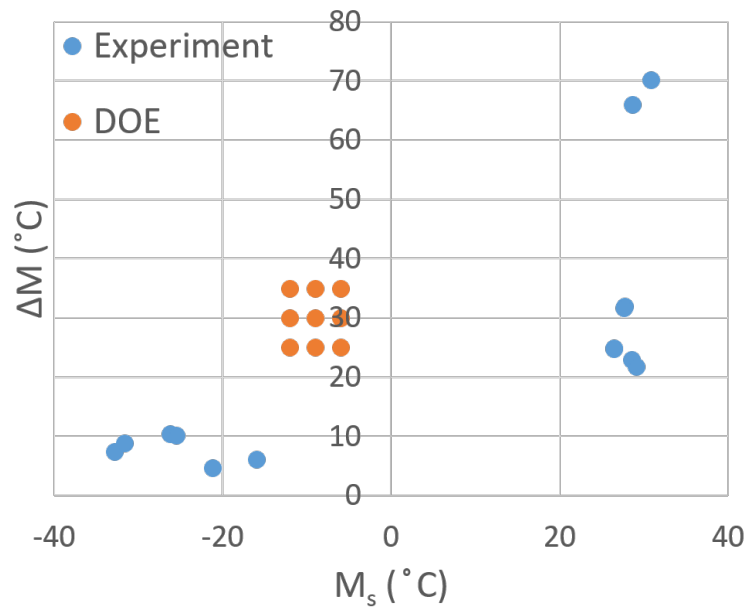
Figure 52: Comparison of M vs. Ms for DOE and experiment

Using the best run from this DOE, some other important outputs were extracted to visualize more about the thermal performance, composite behaviour and SMA response. First, a plot of the open angle versus temperature can be found below in Figure 53 to demonstrate the performance of the best parameters from the DOE. The minimum closed angle was 24° while the maximum open angle upon reheating was 171°. The designated minimum closed angle will be further aided by terminal blocks on the ends of the composite, while the specified maximum open angle prescribes the open angle upon reheating as the model starts at 180°. Additionally, as

mentioned previously the SMA properties are preliminary and untrained, meaning with further iterations the closed and open performance can be improved.
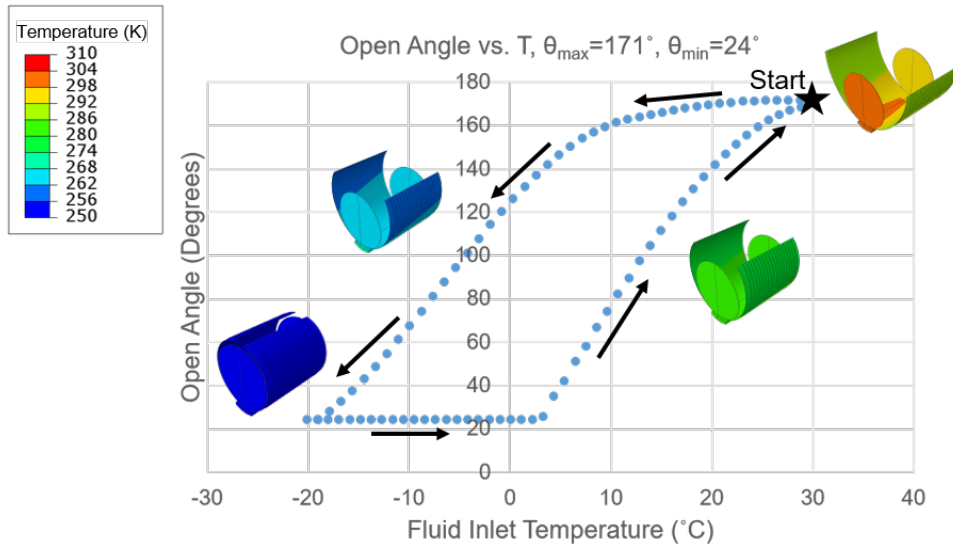
Figure 53: Open angle vs. temperature for SMA-driven operational cycle of the radiator

Next, the temperature gradient of the fluid down the length of the radiator can be visualized at various levels of open angle in Figure 54. This temperature drop is yet another way to conceptualize the heat rejection performed by the panel, as the temperature change increases with open angle, maximizing at the point where the radiator is in full view of space. Another way to visibly see this is through Figure 55 which shows the temperature drop of the fluid down the length of the radiator plotted directly against open angle.
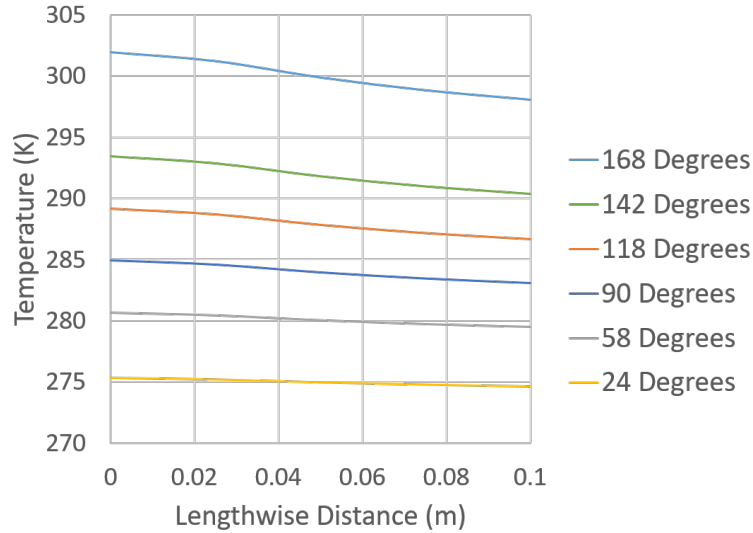
Figure 54: Fluid temperature gradient down the length of the radiator for varying open angles
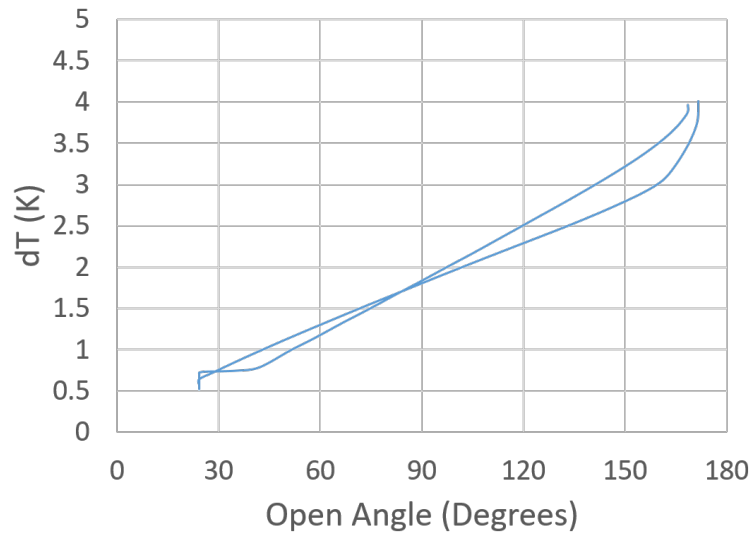
Figure 55: Lengthwise fluid temperature drop vs. open angle

In terms of composite behaviour, the maximum stress throughout the laminate is plotted for the corresponding in plane principal directions. Through Figure 56, notice the σ_{22} tension and σ_{11} compression are the closest to their failure stresses, with the former being the critical stress in the fully open case. Additionally, Figure 57 shows the σ_{11} stress throughout each ply of the composite for a representative element in the center of the panel. Given a normal pure bending problem, the tension and compression would be of a similar magnitude, however, the graphic

77

illustrates a dominated compressive stress. This is due to the additional load of the wires flush against the panel pulling it open. If the moment arm from the panel to the wires was increased, this variation would begin to equilibrate.
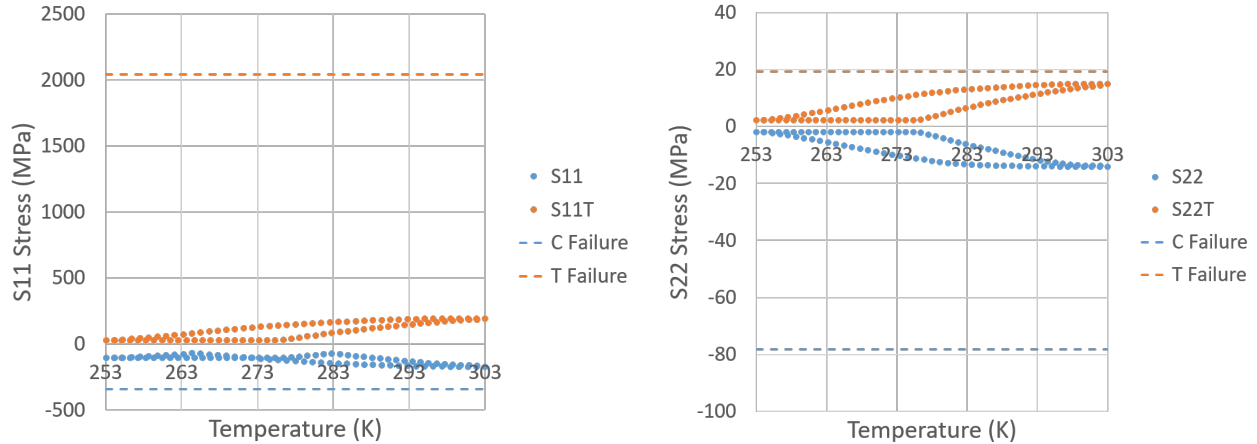
Figure 56: Composite laminate maximum stress vs. temperature, σ_{11} on left and σ_{22} on right
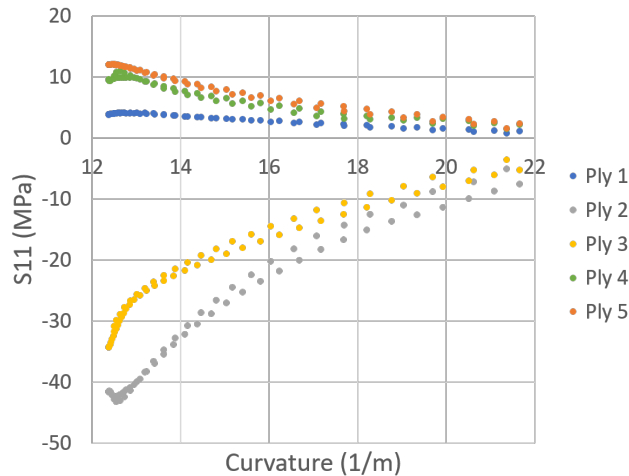
Figure 57: Composite ply by ply σ_{11} stress state vs. curvature at center of panel

The SMA response is best seen by comparing the stress-temperature response of a thermal cycle of the radiator against the SMA phase diagram. Figure 58 below shows the start of martensitic transformation to align with the M_s line at stress. Furthermore, the start of austenitic transformation begins partway through the A_s and A_f lines due to the state of the SMA being in partial and not full martensite. This partial transformation also indicates that

78

the SMA need not fully transform into martensite to completely close the radiator, widening the design space for the SMA.
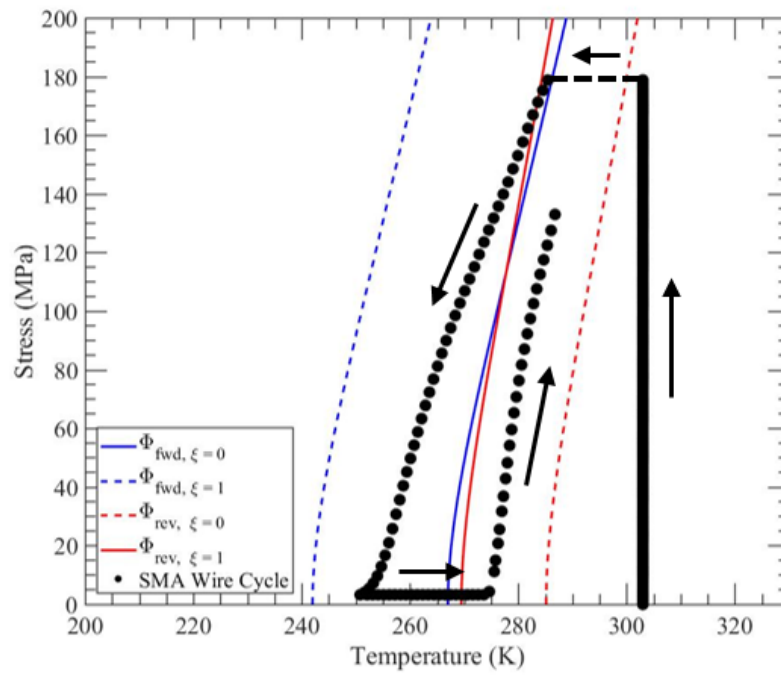
Figure 58: SMA response for a operational cycle of the radiator

5. CONCLUSION & FUTURE WORK

Regulating a space crew cabin's temperature is of utmost importance, with future manned space missions encountering more diverse temperature extremes. Intuitive radiator designs are called to counteract these temperature variations, with requirements on turndown ratios of 6:1 and 12:1. This research demonstrates that a unique SMA-driven morphing radiator is capable of accomplishing these goals within reasonable temperature ranges for a thermal control system. Previous experimental work achieved these turndown ratios through large temperature cycles, however this research aims on tightening this temperature range to a feasible level while still maintaining a full open and closing cycle. Moreover, a fully developed thermal-mechanical model of the radiator was used as a design tool to achieve this end. The work presented here delves into a variety of design topics including model validation, geometric considerations, composite layup optimization, and desired SMA wire properties. Ultimately these efforts proved the present SMA morphing radiator concept as fully operational and advanced the technology readiness level forward.

To validate the morphing radiator model for use as a design tool, a detailed model was created to match the thermal vacuum chamber testing. Final results showed a close correlation of the open angle between model and experiment, nominally having a 19% error in the closed configuration and a near matching in the open configuration at an error of 1.2%. This study indicated the importance of capturing the SMA response in the low stress state, especially for this variable stress application. As without capturing the low stress behaviour, the model fully closed the panel. Simulation thermal results also show approximately a 4°C warmer middle and tip panel temperatures than experiment while the base panel temperature is at a 10°C difference. These thermal discrepancies were found to be negligible as the open angle results ensure the model is accurate in its use for further design considerations.

A turndown study was conducted to determine the optimal composite layup that provides the most turndown within structural bounds. It was found that a layup of [90/-45/0/45/90]

performed the best, achieving a maximum turndown of 12.8, and a turndown of 9.94 given a conservative safety factor of 1.5. The main factor contributing to these results was a fixed ply thickness from the chosen fiber. Given thinner plies, ideally the layup would remain balanced with an equal number of opposite sign 45° plies. Furthermore, this study highlighted the necessity to balance each 45° ply with an opposite sign counterpart to avoid nonzero twisting terms in the composite bending stiffness D matrix. This twisting behaviour caused unwanted high stress concentrations leading to poorer open angle and subsequent turndown performance.

Key SMA wire properties were drawn from a design of experiments that aimed at minimizing the fully closed angle of the radiator. With SMA modeling parameters informed by preliminary NiTiCo wire data, the best performing properties consisted of an M_s of -6°C, ΔM of 25°C, and 18 wires. The minimum closed angle achieved was 24° and the maximum open angle upon reheating was 171°. Turndown results of this case reach the target turndown of 6:1 at 7.7 while this number will greatly increase with the further closure of the radiator in the cold case. Other key takeaways from this study are that only partial transformation is required for full closure, allowing for more margin and a broader design space for the SMA hysteresis.

Many areas of improvement remain with this design process and development of the morphing radiator technology. In terms of design optimization, a full surrogate-based optimization approach could benefit this expensive black box problem greatly to further explore the design space of SMA properties and wire number or sizing. Along the same line of thinking, the dimensionality of the design of experiments could be increased to investigate the austenitic transformation temperatures to ensure full opening of the radiator in the hot case. Looking towards future modeling efforts, an array of morphing radiators would be of interest as this is the true intention of the application. Modeling an array would capture the thermal effects between panels and adjacent components, as well as provide a means to simulate various temperature conditions for the entire thermal control system. Similarly, incorporating the thermal joint technology that interfaces with the morphing radiator into the model can help simulate full

operational performance of the radiator thermal control system. This capability would allow separation of the fluid channel from the morphing radiator at extreme temperatures. Additionally, gap conductance can be implemented based on experimental pressure and clearance data for both the thermal joint and composite panel to best capture the thermal resistance stack up. Many other aspects of the model were simplified for this work, in particular the terminal blocks and MLI blanket. For further accuracy of the model these could be modeled or separate trade studies on their local effects should be investigated. As a single panel representation, the current work has highlighted the ability to achieve target turndowns and proven the ability to operate within a realistic temperature range for a space crew cabin thermal control system.

6. REFERENCES

[1] Reysa, R., and Thurman, R. "The International Space Station ECLS and thermal control systems - Overview." in *Sixth European Symposium on Space Environmental Control Systems* (T.-D. Guyenne, ed.), vol. 400 of *ESA Special Publication*, p. 11, Aug. 1997.

[2] Bertagne, C. L., Cognata, T. J., Sheth, R. B., Dinsmore, C. E., and Hartl, D. J. "Testing and analysis of a morphing radiator concept for thermal control of crewed space vehicles." *Applied Thermal Engineering*, vol. 124, pp. 986–1002, 2017.

[3] Bertagne, C., Walgren, P., Erickson, L., Sheth, R., Whitcomb, J., and Hartl, D. J. "Coupled Behavior of Shape Memory Alloy-Based Morphing Spacecraft Radiators: Experimental Assessment and Analysis." *Smart Materials and Structures*, Apr. 2018.

[4] Lagoudas, D. C., Entchev, P. B., and Kumar, P. K. "Thermomechanical characterization of SMA actuators under cyclic loading." *ASME International Mechanical Engineering Congress and Exposition.* vol. 37076, 2003.

[5] Walgren, P., Bertagne, C., Wescott, M., Benafan, O., Erickson, L., Whitcomb, J., and Hartl, D. "Development and Testing of a Shape Memory Alloy-Driven Composite Morphing Radiator." *Shape Memory and Superelasticity*, pp. 1–10, Jan. 2018.

[6] Walgren, Patrick. "Towards High-Turndown-Ratio Shape Memory Alloy Driven Morphing Space Radiators: Manufacturing Methods, Computational Modeling and Prototype Demonstration." Texas A&M University, Thesis, 2019.

[7] Bertagne, C., Cognata, T., and Hartl, D. "Analysis of Highly Coupled Thermal-Structural Responses in Morphing Radiative Bodies." *AIAA SciTech Forum*, pp. 1–14, Jan. 2015.

[8] "Toray Advnaced Composites – K13C2U / RS-3/3C." Tech. rep., *Toray Advanced Composites*, 2020.

[9] "Toray RS-3 Cyanate Ester." Tech. rep., *Toray Advanced Composites*, 2019.

[10] Leimkuehler, T. and Lantz, G. "Single Loop Thermal Control for Deep Space Exploration." in *42nd International Conference on Environmental Systems*, (San Diego, California), American Institute of Aeronautics and Astronautics, July 2012.

[11] Stephan, R. "Overview of NASA's thermal control system development for exploration project." in *40th International Conference on Environmental Systems*, 2010.

[12] Demiryont, H. and Moorehead, D. "Electrochromic emissivity modulator for spacecraft thermal management." *Solar Energy Materials and Solar Cells*, vol. 93, no. 12, pp. 2075–2078, 2009.

[13] Ganapathi, G. B., Sunada, E. T., Birur, G. C., Miller, J. R., and Stephan, R. "Design Description and Initial Characterization Testing of an Active Heat Rejection Radiator with Digital Turndown Capability." *SAE International Journal of Aerospace*, vol. 4, pp. 272–278, July 2009.

[14] Nagano, H., Nagasaka, Y., and Ohnishi, A. "Simple Deployable Radiator with Autonomous Thermal Control Function." *Journal of Thermophysics and Heat Transfer*, vol. 20, pp. 856–864, Oct. 2006.

[15] Lillibridge, S., Navaroo, M., Cognata, T., and Guinn, J. "Freezable Radiator Testing." in *40th International Conference on Environmental Systems*, (Barcelona, Spain), American Institute of Aeronautics and Astronautics, July 2010.

[16] Bannon, E., Iacomini, C., Bower, C., and Linrud, C. "Stagnating Radiator Thermal Model Design and Verification." in *10th AIAA/ASME Joint Thermophysics and Heat Transfer Conference*, American Institute of Aeronautics and Astronautics, 2010.

[17] Mulford, R. B., Jones, M. R., and Iverson, B. D. "Dynamic Control of Radiative Surface Properties with Origami-Inspired Design." p. 10, 2015.

[18] Athanasopoulos N., and Siakavellas, N. "Variable emissivity through multilayer patterned surfaces for passive thermal control: preliminary thermal design of a nano-satellite." July 2018.

[19] Hendaoui, A., Émond, N., Chaker, M., and Haddad, É. "Highly tunable-emittance radiator based on semiconductor-metal transition of VO2 thin films." *Applied Physics Letters*, vol. 102, Feb. 2013.

[20] Cognata, T., Hartl, D., Sheth, R., and Dinsmore, C. "A Morphing Radiator for High-Turndown Thermal Control of Crewed Space Exploration Vehicles." in *Proceedings of 23rd AIAA/AHS Adaptive Structures Conference*, (Kissimmee, FL), 2015.

[21] Hartl, D. J., Mooney, J. T., Lagoudas, D. C., Calkins, F. T., and Mabe, J. H. "Use of a Ni60Ti shape memory alloy for active jet engine chevron application: II. Experimentally validated numerical analysis," *Smart Materials and Structures*, vol. 19, Dec. 2009.

[22] Carpenter, B., and Lyons, J. "Lightweight Flexible Solar Array Validation Report." *EO-1 First, NASA mission, validation report*, 2002.

[23] Calkins, F. T., and Mabe, J. H. "Flight Test of a Shape Memory Alloy Actuated Adaptive Trailing Edge Flap." in *Volume 1: Multifunctional Materials; Mechanics and Behavior of Active Materials; Integrated System Design and Implementation; Structural Health Monitoring*, (Stowe, Vermont, USA), ASME, Sept. 2016.

[24] Lee, S. H., Mudawar, I., and Hasan, M. M. "Thermal analysis of hybrid single-phase, twophase and heat pump thermal control system (TCS) for future spacecraft." *Applied Thermal Engineering*, vol. 100, pp. 190–214, May 2016.

[25] Assael, M. J., Charitidou, E., Avgoustiniatos, S., Wakeham, W. A., "Absolute Measurements of the Thermal Conductivity of Mixtures of Alkene-Glycols with Water." *International Journal of Thermophysics*, vol. 10, Nov. 1989.

[26] "Online Materials Information Resource." MatWeb, 1996, www.matweb.com/.

[27] Robert M. Jones, *Mechanics of Composite Materials 2nd Edition*. Taylor & Francis, 1999.

[28] Lester, B., Baxevanis, T., Chemisky, Y., Lagoudas, D. "Review and Perspectives: Shape Memory Alloy Composite Systems." *Acta Mechanica*, p. 60, 2015.

[29] "NASA Technology Roadmaps, TA 14: Thermal Management Systems." July 2015.

[30] Ciampa, F. et. al, "Shape memory alloy tufted composites combining high delamination resistant and crack closure properties." *Composites Part A: Applied Science and Manufacturing*, vol. 147, Aug. 2021.

[31] Mirsayar, M. M., Hartl, D. J. "Damage detection via embedded sensory particles – Effect of particle/matrix interphase properties." *Composite Structures*, vol. 232, 2020.

[32] Kirkby, E. L., et al. "Performance of self-healing epoxy with microencapsulated healing agent and shape memory alloy wires." *Polymer*, vol. 50, pp. 5533-5538, 2009.

[33] Raghavan, J., et al. "Damping, tensile, and impact properties of superelastic shape memory alloy (SMA) fiber-reinforced polymer composites." *Composites Part B: Engineering*, vol. 41, pp. 214-222, 2010.

[34] Chang, S. H., and Lee, C. Y. "Damping characteristics of TiNi shape memory alloy wires reinforced epoxy resin." *Journal of Reinforced Plastics and Composites*, vol. 30, pp. 1931-1938, 2011.

[35] Zhang, R. X., et al. "Mechanical properties of composites filled with SMA particles and short fibers." *Composite Structures*, vol. 79, pp. 90-96, 2007.

[36] Ni, Q. Q., et al. "Stiffness and vibration characteristics of SMA/ER3 composites with shape memory alloy short fibers." *Composite Structures*, vol. 79, pp. 501-507, 2007.

[37] Ko, P. L., et al. "Dynamically programmable surface micro-wrinkles on PDMS-SMA composite." *Smart Materials and Structures*, vol. 23, 2014.

[38] Tobushi, H., et al. "Three-way actuation of shape memory composite." *Archives of Mechanics*, vol. 63, pp. 443-457, 2011.

[39] Angioni, S. L., Michele Meo, and A. Foreman. "Impact damage resistance and damage suppression properties of shape memory alloys in hybrid composites—a review." *Smart Materials and Structures*, vol. 20, 2010.

[40] Pappadà, S., et al. "Low-velocity impact response in composite plates embedding shape memory alloy wires." *Polymer Composites*, vol. 33, pp. 655-664, 2012.

[41] Pappadà, S., et al. "Embedding of superelastic SMA wires into composite structures: evaluation of impact properties." *Journal of Materials Engineering and Performance*, vol. 18, pp. 522-530, 2009.

[42] Meo, M., et al. "Shape memory alloy hybrid composites for improved impact properties for aeronautical applications." *Composite Structures*, vol. 95, pp. 756-766, 2013.

[43] Kang, K. W., and Kim, J. K. "Effect of shape memory alloy on impact damage behavior and residual properties of glass/epoxy laminates under low temperature." *Composite Structures*, vol. 88, pp. 455-460, 2009.

[44] Paine, J., and C. Rogers. "High velocity impact response of composites with surface bonded nitinol-SMA hybrid layers." in *36th Structures, Structural Dynamics and Materials Conference.* 1995.

[45] Khalili, S. M. R., M. Shiravi, and A. S. Nooramin. "Mechanical behavior of notched plate repaired with polymer composite and smart patches-experimental study." *Journal of reinforced plastics and composites*, vol. 29, pp. 3021-3037, 2010.

[46] "Arctic Silver Thermal Adhesive Instructions", Arctic Silver Inc., 2012, www.arcticsilver.com/instructions.htm.

[47] Diebold, J., Tarau, C., Lutz, A., Rokkam, S. "Development of Variable-View-Factor and Deployable TwoPhase Radiator." in *International Conference on Environmental Systems*, Advanced Cooling Technologies, Inc., 2020.

[48] D. Gilmore, *Spacecraft Thermal Control Handbook, Volume I: Fundamental Technologies.* Washington, DC: American Institute of Aeronautics and Astronautics, Inc., Dec. 2002.

[49] Qidwai, M. A., and Lagoudas, D. C. "Numerical implementation of a shape memory alloy thermomechanical constitutive model using return mapping algorithms." *International Journal*

87

for *Numerical Methods in Engineering*, vol. 47, pp. 1123-1168, 2000.

[50] Ortiz, M., and Simo, J. C. "An analysis of a new class of integration algorithms for elasto-plastic constitutive relations." *International Journal for Numerical Methods in Engineering*, vol. 23, pp. 353-366, 1986.

[51] Qidwai, M. A., and Lagoudas, D. C. "On thermomechanics and transformation surfaces of polycrystalline NiTi shape memory alloy material." *International Journal of Plasticity*, vol. 16, pp. 1309-1343, 2000.

[52] Simo, J. C., and Hughes, T. J. *Computational inelasticity.* vol. 7. Springer Science & Business Media, 2006.

[53] Boyd, J. G., and Lagoudas, D. C. "A thermodynamical constitutive model for shape memory materials. Part I. The monolithic shape memory alloy." *International Journal of Plasticity*, vol. 12, pp. 805-842, 1996.

[54] Lagoudas, D. C., Bo, Z., and Qidwai, M. A. "A unified thermodynamic constitutive model for SMA and finite element analysis of active metal matrix composites." *Mechanics of Composite Materials and Structures*, vol. 3, pp. 153-179 1996.

[55] Mollica, F., Rajagopal, K. R., Srinivasa, A. R. "The inelastic behavior of metals subject to loading reversal" *International Journal of Plasticity*, vol. 17, pp. 1119–1146, 2011.

[56] Boyd, J. G., and Lagoudas, D. C. "Thermomechanical response of shape memory composites," *Smart Structures and Intelligent Systems*, vol. 1917, 1993.

[57] Lagoudas, D., Hartl, D., Chemisky, Y., Machado, L., Popov, P. "Constitutive model for the numerical analysis of phase transformation in polycrystalline shape memory alloys." *International Journal of Plasticity*, vol.32 pp. 155–183, 2012.

[58] Coleman, B. D. "Thermodynamics of materials with memory." *Archive for Rational Mechanics and Analysis*, vol. 17, pp. 1-46, 1964.

[59] Coleman, B. D., and Gurtin., M. E. "Thermodynamics with internal state variables." *The Journal of Chemical Physics*, vol. 47, pp. 597-613, 1967.

[60] Coleman, B. D., and Noll, W. "Material symmetry and thermostatic inequalities in finite elastic deformations." *Archive for Rational Mechanics and Analysis*, vol. 15, pp. 87-111, 1964.

[61] Coleman, B. D., Noll, W., "The thermodynamics of elastic materials with heat conduction and viscosity." *Archive for Rational Mechanics and Analysis*, vol. 13, pp. 167–178, 1963.

[62] Lagoudas, D. C., ed. *Shape memory alloys: modeling and engineering applications.* Springer Science & Business Media, 2008.

[63] Paglietti, A. "The mathematical formulation of the local form of the second principle of thermodynamics." *Annales de l'IHP Physique théorique*, vol. 27, no. 2, pp. 207-219, 1977.

[64] Schön, J. "Coefficient of friction for aluminum in contact with a carbon fiber epoxy composite." *Tribology International*, vol. 37, pp. 395-404, 2004.

[65] Bertagne, Chris. "Experimental Evaluation of an Analysis Framework for Simulating the Coupled Behavior of Shape Memory Alloy-Based Morphing Radiators." Texas A&M University, Thesis, 2016.

[66] Holman, J. P. *Heat Transfer.* McGraw-Hill, 1990.

[67] Siegel, R., and J. R. Howell. *Thermal Radiation Heat Transfer.* McGraw Hill, New York, 1980.

[68] Hibbitt, D., Karlsson, B., and Sorensen, P. "ABAQUS Version 6.6 Standard user's guide and theoretical manual." *HKS Inc.*, 2006.

[69]Howell, J. R. *A Catalog of Radiation Configuration Factors.* McGraw Hill, New York, 1982.

[70] Hoff, S. J., and Janni, K. A. "Monte Carlo technique for the determination of thermal radiation shape factors." *Transactions of the ASAE*, vol. 32, pp. 1023-1028, 1989.

[71] Dévai, F. "Scan-Line Methods for Parallel Rendering." *High Performance Computing for Computer Graphics and Visualisation*, Springer, London, 1996.

7. APPENDIX A: SMA CHARACTERIZATION

This appendix contains the data used for characterizing the SMA constitutive model presented in this work. Characterization was performed for two separate studies, the validation and the design of experiments.

A1. Validation 5 Mil Thick NiTiCo SMA Strip

The following data gives the low stress biased properties for the SMA strips used in the validation study. The model parameters can be found in Table 5 while the phase diagram is shown in Figure 59.

Table 5: 5 Mil NiTiCo SMA strip low stress bias model parameters used in validation

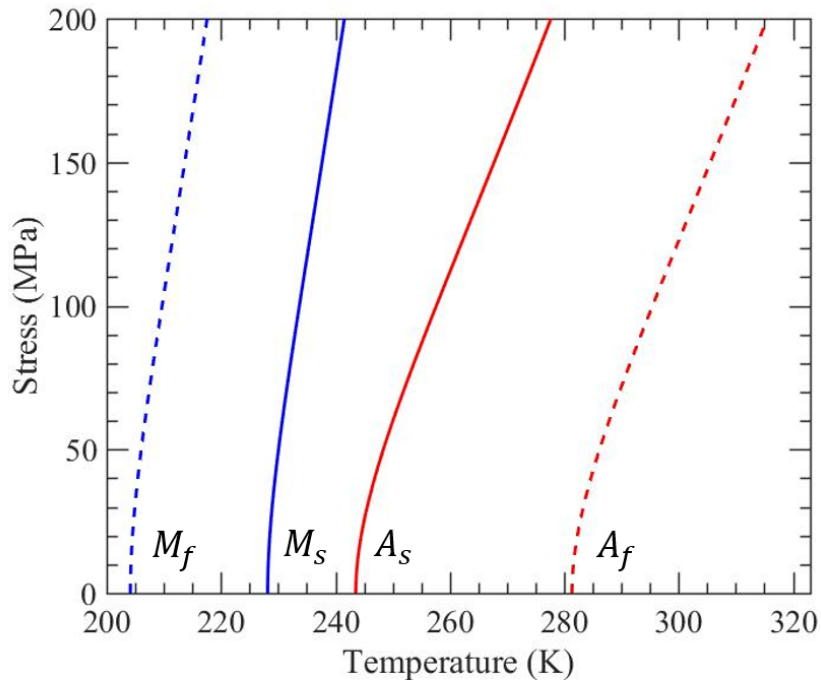| Model Parameter	Calibrated value
E^M	119.0 GPa
E^A	119.0 GPa
ν^M	0.33
ν^A	0.33
α^M	$0 \cdot 10^{-6}$ m/(m·°C)
α^A	$0 \cdot 10^{-6}$ m/(m·°C)
M_f	-69.0 °C
M_s	-45.0 °C
A_s	-29.6 °C
A_f	8.2 °C
C^M	5.11 MPa/°C
C^A	13.0 MPa/°C
H_{min}	0%
H_{max}	3.44%
k	1.55e-8 Pa^{-1}
$\bar{\sigma}_{crit}$	0 MPa
n_1	0.4
n_2	0.4
n_3	0.4
n_4	0.4

Figure 59: Phase diagram for SMA used in validation model

A2. Design of Experiments 0.030 in Diameter NiTiCo SMA Wire

The following data gives the averaged properties for the SMA wire used in the design of experiments. To note, the following data averaged the properties for 7 alloys with slightly varying compositions of cobalt. The model parameters can be found in Table 6 while the raw phase diagram for the averaged data is shown in Figure 59. Furthermore, a plot of transformation strain against applied stress is shown in Figure 61 to illustrate how the transformation strain parameter $H_{cur}(\sigma)$ was calibrated.

Table 6: 0.030 in NiTiCo SMA wire model parameters used in DOE

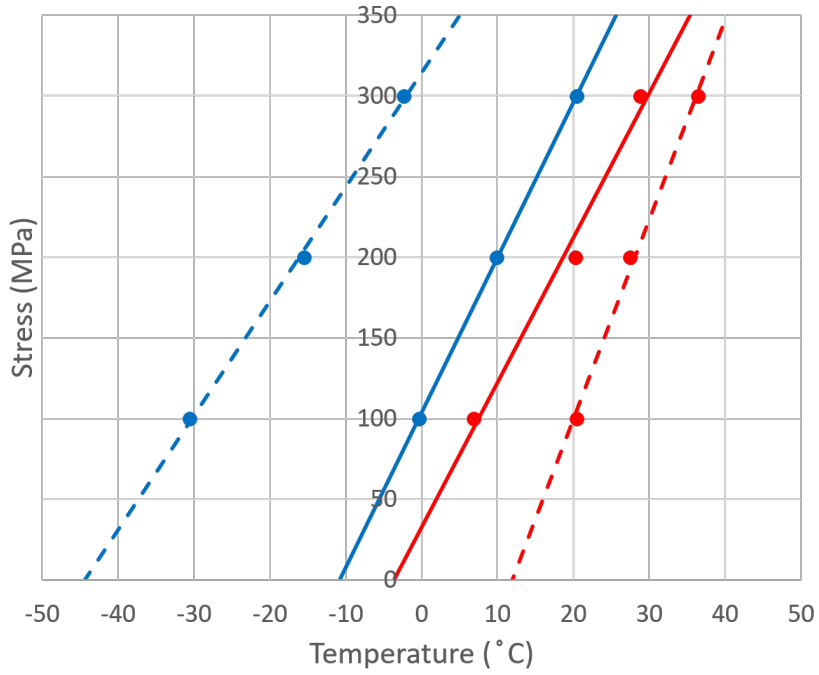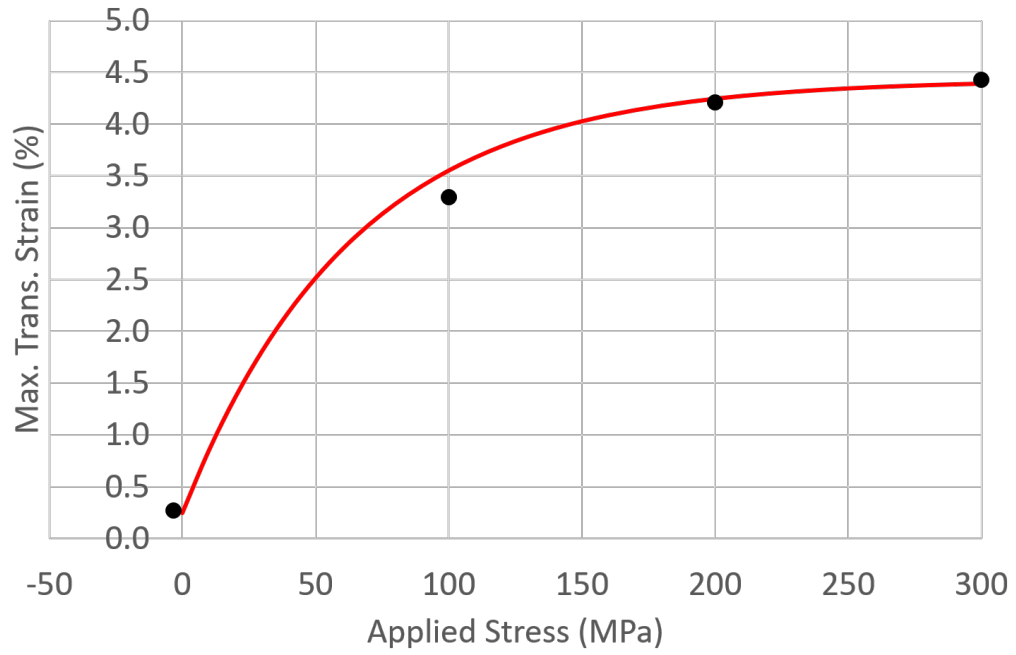| Model Parameter	Calibrated value
E^M	45.5 GPa
E^A	62.2 GPa
ν^M	0.33
ν^A	0.33
α^M	$0 \cdot 10^{-6}$ m/(m·°C)
α^A	$0 \cdot 10^{-6}$ m/(m·°C)
M_f	-44.4 °C
M_s	-10.8 °C
A_s	-3.7 °C
A_f	12.0 °C
C^M	8.15 MPa/°C
C^A	10.4 MPa/°C
H_{min}	0%
H_{max}	4.43%
k	1.56e-8 Pa^{-1}
$\bar{\sigma}_{crit}$	0 MPa
n_1	0.5
n_2	0.5
n_3	0.5
n_4	0.5

Figure 60: Phase diagram for SMA used in DOE model

Figure 61: DOE $H_{cur}(\sigma)$ calibration

8. APPENDIX B: MISCELLANEOUS DESIGN CONSIDERATIONS

This appendix contains the findings for some design considerations of the morphing radiator model. In particular two studies are presented here: a calculation of the effective thermal conductivity for the composite panel as well as a composite thickness tolerance stress sensitivty analysis.

B1. Composite Effective Thermal Conductivity

The thermal conductivity of the composite panel is a crucial metric when modeling since the temperature in the SMA drives the actuation of the radiator and the temperature of the panel drives the temperature in the SMA. Additionally, the temperature in the panel determines how much heat rejection is achieved. Thus, to accurately model this thermal conductivity in subsequent reduced order analyses, a calculation of the effective thermal conductivity for the chosen layup is presented here. Two methods were used and show good agreement in results. In both methods, the composite panel is modeled as flat for simplicity and a balanced layup of [90/45/0/-45/90] is used with a thermal conductivity definition given in the K_{11} (366 W/mK), K_{22} (0.25 W/mK) and K_{33} (0.25 W/mK) directions of the ply (these properties follow from the manufacturer Toray Composites) [8]. First, a constant temperature boundary condition was placed at the start and end of the composite panel through the thickness and the reaction heat flux was summed to obtain the total heat flux, Q. Then using the following equation, the effective thermal conductivity, Keff, was calculated to be 225.4 W/mK:

$$\frac{Q}{A_{23}} = \frac{K_{eff}\Delta T}{\Delta x} \tag{8.76}$$

$$A_{23} = L(5t) \tag{8.77}$$

$$\Delta T = (T_{start} - T_{end,avg}) \tag{8.78}$$

$$\Delta x = \frac{C}{2} = \frac{d}{2} \tag{8.79}$$

where Δx is the distance from the base of the panel to the tip of the radiator, otherwise calculated to be half of the circumference of the cylindrical panel. A_{23} is the cross-sectional area of the composite panel, defined as the lengthwise distance times the total ply thickness. Lastly, ΔT is the temperature difference between the two ends of the panel. Next, to further validate this result a second model was conducted which involves an applied concentrated heat flux at each node throughout the thickness of the composite panel. Essentially this acts as a discretely modeled heat flux on the cross-sectional area of the composite panel, which can then be used in the same equation above, where the temperature change from start to end is now measured. This resulted in an effective thermal conductivity of 221.8 W/mK. A temperature contour of the panel along with a schematic for this method can be seen below in Figure 62.
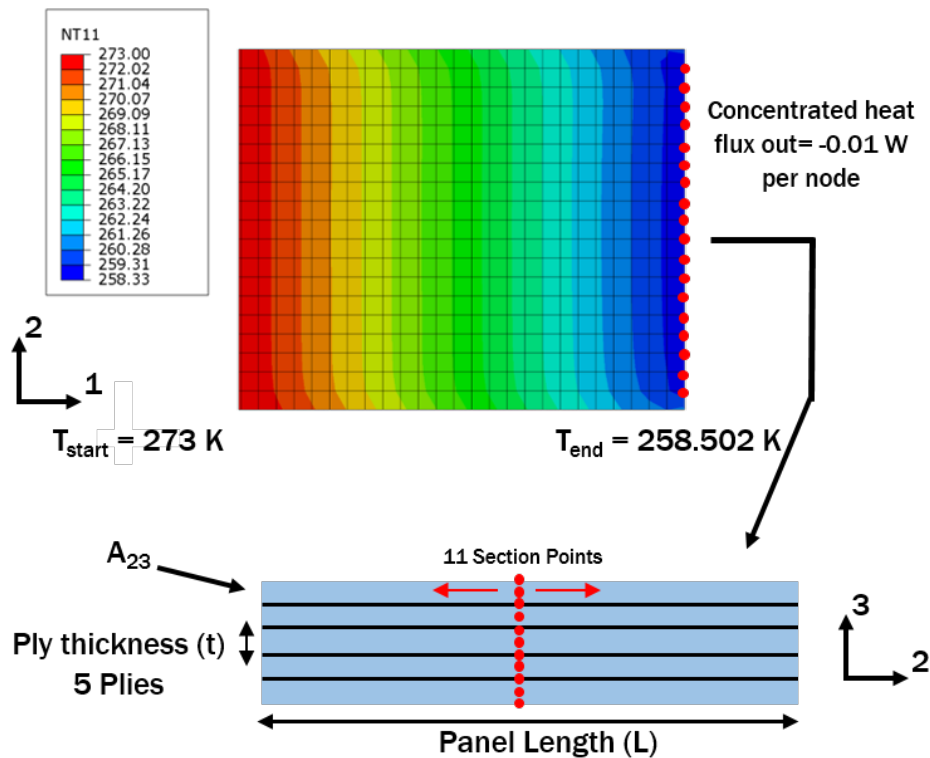

Figure 62: Temperature contour of composite panel with applied heat flux as shown

B2. Composite Thickness Tolerance Sensitivity Analysis

Upon manufacturing of the chosen composite layup, a rough estimate of the composite thickness tolerance was obtained. With previous stress results in this work demonstrating the composite performance for a nominal thickness, the data presented here will delve into the worst case tolerance. As thickness is highly impactful on the stress state of the composite in this bending problem, this thickness tolerance presents a real concern. The nominal composite thickness tolerance is 0.035" while the upper limit tolerance is 0.0385" thick. This tolerance was approximately obtained from differences between two manufactured composite panels. Figure 63 plots the failure stress factor against open angle for the chosen [90/45/0/-45/90] composite layup with the same wire pull loading scenario as the previous geometric trade study. The results show a failure stress factor of 1.21 at 180°, although this happens in the 90° ply in tension first which has a very low strength and is not a catastrophic failure. The more catastrophic failure in the 0° ply compressive direction amounts to 1.06 at 180 just exceeding the margin. For comparison, failure stress factors for the nominal composite thickness were 0.8404 for the 90° ply and 0.785 for the 0° ply at an open angle of 180°. This study demonstrates the high sensitivity of panel stress with composite thickness and acts as a method of honing the tolerance of the composite to a feasible range that maintains acceptable failure margins.
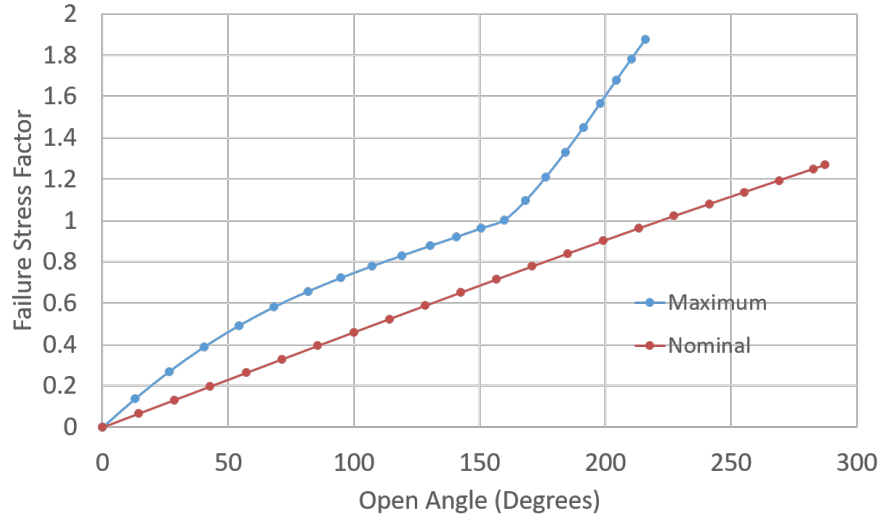
Figure 63: Failure stress factor vs. open angle plot for maximum and
nominal composite thickness tolerance

B3. Twinned Layup Performance in Composite Trade Study

Results below show the twinned layup performance compared to other layups for varying
open angles of the circular morphing radiator. Figure 64 shows the twinned layup to have higher
stress factors than the similar [90/45/0/-45/90] layup, although this was mainly due to highly
localized stress concentrations where the 45° ply layers meet which proved no problem during
testing. As a reminder these are the following layups that were compared where the parentheses
notate plies within the same ply layer:

- Layup 1: [90/45/0/45/90]
- Layup 2: [90/45/0/-45/90]
- Layup 3: [90/45/0/0/-45/90]
- Layup 4: [90/45/-45/-45/45/90]
- Layup 5: [90/45/-45/0/0/45/-45/90]
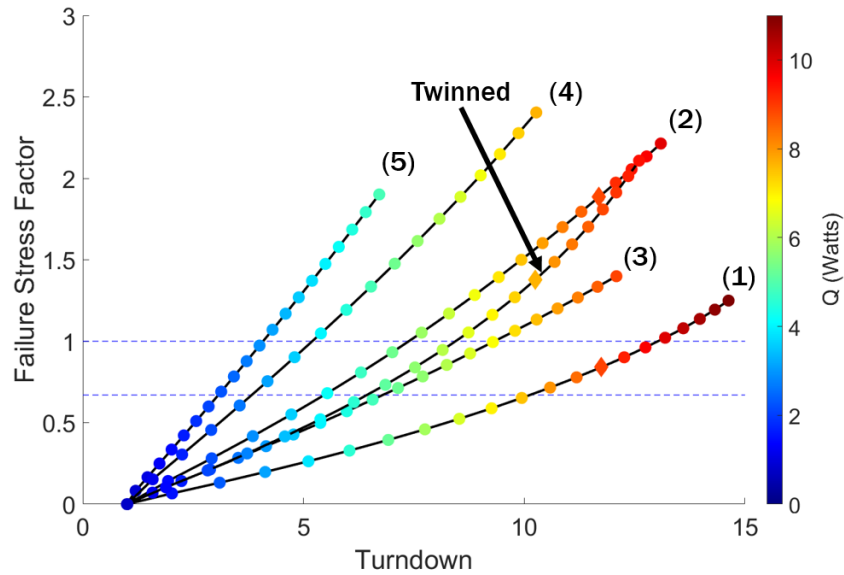- Twinned: [90/(45/-45)/0/(45/-45)/90]

Figure 64: Failure stress factor vs. open angle plot with twinned layup
added (diamond represents 180° open angle)

This localized stress concentration is illustrated below in Figure 65 at the point of failure. The entire middle region of the composite panel where the 45° ply layers meet has a stress concentration, peaking at the root of the panel where it is fixed to a mounting component. Also, this stress concentration manifests in the critical load bearing direction as an increased σ_{11}, and thus cannot be neglected. Although repeated experimental cycling did not show failure of any panels with this layup, non-catastrophic local damage could be taking place where the ply layers meet due to this discontinuity affecting overall compliance of the composite laminate.
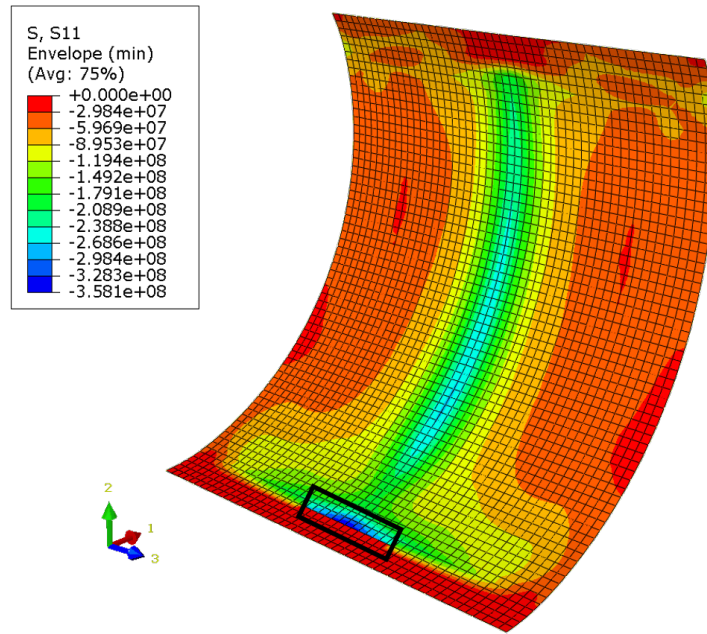
Figure 65: Visualization of stress concentration in twinned layup at failure stress